creative commons

COMMONS DEED

저작자표시-비영리-변경금지 2.0 대한민국

이용자는 아래의 조건을 따르는 경우에 한하여 자유롭게

- 이 저작물을 복제, 배포, 전송, 전시, 공연 및 방송할 수 있습니다.

다음과 같은 조건을 따라야 합니다:

저작자표시. 귀하는 원저작자를 표시하여야 합니다.

비영리. 귀하는 이 저작물을 영리 목적으로 이용할 수 없습니다.

변경금지. 귀하는 이 저작물을 개작, 변형 또는 가공할 수 없습니다.

- 귀하는, 이 저작물의 재이용이나 배포의 경우, 이 저작물에 적용된 이용허락조건을 명확하게 나타내어야 합니다.
- 저작권자로부터 별도의 허가를 받으면 이러한 조건들은 적용되지 않습니다.

저작권법에 따른 이용자의 권리는 위의 내용에 의하여 영향을 받지 않습니다.

이것은 이용허락규약(Legal Code)을 이해하기 쉽게 요약한 것입니다.

Disclaimer

dCollection

공학박사학위논문

A study on the changes in rheological behavior and dispersion state of electrode slurry during processing

가공 중 전극 슬러리의 유변학적 거동 및 분산 상태 변화에 대한 연구

2023년 8월

서울대학교 대학원
화학생물공학부
박정훈

A study on the changes in rheological behavior and dispersion state of electrode slurry during processing

가공 중 전극 슬러리의 유변학적 거동 및 분산 상태 변화에 대한 연구

지도교수 안 경 현

이 논문을 공학박사 학위논문으로 제출함
2023년 8월

서울대학교 대학원
화학생물공학부
박정훈

박정훈의 공학박사 학위논문을 인준함
2023년 8월

위 원 장 _____(인)

부위원장 _____(인)

위 원 _____(인)

위 원 _____(인)

위 원 _____(인)

Abstract

Dispersibility of the Li-ion battery electrode slurry is emerging as an important issue in both academia and industry as it directly affects the battery performance as well as the productivity of the electrode process. To effectively control the slurry dispersion in the electrode process, a comprehensive understanding of both material and process characteristics is required. However, an in-depth understanding of the processing effects on the interactions between individual components of the slurry, and the consequent changes in slurry dispersion, is still lacking.

In this thesis, changes in rheological behavior and dispersion state of the Li-ion battery electrode slurry in the electrode processes were systematically studied, with particular focus on slurry preparation and storage stages, from the viewpoint of process conditions as well as interaction between individual components. In the first chapter, focusing on the slurry preparation stage, various roles of carboxymethyl cellulose (CMC) binder in the graphite/carbon black (CB) anode slurries and their effect on the slurry preparation process were studied. CMC played various roles as a dispersant, thickener, and gelling agent depending on its content. In particular, it was confirmed that the mixing sequence of CMC and the two particles had a significant effect on the slurry dispersion at a CMC content lower than the optimum graft density due to the similar adsorption and dispersion mechanism of CMC for the two particles. In the next chapter, we focused on the slurry storage stage, and studied the changes in the dispersion state of lithium nickel

manganese cobalt oxide (NMC)/acetylene black (AB) cathode slurry during storage, as well as their underlying mechanism. It was found that hydrodynamic stress induced by the flow dominates the changes in slurry dispersion. Therefore, cathode slurry showed different dispersion states before and after storage conditions of critical hydrodynamic stress. In the last chapter, rheological behavior and microstructure formation mechanism of anode slurries containing a next-generation silicon (Si) active materials were studied. It turns out that CMC selectively adsorbs onto CB particles among the two particles in the Si/CB/CMC slurry. Therefore, it was confirmed that CMC acts as a dispersant for the CB particles at low content, while it acts as a flocculant for the particles at high content in the slurries.

This thesis was conducted with the purpose of providing an in-depth understanding of the changes in slurry dispersion in the liquid phase electrode process, specifically focusing on the slurry preparation and storage stages, based on the understanding of the interaction between individual components of the electrode slurry. The findings are expected to provide guidelines for slurry processing, contribute to the electrode process optimization and productivity improvement.

Keyword: Li-ion battery, electrode process, slurry dispersion, binder, rheology, microstructure

Student Number: 2018-26542

Table of Contents

List of Figures

Chapter 1. Introduction

1.1. General introduction

As the need for eco-friendly and renewable energy emerges, the industrial demands of lithium-ion batteries (LIBs) for energy storage system (ESS) [1, 2] and electric vehicles (EVs) [3-5] are increasing explosively. LIBs have various advantages such as having high energy density, long cycle life, high operating voltage, no memory effect, and being lightweight compared to conventional battery technologies [6-9]. However, in order to keep up with industrial demand, LIBs technology needs to be further advanced. Advancements include material development, but production process optimization is essential to ensure productivity, especially for electrodes.

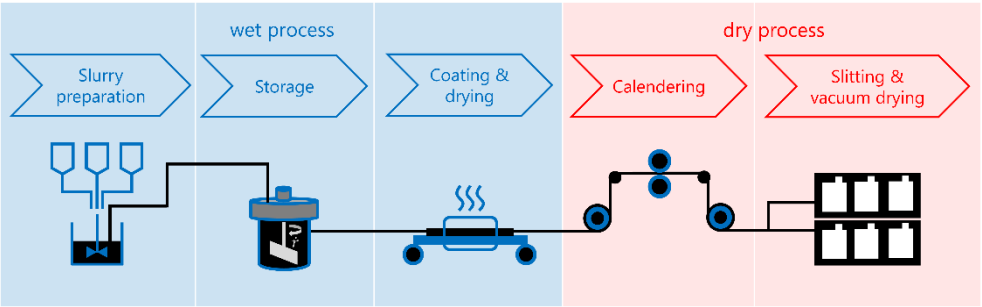

Figure 1.1. Schematic of the electrode preparation process.

The electrodes for LIBs are manufactured through wet processes of slurry preparation, storage, and coating and drying, and dry processes of calendaring, and slitting and vacuum drying, as shown

in Figure 1.1[10-14]. In the first process, the electrode slurry is prepared by mixing and dispersing raw materials (active material, conductive agent, and polymeric binder) in a casting solvent. The dispersion state of the slurry is very important as it directly affects various electrode properties such as coating quality, electrode microstructure, adhesion strength, and electrochemical performance in the following electrode process[15-18]. The slurry dispersion strongly depends on the microstructure formed through the interaction between its individual components during mixing and dispersing each component. Therefore, many studies have been conducted to understand the slurry dispersion in terms of interaction between each component of the slurry[19-27].

In general, cathode and anode slurries show different dispersion characteristics. The main difference comes from the adsorption behavior of the binders. Conventional cathode slurry composed of lithium metal oxide (active material), carbon black (CB, conductive agent), poly(vinylidene fluoride) (PVDF, polymeric binder), and N-methyl-2-pyrrolidone (NMP, solvent) shows gel-like behavior due to the network structure formed by the attractive interaction between the particles. Sung et al. showed that PVDF adsorbs neither onto NMC ($Li(Ni_{1/3}Mn1_{/3}Co_{1/3})O_2$) nor CB surface and does not significantly affect the interaction between the particles. Therefore, as shown in Figure 1.2a and b, PVDF mainly increases viscous part (viscosity, G") of the slurry without significantly affecting the solid-like character (G'), which originates from the network structure of the particles[20]. Therefore, the direct interaction between the particles has a significant effect on the dispersion of cathode slurry, leading to a gel-like behavior. Morelly et al. showed that conductive

nanoparticles (CB) mainly determine the gelation behavior of the cathode slurry, independently of the presence of non-Brownian active material (NMC) particles, as shown in Figure 1.2c and d. They demonstrated that NMC particles do not participate in the percolating network structure of the conductive nanoparticles, regardless of the volume-fraction of the NMC particles[21]. However, a few cases were observed in which the cathode slurry exhibits a liquid-like behavior through the addition of a dispersant for CB particles[20] or through a specific preparation process that disrupts the CB network[22].

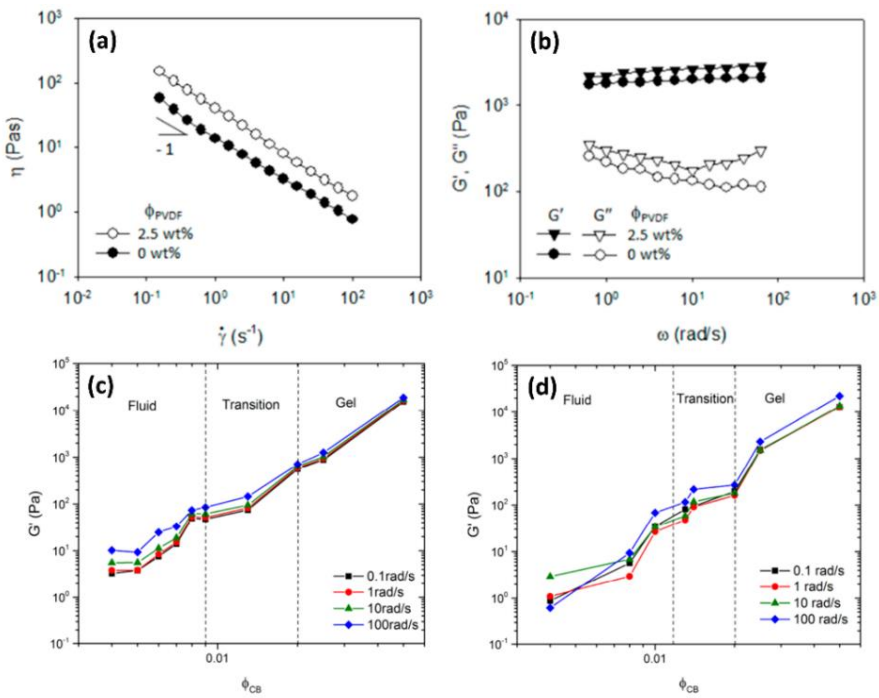

Figure 1.2. (a) Steady shear viscosity and (b) frequency dependent storage (G') and loss (G") modulus of NCM/CB/PVDF/NMP cathode slurries (NCM 25 vol%, CB 1.3 vol%). G' vs volume fraction of carbon black at each frequency for (c) $\phi_{NMC}=0$ and (d) $\phi_{NMC}=0.26$.

On the other hand, a typical anode slurry composed of graphite

(active material), carbon black (conductive agent), anode binder, and water (solvent) exhibits liquid-like behavior. This is attributed to the adsorption characteristics of the anode binder. Anode binders such as sodium carboxymethyl cellulose (CMC), styrene butadiene rubber (SBR), and poly(acrylic acid) (PAA) adsorb onto the particles that tend to agglomerate and stabilize the particle network structure through repulsive interaction[23-26]. In Figure 1.3a and b, as the content of CMC (Figure 1.3a) and SBR (Figure 1.3b) increases and adsorption amount increases, G' of the slurries decreases significantly, indicating stabilization of the network structure of the graphite particles[23]. Likewise, in Figure 1.3c, as pH decreases and adsorption amount of PAA increases, yielding behavior disappears and the slurry shows a Newtonian behavior (at pH=2.7), suggesting disruption of the network structure of the particles[24]. The polymer-particle interactions play a critical role in the anode slurry dispersion, in contrast to the cathode slurry dispersion where direct particle-particle interaction is significant.

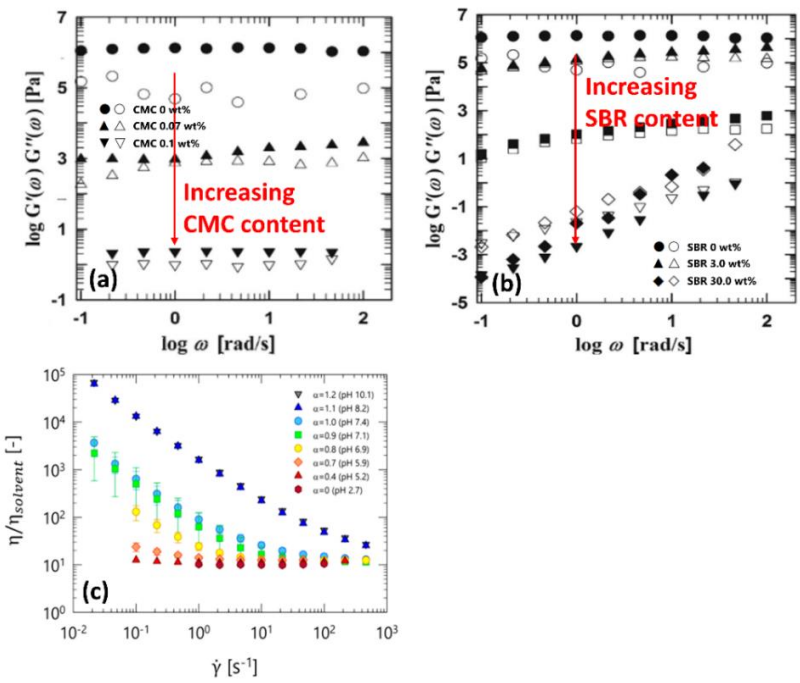

Figure 1.3. G' (closed symbol) and G" (open symbol) of 50 wt% graphite slurry as a function of frequency with increasing (a) CMC content and (b) SBR content. (c) relative viscosity of the anode slurry (graphite 40 wt%, CB 2.0 wt%, PAA 1.5 wt%) as a function of shear rate with varying pH.

Studies have been conducted to understand the general dispersion behavior of the electrode slurries. However, they did not sufficiently consider the processing effect on the slurry dispersion, which is crucial for optimizing the electrode process. Complex fluids, such as electrode slurries, can undergo structural deformation by the flow, resulting in a significant change in dispersion state even when the composition is the same. Unexpected changes in dispersion state cause various industrial problems in the electrode process, hindering process optimization and productivity. Therefore, a fundamental understanding of the processing effects on slurry dispersion in the unit electrode process is essential. In this thesis, changes in the slurry dispersion during wet electrode processing, particularly focusing on the slurry preparation and storage stages, were extensively studied from the viewpoint of the interaction between each component to broaden our knowledge of the processing effect on the slurry dispersion.

1.2. Objectives and outline of the thesis

The objective of this thesis is to provide fundamental insight into the processing effects on slurry dispersion, particularly in the slurry preparation and storage stages, and contribute to electrode process optimization and productivity improvement. The slurry dispersion is mainly evaluated through rheological analysis and microstructure observation. The subject of this thesis is classified into the following three categories: (1) role of carboxymethyl cellulose (CMC) binder and its effect on the preparation process of graphite/CB anode slurries (2) significant agglomeration of conductive materials and dispersion state change of Ni-rich NMC cathode slurries during storage (3) rheological behavior and microstructure formation of Si/CB anode slurries. An outline and brief description of this thesis are as follows.

In chapter 2, we focus on the slurry preparation stage, and systematically investigate role of CMC and how it affects the slurry preparation process, in terms of the effect of CMC on the inter-particle interactions. At first, we find that CMC plays various roles as a dispersant, thickener, and gelling agent in the slurry depending on its content. Then, based on the understanding of the role of CMC, we report that the mixing sequence of CMC and the two particles (carbon black, graphite) has a significant effect on the slurry dispersion below the CMC content of the optimum graft density, which is attributed to the adsorption selectivity of CMC for the two particles. The mechanism of the structural changes is understood by considering the role of CMC in each preparation step based on the adsorption selectivity of CMC.

In chapter 3, we focus on the storage stage of the slurry after slurry preparation, and systematically investigate how storage conditions affect the dispersion of the cathode slurry. We find that hydrodynamic stress induced by the flow governs the change in slurry dispersion during storage, by controlling both process condition (agitation speed) and material condition (matrix viscosity). The cathode slurry exhibits different dispersion states before and after storage conditions of critical hydrodynamic stress. In particular, we observe that the conductive materials form large spherical agglomerate even larger than the active material under the storage conditions lower than the critical hydrodynamic stress, which can cause industrial problems in subsequent electrode process. The mechanism is understood by considering the relative affinity between particles and the flow characteristics during storage.

In chapter 4, we investigate the rheological behavior and microstructure formation of anode slurries containing a next-generation silicon active material. We find that CMC adsorbs onto both CB and Si particles, but it acts as a dispersant for CB particles while it acts as a flocculant for Si particles. Meanwhile, we confirm that CMC selectively adsorbs onto CB particles among the two particles. Therefore, at a CMC content lower than the optimum graft density for the CB particles, CMC acts as a dispersant in the Si/CB slurries. However, at a higher content, CMC acts as a flocculant for the particles. The origin of selective adsorption is understood in terms of driving forces for adsorption and surface energy analysis.

Finally, in chapter 5, a concluding remark is present. We anticipate our findings will provide guidelines for the slurry processing and contribute to optimizing the electrode process.

Chapter 2. Role of carboxymethyl cellulose binder and its effect on the preparation process of anode slurries

2.1. Introduction

The slurry dispersion is emerging as an important issue in both academia and industry as it directly affects various electrode properties such as coating quality, electrode microstructure, adhesion(cohesion) strength, and electrochemical performance in the subsequent electrode process[15-18]. Therefore, many studies have been conducted to understand the microstructure and rheological properties of the slurries from the perspective of the interaction between each component, as the slurry dispersion strongly depends on the structure formed by the interaction of each component during the preparation step[19-34].

Previous studies can be classified as two groups; one on the materials and the other on the preparation process[35, 36]. From the material point of view, the research focused on understanding the role of the binder, a key component in controlling the slurry dispersion[24, 25, 37-41]. The studies mainly focused on the adsorption behavior of the binder, which facilitates control of the rheological properties and microstructure of the slurry. Gordon et al. investigated the effect of molecular weight (MW) and degree of substitution (DS) of carboxymethyl cellulose (CMC) binder on the

flow behavior of the anode slurry and electrode properties. With high MW and low DS, the cohesive strength and the electric conductivity of the electrode increased. They explained CMC with high MW and low DS adsorbed more on graphite particles, improving the slurry dispersion as well as the alignment of graphite particles in the electrode[25]. Sung et al. studied the dispersion heterogeneity of the anode slurry according to the neutralization degree α of poly(acrylic acid) (PAA) binder. The anode slurry showed a liquid-like behavior with low viscosity at low α (acidic condition), while showing a gel-like behavior at high α (basic condition). They claimed that the adsorption amount of PAA on graphite particles changed dramatically with α, resulting in a significant difference in carbon black (CB) distribution in the slurries[24].

On the other hand, from the perspective of preparation process, most studies have been conducted on the effect of mixing protocols on slurry dispersibility[22, 29, 42-47]. Li et al. found that graphite particles interacted favorably with CMC among CMC and styrene-butadiene rubber (SBR) binders while lithium iron phosphate (LFP) particles interacted favorably with SBR. Consequently, the slurry dispersibility was found to be better when sequentially adding CMC and SBR to the particles compared to when adding both binders at the same time[42]. In addition, the studies on improving the slurry dispersibility by dry-mixing of active material and conductive agent[44-46] or by adding a solvent in a multi-step process[22, 29] have also been conducted. However, previous studies had some limitations. From the material point of view, even though binders can play a variety of roles in particulate suspensions, such as electrode slurries, research has been limited to their role in

adsorption behavior. Furthermore, adsorption behavior of the binder was understood with a single-component model slurry which does not contain both active material and conductive particles[23-25, 37, 38]. Also, the change in adsorption behavior was limited to adjusting the pH[24] or changing the molecular structure (MW, DS) of the binder[25, 37, 38]. From the perspective of preparation process, the binder content was fixed and the effect of binder on the interaction between individual particles was not sufficiently considered[22, 44-47]. As the binder can have various effects on the interactions between each particle depending on its content in particulate suspensions[48-51], like electrode slurries, it is necessary to understand the preparation process along with the various roles of a binder, which depend on its content.

In this study, we systemically investigate the various roles of CMC binder in the anode slurry containing both active and conductive materials, and their effect on the slurry preparation process in terms of the effect of CMC on the inter-particle interactions at each preparation stage. The results consist of two parts. In chapter 2.3.1, we explore the various roles of CMC in the anode slurry through the interaction of CMC with CB and graphite particles. We observe that CMC causes rapid rheological and microstructural changes in both CB/graphite suspensions and anode slurries with increasing its content. It turns out that the role of CMC changes according to its content as adsorbed CMC and free CMC have different effects on the inter-particle interaction. Then, in chapter 2.3.2, based on the understanding of the role of CMC, we systematically design the slurry preparation process by changing the mixing sequence of CMC and the two particles, and investigate its

effect on the slurry dispersion with respect to the CMC content. We clarify that the mixing sequence of CMC significantly affects the slurry dispersion below a certain CMC content. The microstructure change mechanism at each process is understood by considering the role of CMC in each preparation stage and its adsorption selectivity onto the particles.

2.2. Experimental section

2.2.1. Materials

Spherical graphite (SG-BH8, Ito Graphite Co., Ltd, Japan) was used as an anode active material. According to the supplier, the average particle size, specific surface area, and density were 8.1 μm, 12.1 m^2/g, and 2.23 g/cm^3, respectively. Carbon black (Timcal Super C65, MTI Korea, Korea) was used as a conductive material. The primary particle size was less than 50 nm, and the specific surface area and the density were 62 m^2/g and 2.25 g/cm^3, respectively, according to the supplier. Sodium carboxymethyl cellulose (CMC, Sigma-Aldrich, USA) was used as a polymeric binder. The molecular weight (M_w) and the degree of substitution (DS) were 250,000 g/mol and 0.7, respectively. Deionized water was used as a casting solvent.

2.2.2. Sample preparation

Each CMC solution (0.1 ~ 5.0 wt%) was prepared by adding a specific amount of CMC to deionized water and dissolving for 6 hours at 1,000 rpm using an anchor-type mechanical stirrer. The CB suspension was prepared by dispersing CB particles into the prepared CMC solution at 6,000 rpm for 10 minutes using a rotor-state homogenizer (Ultra-turrax T18, IKA, Germany) equipped with an S18N-19G dispersing element. The graphite suspension was prepared by adding graphite particles to the prepared CMC solution and mixing for 10 minutes at 1,000 rpm using an anchor-type mechanical stirrer. The particle contents of the graphite and CB suspensions were selected such that the two suspensions show

similar rheological properties in order to usefully explain the interaction between the particles and CMC. The anode slurry was manufactured by adding graphite and CB particles to the prepared CMC solution and dispersing at 6,000 rpm for 10 minutes using a homogenizer, followed by mixing at 1,000 rpm for 10 minutes using a mechanical stirrer. The particle composition of the anode slurry was selected based on the content ratio (graphite:CB = 20:1) commonly used for anodes.

2.2.3. Rheological characterization

The rheological properties of each sample were measured using a stress-controlled type rheometer (AR-G2, TA instruments, USA) equipped with either a 40 mm parallel plate (liquid-like sample) or 40 mm cross-hatched (gel-like sample) fixture. The loading gap of the sample was set to 800 - 1500 μm depending on the initial loading conditions of the sample. The viscosity was measured through a descending-mode (1000 s^{-1} to 0.01 s^{-1}) shear rate sweep test. The viscoelastic properties of the sample were obtained through a descending-mode (100 rad/s to 0.25 rad/s) frequency sweep test in the linear viscoelastic (LVE) region, as the data reliability was poor at low frequencies when measuring frequency sweep test in an ascending-mode.

2.2.4. Adsorption isotherm

Adsorption isotherms (CB-CMC and graphite-CMC) were obtained by the solution depletion method, which is commonly used to measure the adsorption amount. First, CB and graphite suspensions of various CMC content were prepared around the CMC content expected as the adsorption saturation point. Then, each

suspension was centrifuged at 10,000 rpm for at least 24 hours using a high-speed centrifuge (Supra R17, Hanil Scientific Inc, Korea). After confirming that the particles were completely precipitated (verified by transparent supernatant), the supernatant CMC solution was transferred to a petri dish and dried overnight at 40℃ in a convection oven. When all the solvent was evaporated, the mass of the solid was measured to calculate the CMC content of each supernatant solution. Finally, the amount of CMC adsorption was calculated from the difference in CMC content of the original suspension and of the centrifuged supernatant.

2.2.5. Microstructure observation

The microstructure of the anode slurry was observed using a polarizing microscope (BX51, Olympus, Japan). To obtain an optical micrograph, the slurry was first diluted 15 times with deionized water and then mixed for 10 seconds using a vortex mixer (VM-10, ALLforLAB, Korea). Too much dilution leads to an insufficient number of particles while too little dilution leads to dark and obscure images. Both make it difficult to observe the structure, thus the 15 times of dilution was chosen as the most appropriate for observation. Then, 0.1 mL of the diluted slurry was carefully loaded onto a slide glass using a dropper and covered with a cover glass. Finally, the optical micrographs of the slurry were obtained with 10 times and 50 times magnification. The optical micrographs of CB suspension and graphite suspension were obtained through the same procedure except that the dilution factor was 10 and 15, respectively.

2.3. Results and discussion

2.3.1. Role of CMC binder in the anode slurry

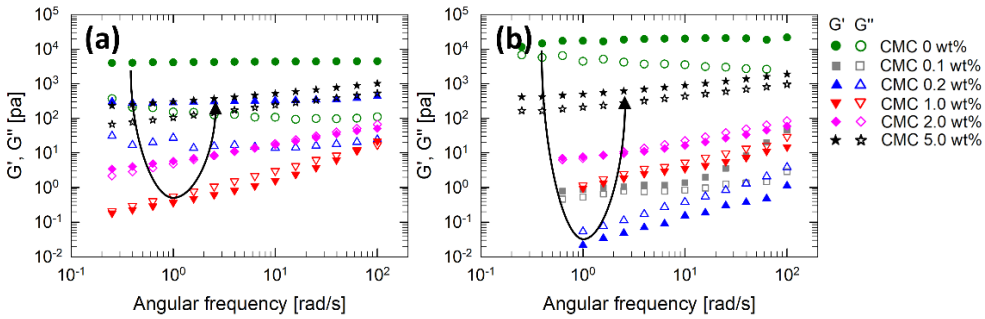

Figure 2.1. Storage (closed symbol) and loss (open symbol) modulus of (a) 5 wt% CB suspensions and (b) 45 wt% graphite suspensions as a function of frequency with varying CMC content. The arrow indicates an upturn of G' and G".

Figure 2.1 shows the frequency sweep results of CB suspension (Figure 2.1a) and graphite suspension (Figure 2.1b) with varying CMC content. Both suspensions show a sharp change in viscoelastic properties with increasing CMC content. The CB suspension without CMC shows G' of the order of thousand with frequency independence over a wide range of frequencies, suggesting a gel-like behavior. In a hydrophilic solvent, CB (or graphite) particles with non-polar surface agglomerate by hydrophobic interaction between the particles[52, 53] to form a volume-spanning network, which contributes to strong elasticity. As the CMC content increases to 0.2 wt%, G' decreases by an order. However, the CB suspension still shows a gel-like behavior, suggesting that the network structure is weakened but still present. As the CMC content increases to 1.0 wt%, G' decreases sharply, and G' and G"

are reversed over the investigated frequency range, indicating that the CB suspension shows a liquid-like behavior. It suggests that the CB network structure is disrupted. As the CMC content further increases, both G' and G" increase. Finally, at CMC 5.0 wt%, G' and G" are reversed again, and the CB suspension shows a weak-gel behavior in which G' is larger than G" and has a weak frequency dependence ($G' \sim \omega^{0.24}, G'' \sim \omega^{0.34}$), suggesting the formation of another network structure.

Graphite suspension shows a similar behavior as the CB suspension. In the absence of CMC, it shows a gel-like behavior with G' of the order of ten thousand. As the CMC content increases to 0.1 wt%, although the G' decreases significantly, a low-frequency plateau is observed, suggesting that the network structure still exists[54, 55]. As the CMC content increases to 0.2 wt%, G' and G" are reversed and it shows a liquid-like behavior, suggesting the disruption of the network structure. As the CMC content further increases, both G' and G" increase. Finally, at CMC 5.0 wt%, G' and G" are reversed again and it shows a weak-gel behavior ($G' \sim \omega^{0.25}, G'' \sim \omega^{0.29}$), indicating that another network structure is formed.

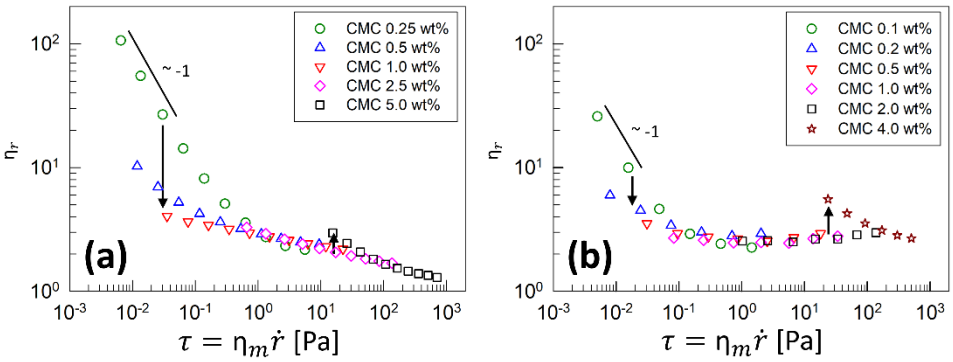

Figure 2.2. Relative viscosity curves of (a) 3 wt% CB suspensions, and (b) 45 wt% graphite suspensions with varying CMC content.

To better understand the effect of CMC on the interaction between CB and graphite particles, the viscosity curves of CB (Figure 2.2a) and graphite suspensions (Figure 2.2b) are investigated with varying CMC content. Relative viscosity ($\eta_r = \frac{\eta_{susp}}{\eta_{matrix}}$) is expressed with respect to the hydrodynamic stress ($\tau = \eta_{matrix}\dot{\gamma}$). This characterization is a useful rheological technique to rule out the contribution of the binder itself and to investigate the effect of the binder on the inter−particle interactions[40]. The CB suspension shows a yielding behavior (negative slope of −1) at CMC 0.25 wt%, suggesting the presence of a network structure. As the CMC content increases up to 1.0 wt%, the slope of the viscosity curve at low hydrodynamic stress ($\tau < 1\,Pa$) decreases significantly, suggesting a weakening of the structure. As the CMC content increases from 1.0 wt% to 2.5 wt%, the slope of the viscosity curves and the order of the relative viscosity are almost identical in the investigated hydrodynamic stress range to form a single master curve. However, at CMC 5.0 wt%, the slope at $\tau < 100\,Pa$ increases again, indicating the formation of another structure.

The graphite suspension shows a similar behavior as the CB suspension. The graphite suspension shows a yielding behavior at CMC 0.1 wt%, and the slope at low hydrodynamic stress $(\tau < 0.1\ Pa)$ decreases significantly as the CMC content increases to 0.2 wt%. As the CMC content increases from 0.2 wt% to 2.0 wt%, the viscosity curve shows a universal behavior to form a master curve. However, at CMC 4.0 wt%, the slope at $\tau < 100\ Pa$ increases again. In both CB and graphite suspensions, G' and G" are reversed twice (Figure 2.1) and the shape of the viscosity curve changes twice (Figure 2.2) as the CMC content increases.

CMC is known as a surfactant for carbon-based materials (CB, graphite) in an aqueous medium due to its molecular structure consisting of hydrophobic carbon chains and hydrophilic functional groups (carboxyl group). The hydrophobic part provides an opportunity for CMC to adsorb on the particles (CB, graphite) by hydrophobic interaction, whereas the charged hydrophilic part can stabilize the hydrophobic surface of the adsorbed particles by electro-steric interaction[56].

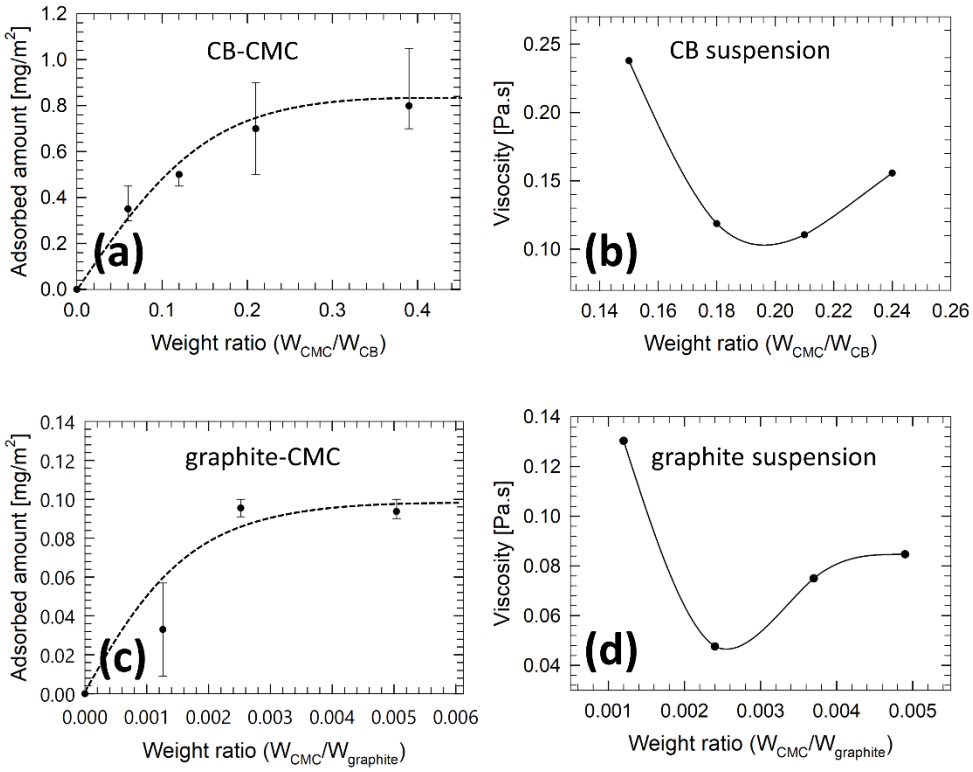

Figure 2.3. Adsorption isotherm of (a) CB−CMC and (c) graphite−CMC. Viscosity (shear rate = 1 s^{-1}) of (b) 3 wt% CB and (d) 45 wt% graphite suspensions as a function of weight ratio of CMC to particle ($W_{CMC}/W_{particle}$).

Figure 2.3a shows the adsorption isotherm of CMC to CB. The adsorption amount, which is the graft density, refers to the weight of the polymer adsorbed per unit surface area of the particle. The adsorption amount increases as the weight ratio of CMC to CB (W_{CMC}/W_{CB}) increases. Around W_{CMC}/W_{CB} = 0.2, CMC completely covers the CB surface and the adsorption is saturated. Figure 2.3b shows the change in viscosity of the CB suspension with increasing W_{CMC}/W_{CB}. As W_{CMC}/W_{CB} increases, the viscosity of the CB suspension decreases and then increases, reaching a minimum near the adsorption saturation point (W_{CMC}/W_{CB} = 0.2). It is well known

that the dispersion state is optimal at this optimum graft density (~$0.8\,mg/m^2$ for CB−CMC) where the viscosity is minimized[28, 55]. Figure 2.3c shows the adsorption isotherm of CMC to graphite. Adsorption is saturated around $W_{CMC}/W_{graphite}$ = 0.0024. Figure 2.3d shows the change in viscosity of the graphite suspension with increasing $W_{CMC}/W_{graphite}$. Like the CB suspension, the CMC content becomes optimal (graft density~$0.1\,mg/m^2$ for graphite−CMC) with a minimum viscosity near the adsorption saturation point ($W_{CMC}/W_{graphite}$ = 0.0024). The CMC contents of the optimum graft density in the CB and graphite suspensions shown in Figure 2.1 and Figure 2.2 are 1.0 wt% and 0.2 wt%, respectively. Therefore, the two particles are more dispersed and stabilized by the adsorbed CMC and the dispersion becomes optimal at CMC 1.0 wt% for CB suspension and CMC 0.2 wt% for graphite suspension. Accordingly, as the CMC content increases to 1.0 wt% for the CB suspension and to 0.2 wt% for the graphite suspension, the elasticity of both suspensions rapidly decreases to show a liquid−like behavior (Figure 2.1a and b) and the slope of the viscosity curves of both suspensions decreases and the yielding behavior disappears (Figure 2.2a and b). From the results in Figure 2.1, Figure 2.2, and Figure 2.3, it can be known that CMC acts as a dispersant in CB and graphite suspensions at a content lower than the optimum graft density where CMC is adsorbed and saturated.

In Figure 2.2a and b, as the CMC content increases above the optimum graft density (1.0 ~ 2.5 wt% for the CB suspension and 0.2 ~ 2.0 wt% for the graphite suspension), the viscosity curves of the CB and graphite suspensions show a universal behavior to form a master curve over a wide range of the hydrodynamic stress. This

is a typical rheological behavior when a non-adsorbing polymer increases the matrix viscosity without significantly affecting the interaction between the particles[20, 57, 58]. In this case, more CMC is present in the suspensions than is required for adsorption saturation. Therefore, the CMC adsorbed on the particles (as much as the adsorption saturation of each particle) acts as a dispersant and the extra CMC exists in the matrix (i.e. free CMC) mainly acting as a thickener to increase the viscosity without significantly affecting the interaction between the particles.

In Figure 2.2a and b, as the CMC content further increases to 4.0 (graphite suspension) or 5.0 wt% (CB suspension), the slope of the viscosity curve at $\tau < 100\,Pa$ increases again, suggesting the formation of another network structure. To understand this behavior, we investigate the rheological properties of the CMC solution (Figure 2.4).

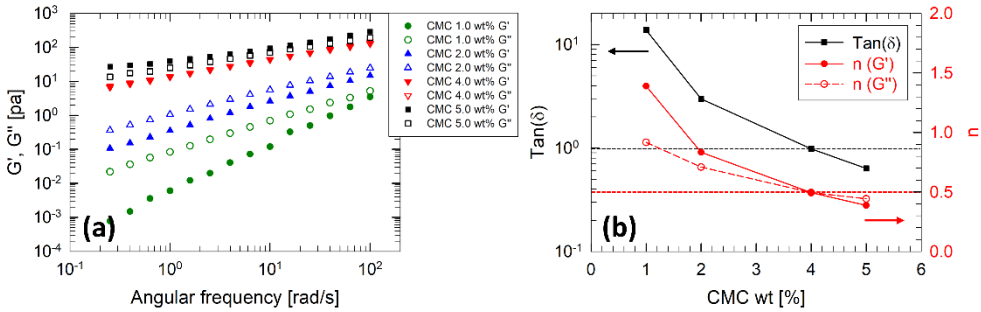

Figure 2.4. (a) frequency sweep results of the CMC solution with varying CMC content. (b) Tan(δ) = G"/G' at frequency = 1 rad/s (square symbol, left) and the powers (n) of G', G" with respect to frequency ($G' \sim \omega^n, G'' \sim \omega^n$) (circular symbol, right) of the CMC solution with varying CMC content. The black dashed line represents the line with tan(δ)=1 and the red dashed line represents the line with n=0.5.

Figure 2.4a shows frequency sweep results of the CMC solution with increasing CMC content. As CMC content increases, both G' and G" increases. Figure 2.4b shows tan(δ) = G"/G' (ω = 1 rad/s) and the powers (n) of G' and G" with respect to frequency ($G' \sim \omega^n, G'' \sim \omega^n$) of the CMC solution with increasing CMC content. At CMC 1.0 and 2.0 wt%, the CMC solution exhibits a viscoelastic liquid-like behavior (tan(δ)>1, $n(G') > n(G'')$). However, it shows a critical-gel behavior (tan(δ)~1, $n(G'') \sim n(G') \sim 0.5$ at CMC 4.0 wt% and weak-gel behavior (tan(δ)<1, $n(G') < n(G'')$ at CMC 5.0 wt%. When the CMC content is low, the electrostatic interaction between functional groups of the CMC dominates, so the CMC chain adopts an extended conformation. However, as the CMC content increases above the critical concentration, the interaction between the hydrophobic chains dominates as the chains come closer. In this case, CMC is entangled by local polymer-polymer hydrophobic

interactions[59, 60] forming a 3D-fibrillar network with a size of sever hundred nm[61]. Our results are similar to previous studies on a CMC solution of similar DS, where the hydrophobic interaction between the chains dominate above CMC 2.5 wt%, and the CMC solution exhibits a weak-gel behavior at CMC 5.0 wt%[60]. Therefore, the critical gel and weak-gel behavior of the CMC solution implies the formation of a 3D-fibrillar network of CMC. However, G' of the CB and graphite suspensions at CMC 5.0 wt% (Figure 2.1a and b) is about 10 times larger than that of CMC 5.0 wt% solution (not shown here). It is often found that the gelling solution interacts with particles to form a more rigid structure[62]. Therefore, when the CMC content is high enough to induce entanglement of free CMC (more than 4.0 wt% in this study), CB and graphite particles dispersed by adsorbed CMC (electro-steric stabilization) and the 3D-fibrillar networks formed by free CMC (hydrophobic interaction) interact together to form a more robust structure. Accordingly, at CMC 5.0 wt%, the CB and graphite suspensions show a weak-gel behavior at CMC 5.0 wt% (Figure 2.1a and b). Also, the slope of the viscosity curves of both suspensions increases at CMC 5.0 wt% for the CB suspension and at 4.0 wt% for the graphite suspension (Figure 2.2a and b).

The structural change of CB and graphite suspensions according to CMC content can be intuitively confirmed through optical micrographs (Figure 2.5). In the absence of CMC, CB (Figure 2.5a) and graphite particles (Figure 2.5b) aggregate to form a volume-spanning network. At CMC content below the optimum graft density, some of the CB (Figure 2.5c) and graphite (Figure 2.5d) particles are dispersed by the adsorbed CMC while others still form a network

structure. Specifically, in Figure 2.5c, CB agglomerates with a size of several tens of microns are observed. In addition, matrix becomes cloudy than without CMC (Figure 2.5a) as some of the CB is dispersed into aggregate (sub-micron in size) by the adsorbed CMC (as will be discussed in detail in chapter 2.3.2). At CMC content above the optimum graft density, most of the CB (Figure 2.5e) and graphite (Figure 2.5f) particles are well-dispersed by the adsorbed CMC.

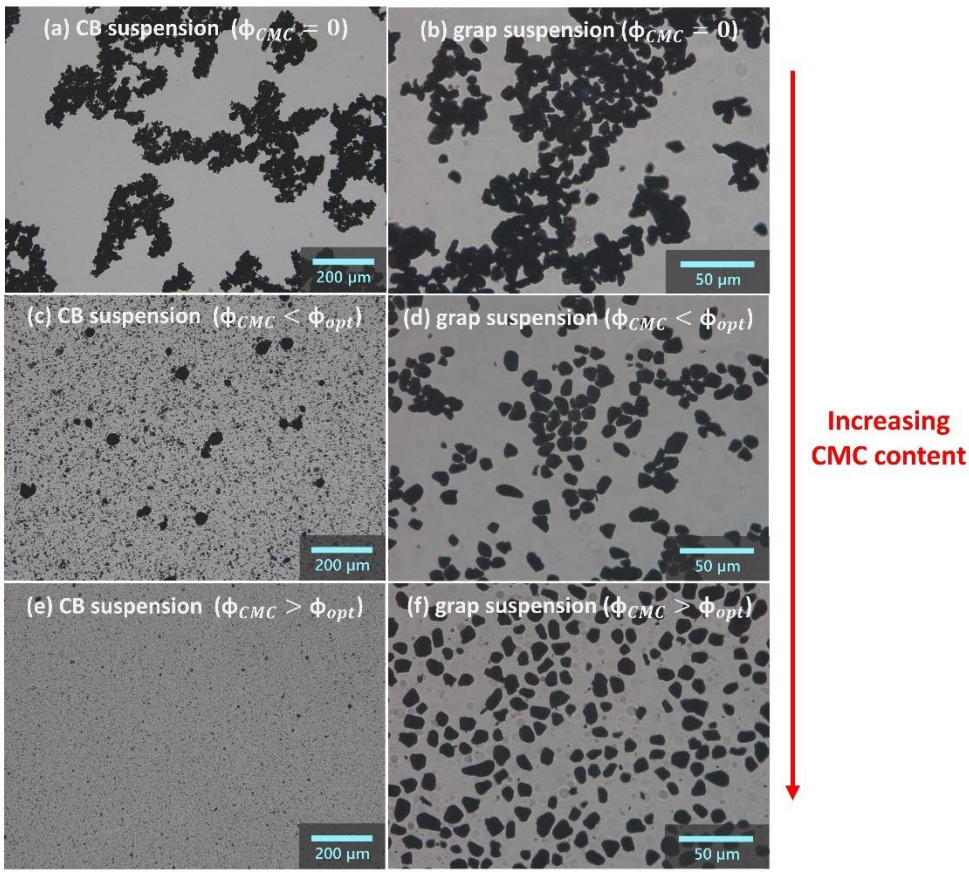

Figure 2.5. Optical micrographs of 5 wt% CB suspensions with (a) no CMC, (b) CMC 0.2 wt% (below optimum graft density), and (c) CMC 5.0 wt% (above optimum graft density). Optical micrographs of 45 wt% graphite suspension with (d) no CMC, (e) CMC 0.1 wt% (below

optimum graft density), and (f) CMC 5.0 wt% (above optimum graft density). The CB suspension was diluted 10 times while the graphite suspension was diluted 15 times with DI water.

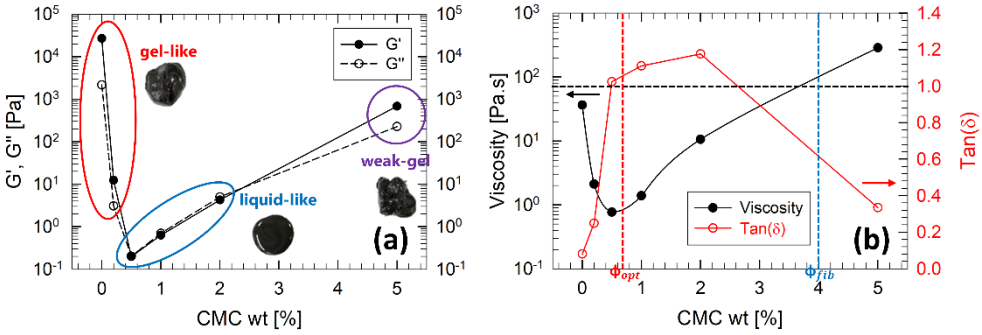

Figure 2.6. (a) Storage and loss modulus of the anode slurries (graphite 36 wt%, CB 1.8 wt%) at frequency = 1 rad/s with varying CMC content. (b) Viscosity (shear rate = 1 s^{-1}, closed symbol, left) and tan(δ) = G''/G' (frequency = 1 rad/s, open symbol, right) of the anode slurries (graphite 36 wt%, CB 1.8 wt%) with varying CMC content. The red dashed line represents the line with tan(δ) = 1.

Figure 2.6a shows G' and G'' (frequency = 1 rad/s) of anode slurries with varying CMC content. In the absence of CMC, G' of the anode slurry is of the order of ten thousand with frequency independence, indicating a gel-like behavior. The G' of the anode slurry is larger than that of CB (5 wt%) and graphite (45 wt%) suspension (Figure 2.1), even though the particle content is lower than that of each suspension. This is because CB and graphite particles with hydrophobic surface agglomerate together to form a volume-spanning network. The role of CMC in the anode slurry is similar to that in the CB and graphite suspensions.

Below the CMC content of optimum graft density, the adsorption

of CMC dominates the change in the dispersion state of the anode slurry. Figure 2.6b shows the viscosity (shear rate = 1 s^{-1}) and tan(δ) = G”/G’ (frequency = 1 rad/s) of the anode slurry with varying CMC content. Between CMC 0.5 and 1.0 wt%, the CMC content becomes an optimum graft density with the minimum viscosity. In particular, the CMC content (0.5 ~ 1.0 wt%) of the optimum graft density in the anode slurry is similar to the sum of the CMC content of the optimum graft density in the CB (W_{CMC}/W_{CB} = 0.2) and graphite ($W_{CMC}/W_{graphite}$ = 0.0024) suspensions (CMC 0.6 wt% (for CB) + CMC 0.15 wt% (for graphite) ~ CMC 0.75 wt%). This is because the two particles have similar surface properties (dispersive and polar component of surface energy [63, 64] and the same adsorption mechanism of CMC (hydrophobic interaction) [56]. Therefore, as the CMC content increases to 0.5 wt%, the two particles are more dispersed by the adsorbed CMC, resulting in a rapid decrease in G’ and inversion of G’ and G”. In other words, at CMC 0.5 wt%, it crosses tan(δ)~1, indicating a transition from solid-like to liquid-like state. As the CMC content increases from 1.0 wt% to 2.0 wt%, tan(δ) increases and is still larger than 1, indicating a liquid-like behavior. As in the CB and graphite suspensions, the CMC adsorbed to the two particles acts as a dispersant, and the free CMC remaining after adsorption acts as a thickener to increase the viscosity of the continuous phase. As the CMC content further increases to 5.0 wt%, G’ increases sharply and G’ and G” are reversed again. In other words, tan(δ) becomes lower than 1 again, indicating a transition from liquid-like to solid-like characteristics. As free CMC forms a 3D-fibrillar network, CMC acts as a gelling agent. Therefore, the anode slurry exhibits a weak-gel behavior ($G' \sim \omega^{0.21}, G'' \sim \omega^{0.29}$) as in the CB and graphite suspensions.

The change in the microstructure of the anode slurry with increasing CMC content can also be confirmed from the optical micrographs in Figure 2.7. In the absence of CMC (Figure 2.7a), graphite and CB particles together form a network structure by hydrophobic interactions. At CMC content below the optimum graft density of the slurry (Figure 2.7b), some graphite and CB particles are dispersed by the adsorbed CMC while others are aggregated. At CMC content of close to or above the optimum graft density of the slurry (Figure 2.7c and d), both particles are uniformly dispersed by the adsorbed CMC. In addition, the change of the slurry with increasing CMC content is clearly observed even with naked eye (Figure 2.8).

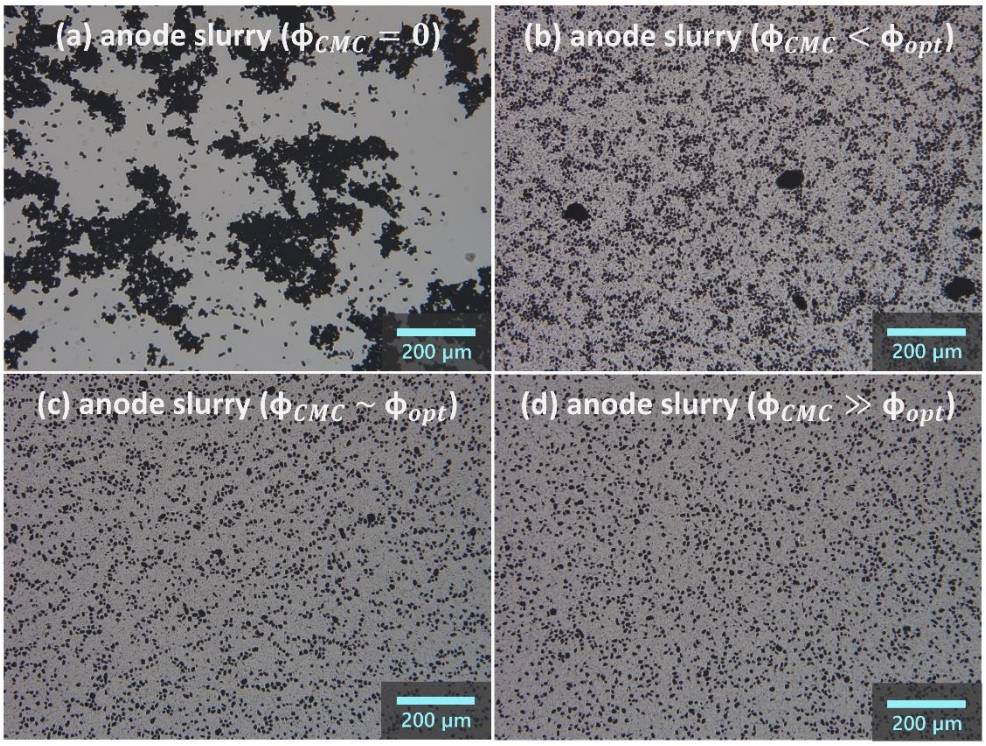

Figure 2.7. Optical micrographs of the anode slurries (graphite 36 wt%, CB 1.8 wt%) with (a) no CMC (b) CMC 0.2 wt% (below optimum graft density) and (c) CMC 1.0 wt% (near optimum graft density) and (d) CMC 5.0 wt% (above optimum graft density). Anode

slurries were diluted 15 times with DI water.

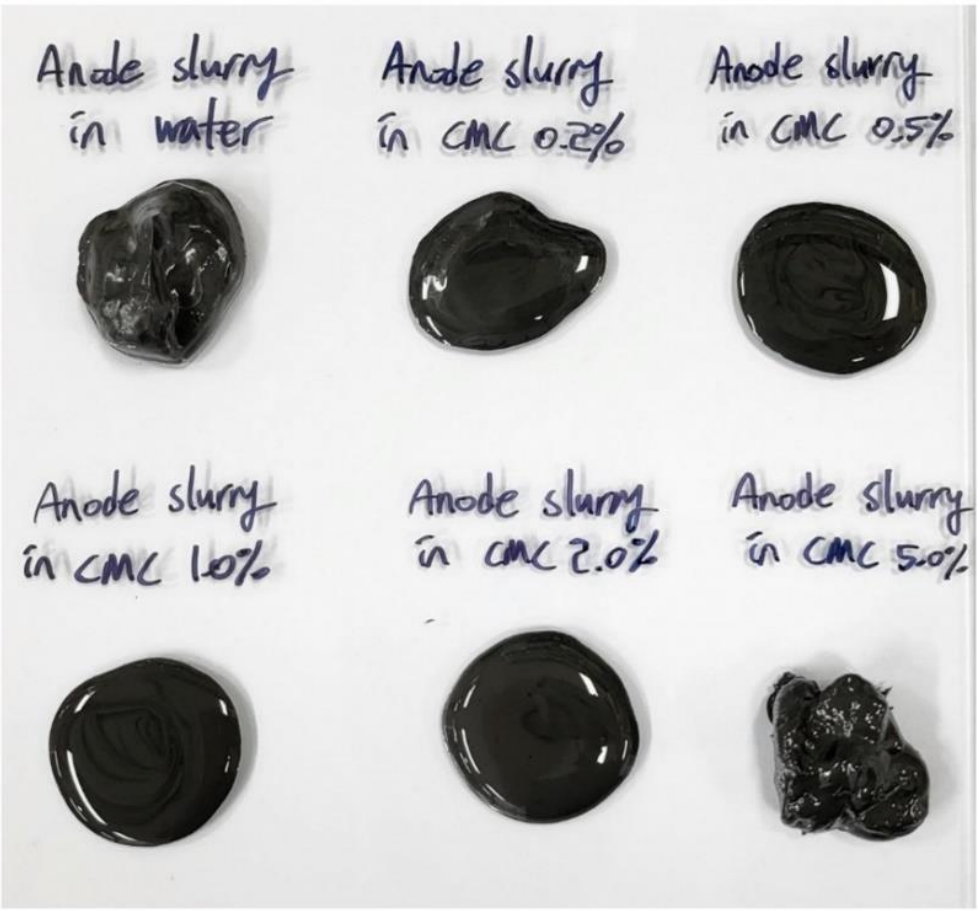

Figure 2.8. Images of the anode slurries (graphite 36 wt%, CB 1.8 wt%) with varying CMC content.

2.3.2. Effect of the preparation process on the slurry dispersion with respect to CMC content

The change in the rheological properties and microstructure of the anode slurry with respect to the CMC content is similar to that of the CB and graphite suspensions. In addition, the CMC content at the optimum graft density in the anode slurry is similar to the sum of the CMC content at the optimum graft density in each of the CB and

graphite suspensions. These are because the surface properties of the two particles and the adsorption and stabilization mechanism of CMC are similar. Based on these observations, it can be thought that the adsorption selectivity of CMC for the two particles (CB, graphite) changes depending on the mixing sequence of CMC and the two particles, leading to significant changes in slurry dispersion. It is well known that the selective adsorption of polymers affects the dispersibility of colloidal suspensions[65–67]. Here we design three different preparation processes of the slurry to confirm the above logics.

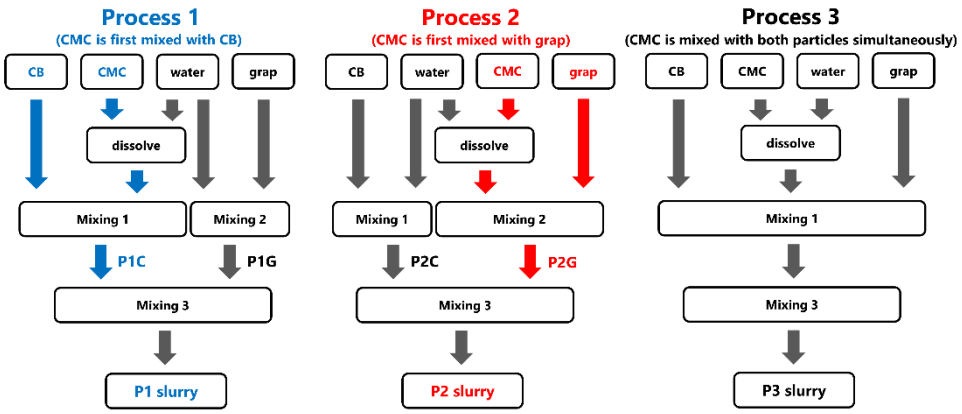

Figure 2.9. Three anode slurry preparation processes with different mixing sequence of CMC and the two particles (graphite, CB). Mixing 1 disperses the CB particles (in Process 3, both CB and graphite particles) at 6,000 rpm for 10 min using a homogenizer. Mixing 2 disperses the graphite particles at 1,000 rpm for 10 min using a mechanical stirrer. Mixing 3 is the final mixing of CB and graphite suspensions at 1,000 rpm for 10 min using a mechanical stirrer.

Figure 2.9 shows the three preparation processes of the anode slurry. The mixing sequence of CMC and the two particles (graphite,

CB) is different for each process. In Process 1, CMC is first mixed with CB particles in Mixing 1 (adsorbed to CB first) and then mixed with graphite particles in Mixing 3. In Process 2, CMC is first mixed with graphite particle in Mixing 2 (adsorbed to graphite first) and then mixed with CB particles in Mixing 3. In Process 3, CMC is mixed with both particles simultaneously (simultaneously adsorbed to CB and graphite). The CB suspension after Mixing 1 in Process 1 is named P1C, and the graphite suspension after Mixing 2 in Process 1 is named P1G. The anode slurry in which P1C and P1G are mixed (Mixing 3) in Process 1 is named P1 slurry. The suspensions and the slurries in Process 2 and 3 are named in the same way. Note that CMC exists in P1C and P2G, but not in P1G and P2C.

The effect of CMC mixing sequence on slurry dispersion should be understood in relation to the CMC content as CMC plays various roles depending on its content. Thus, we investigate the effect of the CMC mixing sequence on the rheological properties and microstructure of the slurry under the following two conditions; (1) CMC content is lower than the optimum graft density (CMC 0.13 wt%, in line with a recent trend to reduce binder content) [56, 68−70], and (2) CMC content is higher than the optimum graft density (CMC 1.90 wt%, content used for conventional anode slurry) [71−74]. The particle content is fixed at graphite 36 wt% and CB 1.8 wt% as in Figure 2.6 of chapter 2.3.1.

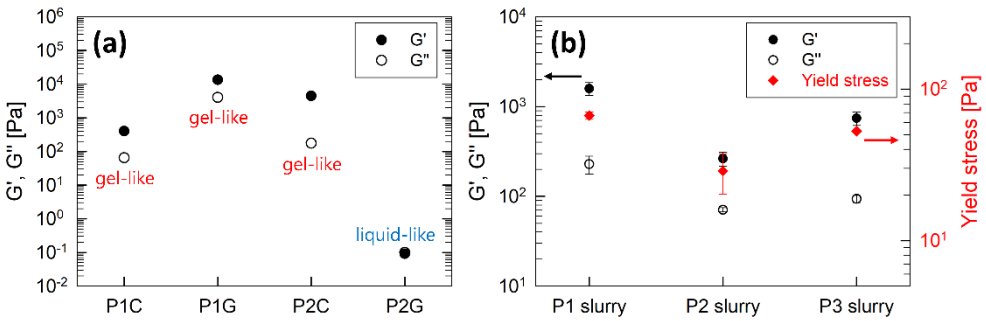

Figure 2.10. CMC content (0.13 wt%) lower than the optimum graft density; (a) Storage and loss modulus of P1C, P1G, P2C, and P2G at frequency = 1 rad/s. (b) Storage and loss modulus (circular symbol, at frequency = 1 rad/s), and yield stress (diamond symbol) of P1, P2, and P3 slurries (graphite 36 wt%, CB 1.8 wt%, CMC 0.13 wt%).

Figure 2.10a and b shows the rheological properties of P1C, P2C (CB suspension) and P1G, P2G (graphite suspension) (Figure 2.10a), and P1, P2, and P3 slurries (Figure 2.10b) when the CMC content (0.13 wt%) is lower than the optimum graft density (~0.75 wt%) of the slurry. Note that the CMC content (0.13 wt%) is too low to disperse all graphite and CB particles in P1, P2, and P3 slurries. It can disperse about 90% of the graphite particles when adsorbed only to graphite, or about 20% of the CB particles when adsorbed only to CB.

Figure 2.10a shows G' and G" of P1C, P1G, P2C, and P2G after mixing 1 and 2. In Process 1, P1C (W_{CMC}/W_{CB} = 0.044) and CMC-free P1G show a gel-like behavior, suggesting a network structure of hydrophobic particles. In Process 2, CMC-free P2C shows a gel-like behavior while P2G ($W_{CMC}/W_{graphite}$ = 0.0022) shows a liquid-like behavior, indicating that most of the graphite particles are stabilized by the adsorbed CMC. The microstructures of P1C, P1G,

P2C, and P2G are shown in Figure 2.11. Figure 2.10b shows G', G" (frequency = 1 rad/s) and yield stress of P1 slurry, P2 slurry, and P3 slurry after Mixing 3. P1, P2, and P3 slurries show a gel-like and yielding behavior. However, it is to be noted that the G' and the yield stress show a large difference of about one order of magnitude (P1 slurry>P3 slurry>P2 slurry). Although the composition is the same, the rheological properties of the slurry are strongly affected by the CMC mixing sequence.

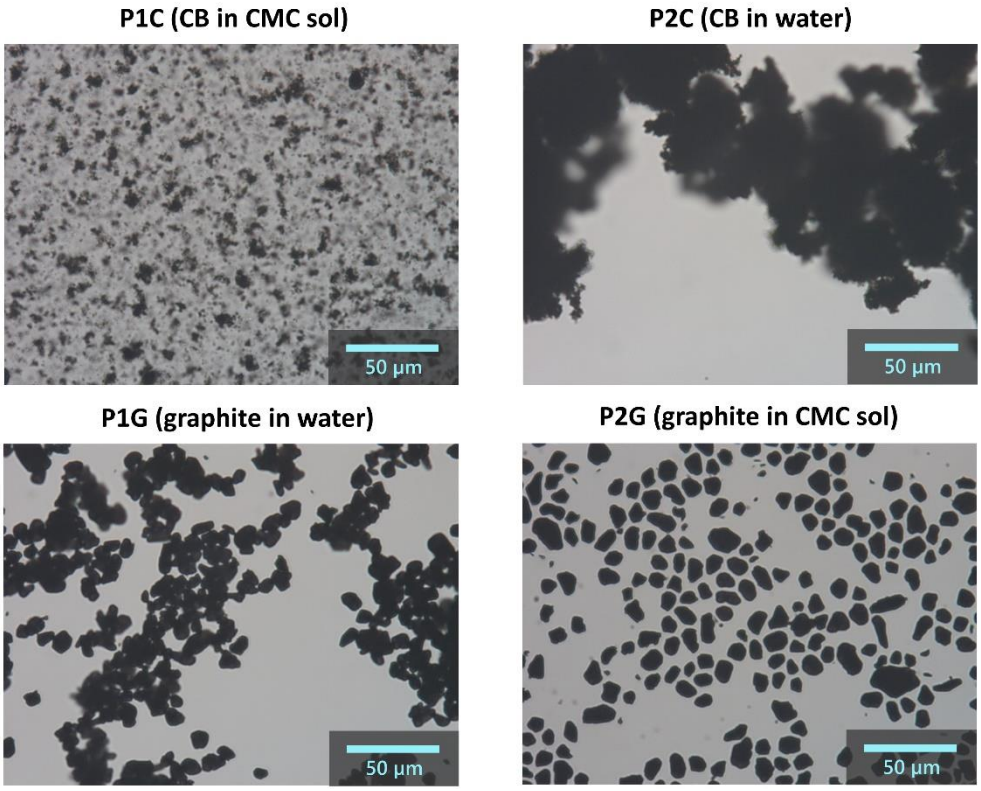

Figure 2.11. Optical micrographs of the (a) P1C, (b) P2C, (c) P1G, and (d) P2G when the CMC content (0.13 wt%) is lower than the optimum graft density.

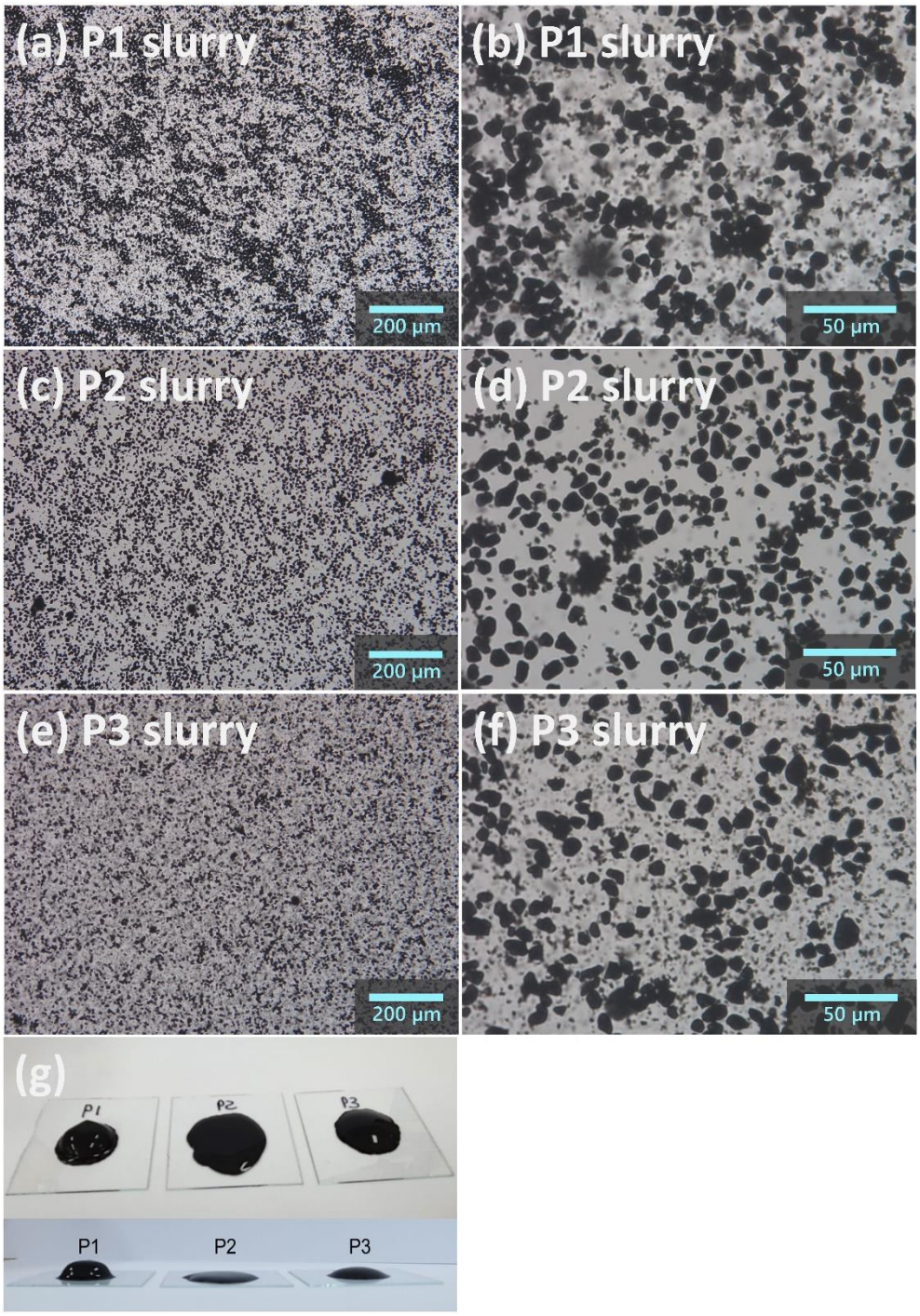

Figure 2.12. CMC content (0.13 wt%) lower than the optimum graft density. Optical micrographs of the anode slurries; (a, b) P1 slurry, (c, d) P2 slurry, and (e, f) P3 slurry. (a), (c), and (e) are low

magnification (10X) images, and (b, (d), and (f) are high magnification (50X) images. Each slurry was diluted 15 times with DI water. (g) Images of P1, P2, and P3 slurries when the CMC content (0.13 wt%) is lower than the optimum graft density.

When the CMC content is lower than the optimum graft density of the slurry (0.13 wt%), the CMC mixing sequence significantly affects the microstructure of the slurry as can be observed in optical micrographs (Figure 2.12). At low magnification (Figure 2.12a, c and e), the network structure of the agglomerated graphite particles is clearly observed in the P1 slurry (Figure 2.12a) as opposed to the P2 (Figure 2.12c) and P3 (Figure 2.12e) slurries. The structural difference of graphite particles is more evident at high magnification (Figure 12b, d and f). Among the graphite particles, the number of dispersed particles (graphite) without agglomeration (i.e. not in contact) is found 8.7% for P1 slurry (Figure 12b), 63.2% for P2 slurry (Figure 12d), and 41.5% for P3 slurry (Figure 12f). These suggest that the dispersibility of graphite particles is in the order of Process 2>Process 3>Process 1. On the other hand, since well-dispersed CB exists in the form of aggregates with a size of 100-300 nm composed of primary particles (<50 nm) [75], it is difficult to directly observe CB aggregates with this magnification. However, the relative dispersibility of CB can be estimated by detecting the cloudiness of the matrix or the presence of the agglomerates larger than a micron in size. For example, in Figure 2.5 (optical micrographs of CB suspension), the matrix is completely transparent when CMC does not exist and CB particles agglomerate to form a volume-spanning network (Figure 2.5a). On the other hand, the matrix becomes cloudy when CB is dispersed into aggregates by the

adsorbed CMC (Figure 2.5c and e). In addition, when the CMC content is lower than the optimum graft density, CB agglomerates with a size of several tens of microns are observed (Figure 2.5c), in contrast to the CMC content above the optimum graft density (Figure 2.5e). In the P2 slurry, the matrix is transparent (Figure 2.12d) and undispersed CB agglomerates with a size of several tens of microns are observed frequently (Figure 2.12c). On the other hand, in the P1 slurry, the matrix is quite cloudy (Figure 2.12b) and CB agglomerates larger than a few microns are observed less frequently (Figure 2.12a). In the P3 slurry, the cloudiness of the matrix (Figure 2.12f) appears to be in between P1 and P2 slurries. These observations imply that the dispersibility of CB particles is in the order of Process 1>Process 3>Process 2. From the dispersion state of the two particles, it can be said that the amount of CMC adsorbed to graphite is in the order of Process 2>Process 3>Process 1 while the amount of CMC adsorbed to CB is in the order of Process 1>Process 3>Process 2. Even after final mixing (Mixing 3), most of the CMC is selectively adsorbed to the pre-adsorbed (first adsorbed) particle among CB and graphite particles in Mixing 1 and 2. When CMC is adsorbed on both particles simultaneously (Process 3), the amount of CMC adsorbed to the two particles is between Process 1 and Process 2. The difference of P1, P2, and P3 slurries can clearly be observed even by the naked eye as shown in Figure 2.12g.

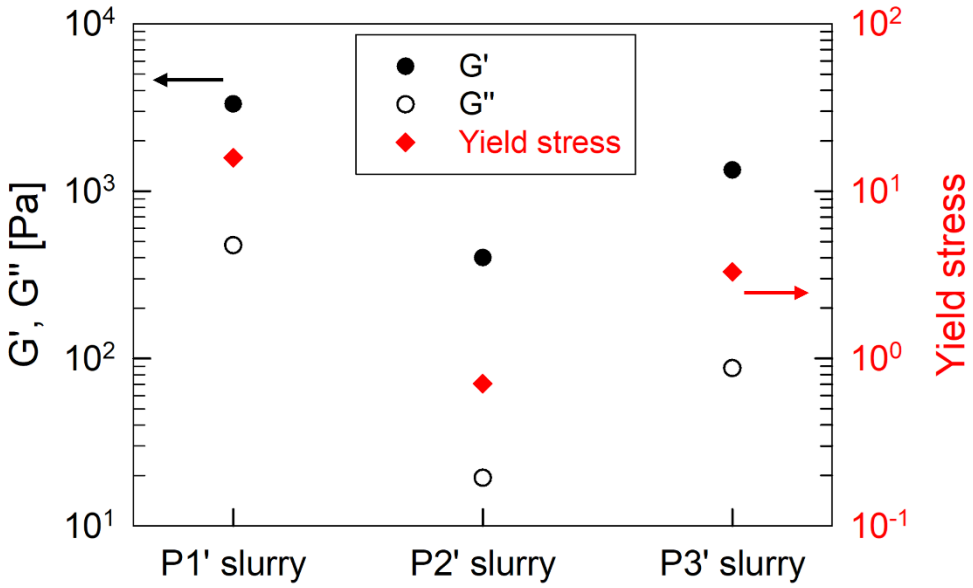

Figure 2.13. Storage and loss modulus (circular symbol, at frequency = 1 rad/s), and yield stress (diamond symbol) of P1'(graphite 36 wt%, CB 1.41 wt%), P2'(graphite 2.67 wt%, CB 1.8 wt%), and P3' (graphite 19.2 wt%, CB 1.61 wt%) slurries at frequency = 1 rad/s.

At CMC content lower than the optimum graft density, the two particles of the anode slurry exist in two dispersion states (1) well-dispersed particles by adsorbed CMC and (2) particles that are not adsorbed by CMC and agglomerate to form a network structure. As discussed in chapter 2.3.1, the elasticity (or yield stress) of the slurry is mainly due to the structure formed by (2) than (1). Therefore, in Figure 2.10b (or Figure 2.12), assuming that complete selective adsorption of CMC occurs, we can predict whether selective adsorption occurs in the P1, P2, and P3 slurries by comparing the elasticity (or yield stress) of the slurries composed solely of the particle content not adsorbed by CMC (particle content of slurry - particle content adsorbed by CMC) in the P1, P2, and P3 slurries.

Assume that all CMCs (0.13 wt%) selectively adsorb only to CB for the P1 slurry, only to graphite for the P2 slurry, and half (0.065 wt%) to both particles for the P3 slurry. At this time, the slurries composed of particle content not adsorbed by CMC are called the P1', P2', and P3' slurries. Figure 2.13 shows the G', G", and yield stress of P1', P2', and P3' slurries. The P1', P2', and P3' slurries show gel-like and yielding behaviors like the P1, P2, and P3 slurries. Furthermore, not only the magnitude of G' and yield stress appears in the order of P1'>P3'>P2' slurry, following the trend of P1>P3>P2 slurry, but the G' value for each process is similar. This is clear evidence that the differences in rheological properties and microstructure of P1, P2, and P3 slurries are due to the selective adsorption of CMC according to the preparation process.

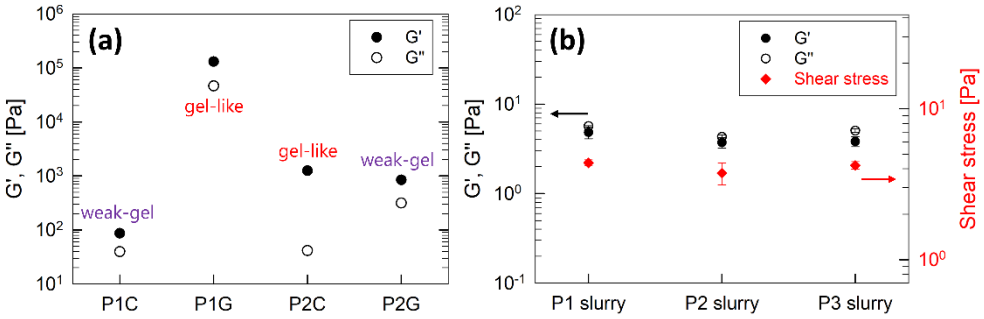

Figure 2.14. CMC content (1.9 wt%) higher than the optimum graft density; (a) Storage and loss modulus of P1C, P1G, P2C, and P2G at frequency = 1 rad/s. (b) Storage and loss modulus (circular symbol, at frequency = 1 rad/s), and shear stress (diamond symbol, at shear rate = 0.1s^{-1}) of P1, P2, and P3 slurries (graphite 36 wt%, CB 1.8 wt%, CMC 1.9 wt%).

Figure 2.14a and b shows the rheological properties of P1C, P2C and P1G, P2G (Figure 2.14a), and P1, P2, and P3 slurries (Figure

2.14b) when the CMC content (1.9 wt%) is higher than the optimum graft density of the slurry. Note that the CMC content (1.9 wt%) is sufficient to adsorb and disperse all the graphite and CB particles in P1, P2, and P3 slurries.

Figure 2.14a shows G' and G" of P1C, P1G, P2C, and P2G after mixing 1 and 2. In Process 1, P1C (W_{CMC}/W_{CB} = 0.65) shows a weak-gel behavior indicating a fibrillar network of CMC while P1G without CMC shows a gel-like behavior indicating the presence of a network structure of graphite particles. In Process 2, P2C without CMC and P2G ($W_{CMC}/W_{graphite}$ = 0.033) show a gel-like behavior and weak-gel behavior, respectively, for the same reasons as P1G and P1C. The microstructures of P1C, P1G, P2C, and P2G are shown in Figure 2.15. Figure 2.14b shows G', G" (frequency = 1 rad/s) and shear stress (shear rate = $0.1s^{-1}$) of P1, P2, and P3 slurries after Mixing 3. P1, P2, and P3 slurries show a liquid-like behavior without yield stress. However, when the CMC content is higher than the optimum graft density (Figure 2.14b), the mixing sequence of CMC rarely influences the rheological properties of the slurry, unlike the slurries with a CMC content lower than the optimum graft density (Figure 2.10b).

The microstructure of the three slurries looks similar (uniform dispersion of CB and graphite particles) as can be seen in the optical micrographs (Figure 2.16), suggesting that the CMC mixing sequence rarely influence the slurry microstructure. The shapes of the three slurries are also similar (Figure 2.16g), unlike the CMC content lower than the optimum graft density.

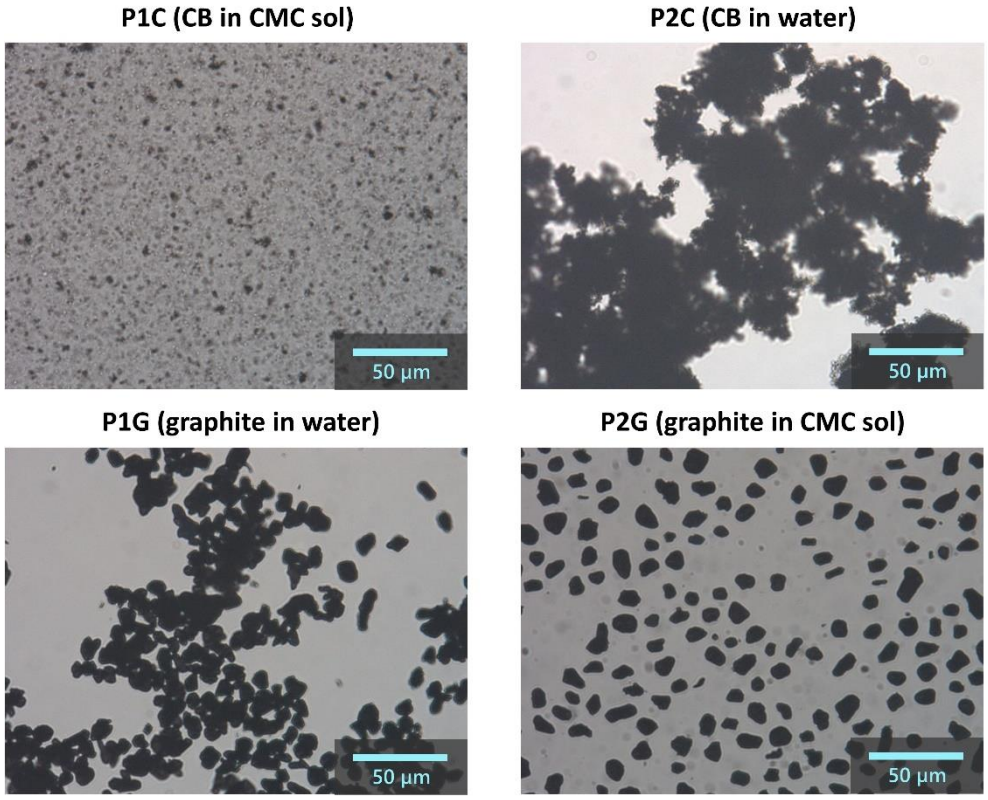

Figure 2.15. Optical micrographs of the (a) P1C, (b) P2C, (c) P1G, and (d) P2G when the CMC content (1.9 wt%) is higher than the optimum graft density.

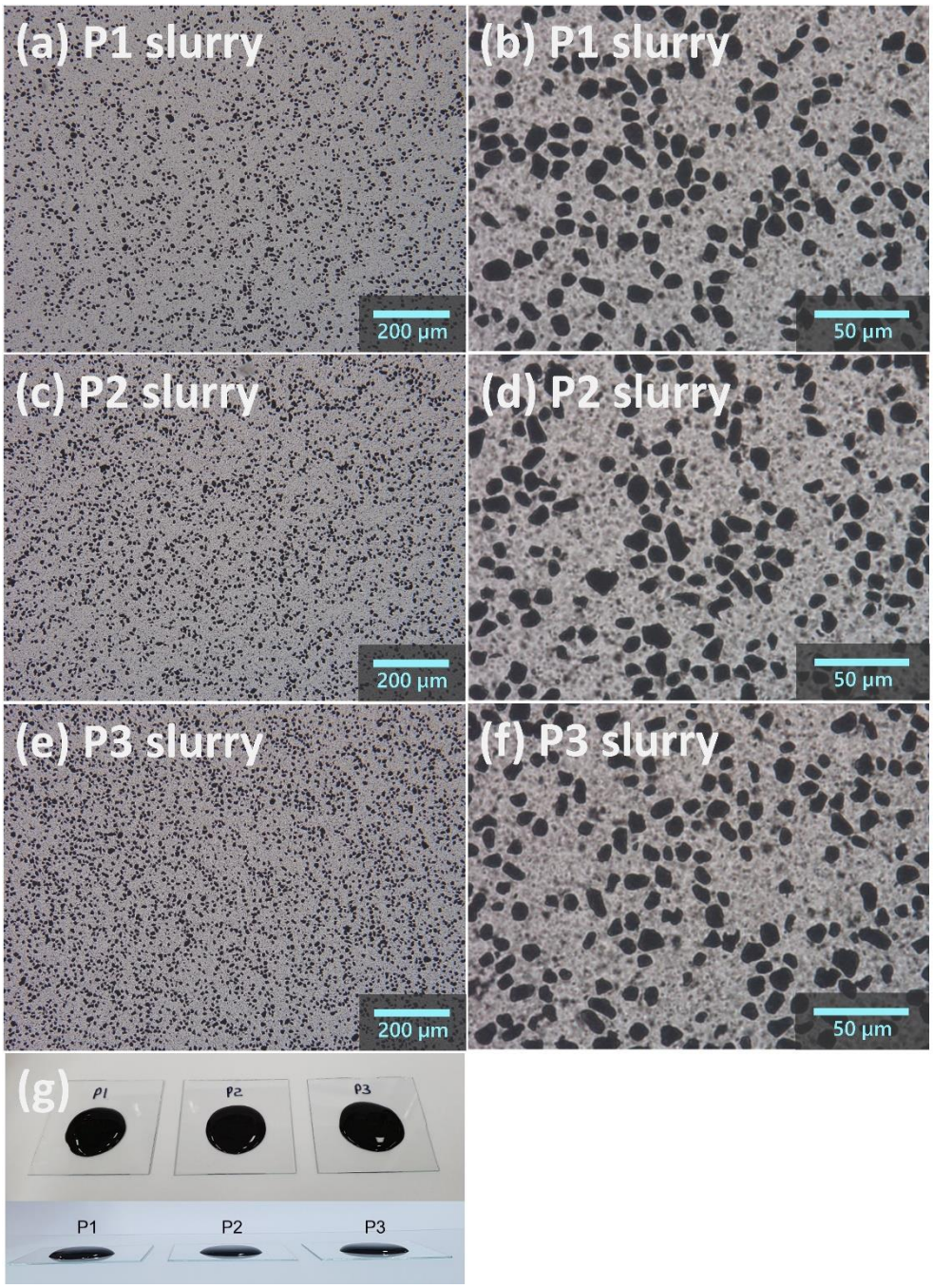

Figure 2.16. CMC content (0.13 wt%) higher than the optimum graft density. Optical micrographs of the anode slurries; (a, b) P1 slurry, (c, d) P2 slurry, and (e, f) P3 slurry. (a), (c), and (e) are low magnification (10X) images, and (b, (d), and (f) are high magnification (50X) images. Each slurry was diluted 15 times with

DI water. (g) Images of P1, P2, and P3 slurries when the CMC content (1.9 wt%) is lower than the optimum graft density.

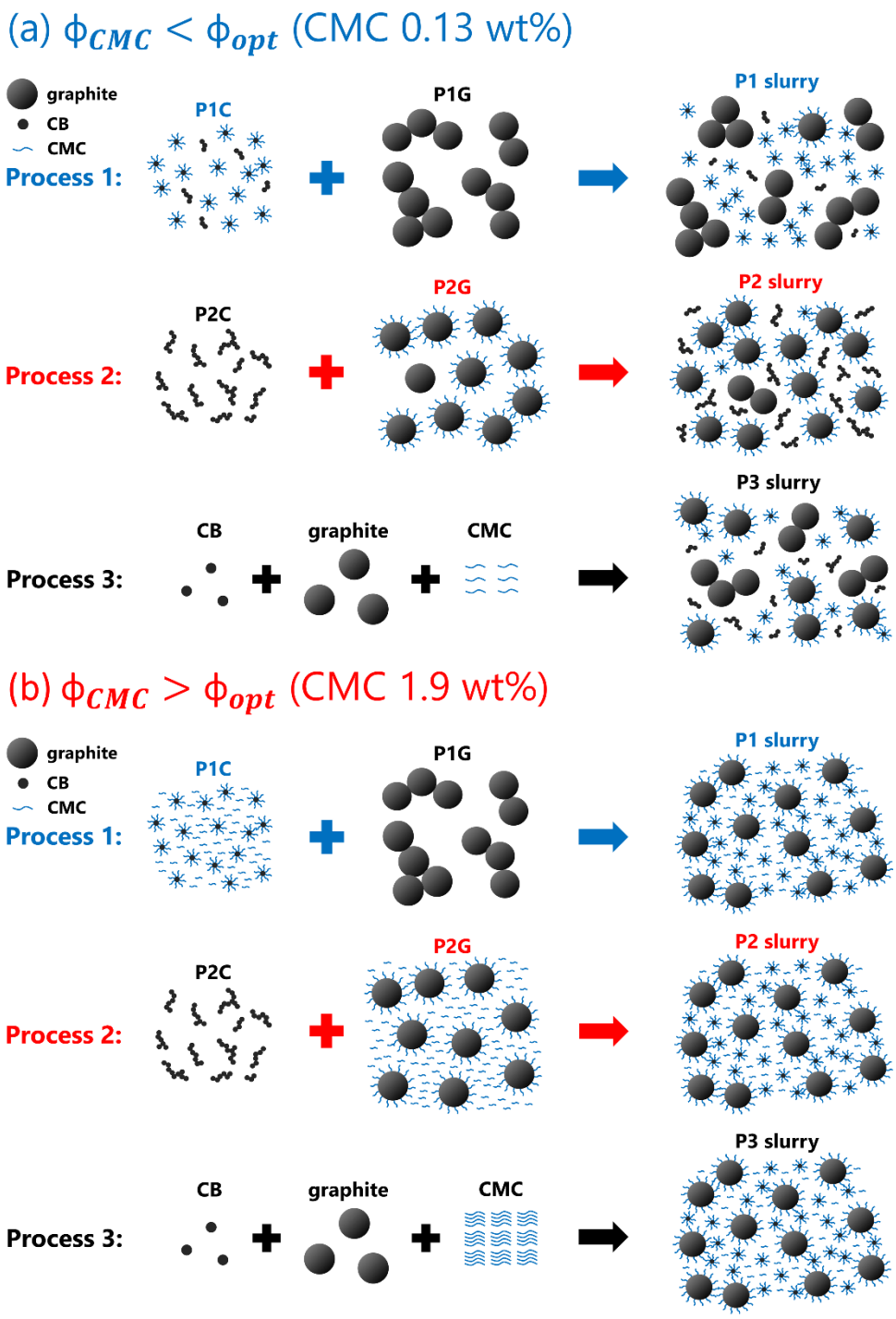

Figure 2.17. Schematic of the mechanism of the slurry microstructure

change according to the CMC mixing sequence.

The mechanism of the changes in slurry microstructure according to the CMC mixing sequence can be understood by considering the role of CMC in each preparation and the adsorption selectivity of CMC. Figure 2.17 shows the microstructure change mechanism of the slurry according to the CMC mixing sequence. When the CMC content of the anode slurry is lower than the optimum graft density (CMC 0.13 wt%, Figure 2.10 and Figure 2.17a), in P1C and P2G after Mixing 1 and Mixing 2, all CMCs are adsorbed and grafted onto the particle (CB in P1C, graphite in P2G) and free CMC does not exist. Even after final mixing (Mixing 3) with another particle (graphite in P1G, CB in P2C) introduced later, most of the grafted CMC (in P1C and P2G) is still selectively adsorbed to the pre-adsorbed particle and acts as a dispersant of that particle. Therefore, even with the same CMC content, the slurries exhibit different microstructures as the adsorption selectivity is different depending on the CMC mixing sequence. On the other hand, when the CMC content is higher than the optimum graft density (CMC 1.9 wt%, Figure 2.14 and Figure 2.17b), in P1C and P2G after Mixing 1 and Mixing 2, a portion of the CMC is grafted onto the particles (as much as the adsorption saturation), but excess CMC exists as a free polymer in the matrix. Unlike grafted CMC, which acts as a dispersant, free CMC present in P1C and P2G, which acts as a thickener or gelling agent, adsorbs to another particle introduced later during Mixing 3 and acts as a dispersant of that particle. Therefore, the slurry microstructure is rarely affected by the mixing sequence of CMC as both particles are eventually fully adsorbed by CMC in the final mixing (Mixing 3) stage.

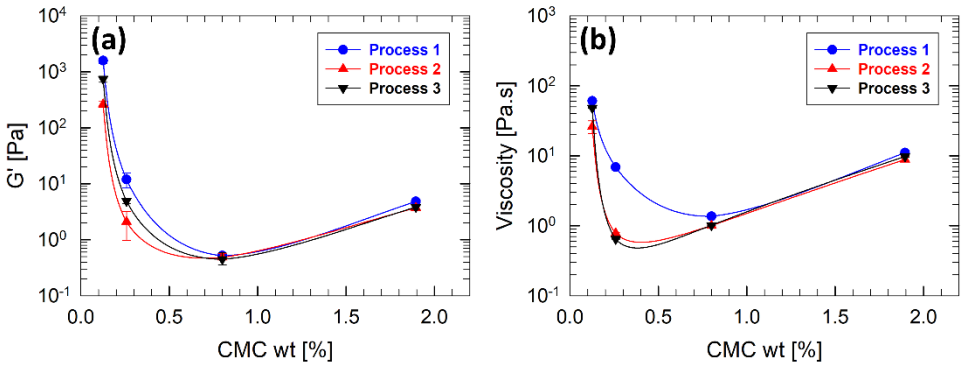

Figure 2.18. (a) Storage modulus (frequency = 1 rad/s), and (b) viscosity (shear rate = $1s^{-1}$) of the anode slurries according to the slurry preparation process (CMC mixing sequence) as a function of CMC content (CMC 0.13 wt%, 0.26 wt%, 0.80 wt%, and 1.9 wt%).

Figure 2.18 shows the storage modulus (Figure 2.18a) and viscosity (Figure 2.18b) of the anode slurries according to the CMC mixing sequence as a function of CMC content. At a CMC content lower than the optimum graft density of the anode slurry (~0.75 wt%), CMC mixing sequence has a significant effect on the rheological properties (storage modulus and viscosity) of the slurry, as it affects adsorption selectivity of CMC for the two particles. The difference between CMC 0.26 wt% and CMC 0.13 wt% is that some free CMC is present in P2G after Mixing 2 at CMC 0.26 wt%. However, the amount of free CMC in P2G (at CMC 0.26 wt%) is insufficient to fully adsorb and disperse the CB particles introduced later (Mixing 3), which leads to a difference in the adsorption selectivity of the slurry after final mixing stage. On the other hand, at a CMC content higher than the optimum graft density, CMC mixing sequence rarely affects the rheological properties of the slurry as both particles are adsorbed and saturated by CMC in the final mixing stage.

2.4. Conclusion

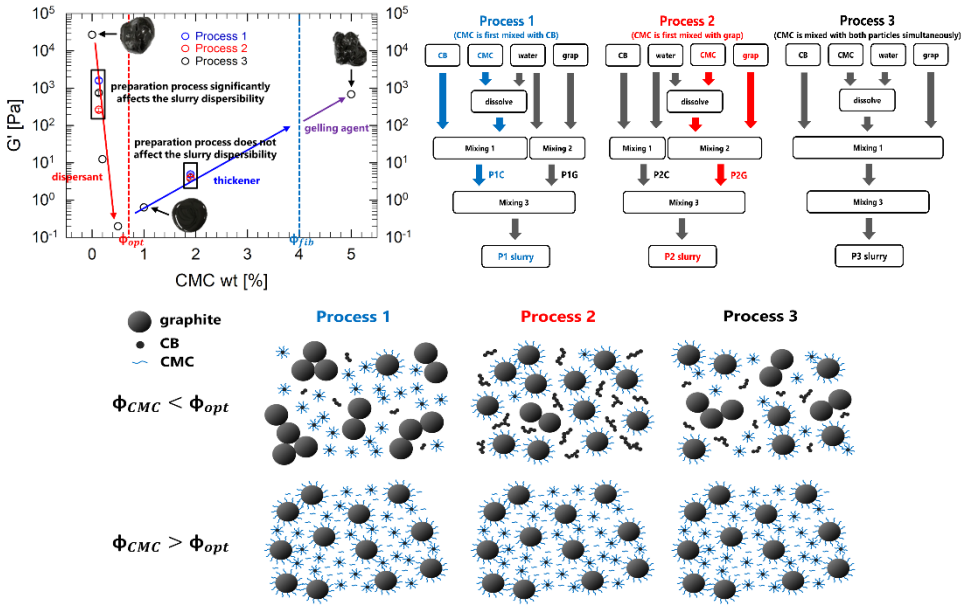

Figure 2.19. Schematic of the role of CMC and how it affects the slurry preparation process.

In this chapter, we systematically investigated the various roles of CMC and their effect on the preparation process in terms of the interactions between each component in the anode slurry that contains both active and conductive particles. Figure 2.19 summarizes the role of CMC and how it affects the slurry preparation process depending on the CMC content.

CMC plays various roles in the anode slurry depending on the content and significantly influences slurry dispersibility. CMC acts as a dispersant at lower content than the optimum graft density at which adsorption is saturated. When the CMC content increases above the optimum graft density, the adsorbed CMC acts as a

dispersant and the extra free CMC acts as a thickener. However, when the content increases further and the free CMC forms a fibrillar network, the CMC acts as a gelling agent. Therefore, with increasing CMC content, the rheological properties of the slurry changes from a gel-like to liquid-like, and then back to weak gel-like behavior. In addition, CMC selectively adsorbs to the first mixed particle among the two particles (CB, graphite) in the anode slurry. Therefore, at a CMC content lower than the optimum graft density, the dispersibility of the slurry is strongly affected by the CMC mixing sequence even if the composition is the same. On the other hand, at a CMC content higher than the optimum graft density, the dispersibility of the slurry is rarely affected by the CMC mixing sequence even with the selective adsorption of CMC in the first mixing stage as both particles are eventually adsorbed and saturated in the final mixing stage.

Under the industrial trend of increasing the content of the active component and lowering the content of the inactive component, the dispersion behavior of low-binder content slurries becomes crucial. In terms of slurry transport, it would be beneficial to selectively adsorb CMC onto graphite to lower the viscosity, and in terms of conductivity, it would be advantageous to selectively adsorb CMC onto CB to form a conducting network structure. However, the significance of the findings is that slurry dispersion can be controlled for the desired purpose by simply changing the mixing sequence of the components, without altering the physiochemical properties of each component and the composition of the slurry.

Furthermore, the findings open up the possibility of controlling the slurry dispersion to suit each electrode process, such as slurry

preparation, storage, transport and coating stages, by desorbing and selectively re-adsorbing the CMC adsorbed in the mixing and dispersing stage, which would be beneficial for process optimization. The hydrophobic force (F_H) between CMC and CB, which is the driving force for the adsorption, is estimated to be $F_H \sim W_{CMC-CB} R_g \sim 8.26 * 10^{-9}\ (N)$ (where W_{CMC-CB} is work of adhesion between CMC and CB, as will be discussed in Chapter 4, and R_g is radius of gyration of CMC with a molecular weight of 250K), and the drag force (F_D) acting on the CMC chain, which is expected to mainly contribute to the desorption of the CMC chain, is estimated to be $F_{D,sphere} \sim 6\pi\mu R_g v \sim 2.96 * 10^{-9}\ (N)$ and $F_{D,cylinder} \sim 0.5 C_D \rho A v^2 \sim 3.69 * 10^{-9}\ (N)$, respectively, under the mixing condition of 1,000 rpm (laminar flow) in this study. These estimates assume that the CMC chain can be modeled as a sphere and a cylinder, respectively. To desorb the CMC, the drag force F_D needs to be larger than the hydrophobic force F_H. In the sphere case, an agitation speed of 2,800 rpm is required, while in the cylinder case, a speed of 48,000 rpm is needed for the desorption of CMC in the slurry preparation stage. As CMC adopts a stretched conformation in water due to its rigid backbone, the actual magnitude of the drag force for desorption might be in between the abovementioned forces. In slurry storage, transport, and coating stages, an equivalent force might be required for CMC desorption. The exact order of the force must be verified experimentally since various complexities, such as the flexibility and roughness of the CMC chain, the shape and surface properties of the particles, and the types of storage tank and pipe, hinder precise calculations. However, since additional energy is required for desorbing and re-adsorbing CMC in each electrode process, from the process optimization standpoint, the trade-off between the benefits

obtained by tuning the slurry dispersion and the economic loss due to energy consumption should be considered.

Based on our findings, we plan to evaluate the correlation between slurry dispersion and various electrode characteristics in the subsequent electrode process. We anticipate our findings provide useful insights in terms of controlling the slurry dispersibility, improving the electrode process design and productivity.

Chapter 3. Significant agglomeration of conductive materials and dispersion state change of Ni-rich NMC cathode slurries during storage

3.1. Introduction

The prepared electrode slurry is agitated in a storage tank to maintain the dispersion quality before entering the subsequent coating and drying process[76]. However, complex fluids such as electrode slurries can undergo structural changes by the flow. Therefore, even if well-dispersed slurries with target mechanical properties are prepared, any deterioration in slurry dispersion during storage may lead to various industrial problems, including surface defects, non-uniform coating thickness and electrode loading, clogging in pipes and filters, and foil breakage, to list a few. Therefore, it is of great industrial importance to understand the storage effect on the slurry dispersion.

However, efforts to understand the storage effect have been limited[76-78]. Kwon et al. argued that low-speed agitation during storage deteriorates the slurry dispersion, based on the observation that rheological properties of the slurry change more rapidly with agitation than without agitation. They claimed that low-speed agitation accelerated the network structure of active material

particles[76]. Wang et al. observed the structural change of the cathode slurry with storage time by changing the agitation speed through electrochemical impedance spectroscopy (EIS) analysis. At a high agitation speed, the resistance of the conductive path of the cathode slurry decreased with storage time while increasing at a low agitation speed. They claimed that the reason was due to the reduced dispersibility of the CB particles with agitation time at low agitation speed[77]. As a follow-up study, they characterized the two dispersion states of the cathode slurry at various agitation speeds through EIS analysis. At an agitation speed lower than the specific agitation speed, two semicircles appeared on the Nyquist plot, indicating a poor dispersion state where CB particles were aggregated and not well dispersed. Another dispersion state was observed at high agitation speed. At this time, a well-dispersed state where CB particles coat the active material particle and form a conducting network was defined, since only one semicircle appeared on the Nyquist plot[78]. Although limited studies have been conducted, it has not been revealed, during storage, how the slurry microstructure changes specifically, which parameter governs the change in slurry microstructure, and what is the underlying mechanism of the structural change.

In this study, we aim to investigate during storage, how the dispersibility of the cathode slurry changes by agitation, and which parameter governs the change in microstructure, along with the underlying mechanism. We investigate the changes in rheological properties and microstructure of the slurry under each storage condition, and the microstructure of the cathode after drying the slurry. At first, we observe that the conductive particles

significantly agglomerate under certain low-speed agitation, forming large spherical agglomerates whose size ranges several tens of μm. This leads to significant changes in rheological properties of the slurry. Then, to clarify the main parameter that causes the structural change, we simultaneously control the agitation speed and the matrix viscosity of the slurry. These two parameters can be integrated into the hydrodynamic stress. Finally, we correlate the changes in rheological properties and microstructure of the slurries with the hydrodynamic stress during storage. The mechanism of the structural change is understood by considering the relative affinity between each particle and the flow characteristics during storage.

3.2. Experimental section

3.2.1. Materials

$Li(Ni_{0.8}Mn_{0.1}Co_{0.1})O_2$ (NMC811, Shangdong Gelon Lib Co., Ltd, china) with a mean particle size of 10 μm and density of 4.7 g/cm^3 was used as a cathode active material. Acetylene black (a type of carbon black with highly purified and conductive) (AB, Denka black, Denka company limited, Japan) with an average particle diameter of 35 nm, density of 2.25 g/cm^3, surface area of 62 m^2/g according to the supplier was used as a conductive agent. For polymeric binder, two types of poly(vinylidene fluoride) homopolymer(PVDF, Solvay, Belgium) were used. The molecular weight of PVDF was 700,000 g/mol (solef 6020) and 320,000 g/mol (solef 6010), respectively. N-Methyl-2-pyrrolidone (NMP, Daejung, Korea) was used as a casting solvent.

3.2.2. Sample preparation

The cathode slurry was manufactured through the following procedure. Firstly, PVDF solution was prepared by adding a PVDF binder into NMP solvent and dissolving for 10 hours at 400 rpm using a magnetic stirrer. After that, AB (acetylene black) paste was prepared by adding AB particles to the prepared PVDF solution and dispersing it for 10 minutes at 10,000 rpm using a rotor-state homogenizer (Ultra-Turrax T18, IKA, Germany). Finally, the cathode slurry was manufactured by adding NMC, PVDF solution, and NMP into prepared AB paste, and then mixing for 5 minutes at 1,000 rpm using an anchor-type mechanical stirrer. The particle concentration of the prepared cathode slurry was NMC 25 vol % and

AB 1.5 vol %, and the PVDF concentration of two molecular weights were adjusted as in table 1 to control the matrix viscosity of the cathode slurry. The PVDF concentration was designed so that the two PVDF solutions with different molecular weight had similar but slightly different (about 10%) viscosity (matrix viscosity in the cathode slurry).

PVDF (700K)		PVDF (320K)	
Concentration (wt %)	viscosity (Pa.s)	Concentration (wt %)	viscosity (Pa.s)
2.5	0.040	5.0	0.045
3.5	0.080	6.8	0.090
5.0	0.230	9.6	0.250

Table 1. Viscosity of PVDF solution depending on the concentration and molecular weight of the PVDF binder.

The prepared cathode slurries were agitated at rotational speeds of 50, 100, 200, and 400 rpm for up to 3 hours using an anchor-type mechanical stirrer to simulate the storage conditions in the industrial electrode process. We confirmed that the rheological properties of the slurry reach equilibrium after 3 hours of storage. We also confirmed that the storage conditions covered in this study, including all matrix viscosities of the slurries and agitation speeds of the stirrer, correspond to laminar flow. A schematic diagram of storage tank and agitator with dimension was shown in Figure 3.1.

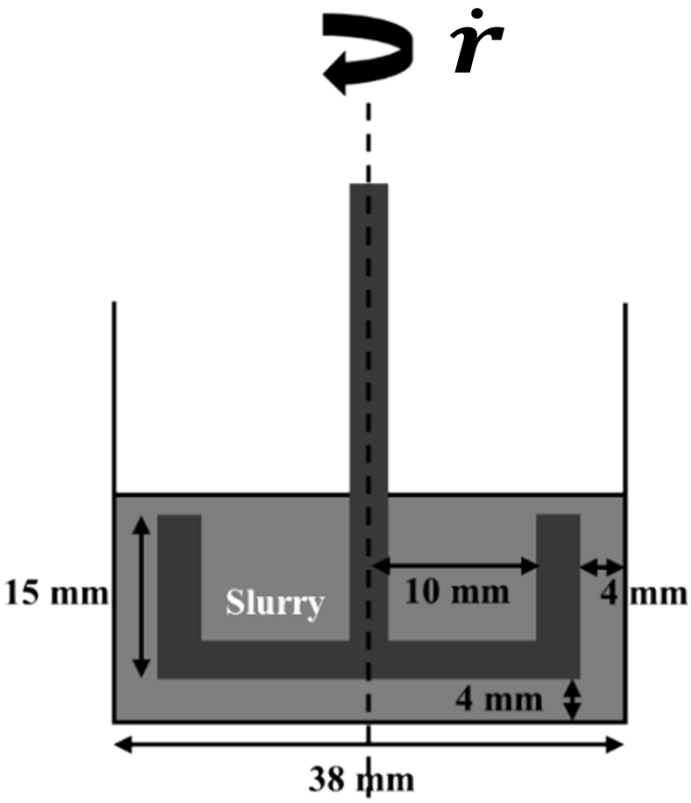

Figure 3.1. Schematic diagram of storage tank and stirrer with dimensions.

If the cathode slurry was stored without proper agitation, the NMC particles were seriously precipitated due to large density difference with the NMP solvent. Therefore, the physical properties of the cathode slurry stored without agitation were not dealt as reference sample. However, we confirmed that precipitation did not occur when the agitation (covered in this study, 50 ~ 400 rpm) was applied as shown in Figure 3.2.

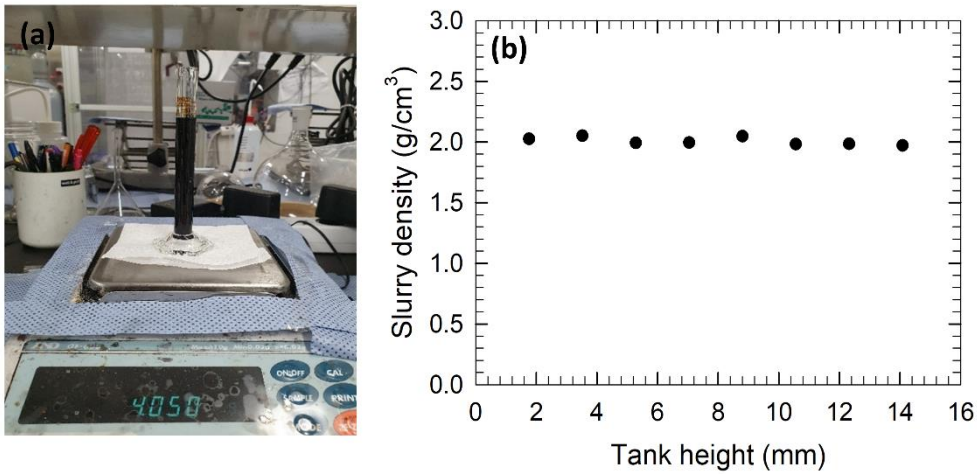

Figure 3.2. (a) Image of the slurry sampled after 3 hours of storage in a storage tank (b) slurry density as a function of tank height.

When the slurry density was calculated by sampling 2ml of the slurry from the top of the tank and then measuring the mass, there was little difference in slurry density as a function of tank height after low-speed agitation (50 rpm for 3 hours, storage condition where precipitation is most likely to occur). Moreover, we carefully checked that precipitation did not occur during storage.

In order to calculate the hydrodynamic stress caused by agitation, the rotational speed(rpm) of the stirrer was converted into an angular velocity through the following equation (eq 1)

$$w\left(angular\ velocity, \frac{rad}{s}\right) = \frac{revolution}{min}(rpm) \times \frac{min}{60s} \times \frac{2\pi\ rad}{revolution} \quad (1)$$

Hydrodynamic stress caused by agitation was calculated as the stress at the outside wall (maximum stress) through the following equation (eq 2)

$$\dot{\gamma} = \frac{Rw}{h}, \qquad \tau = \eta_m \dot{\gamma} \quad (2)$$

where $\dot{\gamma}$, h, R, η_m, τ are the shear rate, distance between the outside wall of the stirrer and the storage tank, distance from the center of the storage tank to the outside wall of the stirrer, matrix viscosity, and hydrodynamic stress, respectively. To prepare the electrode, the cathode slurry was coated on aluminium foil with a thickness of 200 μm at a coating speed of 10 mm/s using a ZAA 2300 automatic coater (Zehntner GmbH, Switzerland) and a ZUA 2000.60 doctor blade (Zehntner GmbH, Switzerland). Then, the coated slurry was dried at 80℃ for 24 hours in a convection oven. As NMP has a boiling point of 202℃, which is very high compared to water, it was dried at a sufficiently high temperature for a long time as in the literature. The composition of the electrode after drying was NMC 95.7 wt%, AB 2.7 wt%, and PVDF 1.6 wt%. The rheological properties and optical microscope images of the cathode slurries were obtained at agitating times of 1 hour and 3 hours.

3.2.3. Rheological characterization

The rheological properties of the cathode slurries were measured using a stress-controlled mode AR-G2 rheometer (TA instruments, New Castle, USA) with a 40-mm parallel plate fixture. The loading gap was set to 700 ~ 1000 μm depending on the initial loading condition of the cathode slurry. Before performing the frequency sweep, the sample was initialized by applying a pre-shear of 10 s^{-1} for 10 seconds after loading the sample. Then, the sample was equilibrated through a time-sweep for 3 minutes at angular frequency = 6.28 rad/s in a linear viscoelastic regime. The frequency sweep was performed by decreasing the angular frequency from 100 rad/s to 0.25 rad/s in the linear viscoelastic region.

3.2.4. Microstructure observation

Optical microscope images of the cathode slurry were obtained using a polarizing microscope (BX51, Olympus, Japan). In order to obtain OM images, the cathode slurry was diluted 6 times with NMP and mixed for 5 seconds using a vortex mixer (VM-10, Allforlab, Korea). Excessive dilution makes it difficult to observe the microstructure because the number of particles is too small, and it is difficult to observe dark materials optically with too little dilution, thus the most appropriate dilution factor of 6 was selected. Then, 0.1 ml of the diluted cathode slurry was carefully loaded onto a 24 x 50 mm^2 slide glass using a dropper, and a 22 x 22 mm^2 cover glass was placed on the sample, and then the optical microscope image was observed. The surface structure of the cathode was observed using a field emission scanning electron microscope (FE-SEM, SUPRA 55VP, Germany), and the cross-sectional microstructure of the cathode was observed using a focused ion beam scanning electron microscope (FIB-SEM, Helios 650, USA).

3.3. Results and discussion

3.3.1. Significant changes in rheological properties and microstructure of cathode slurries during storage

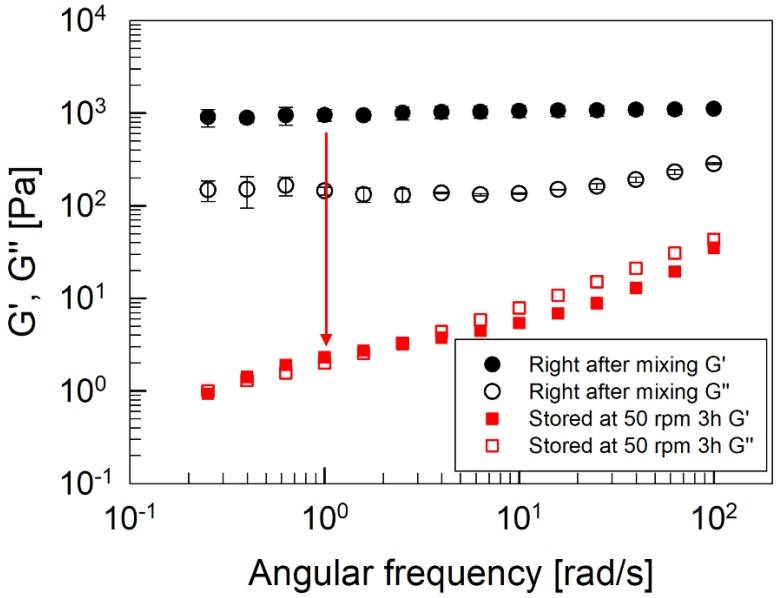

Figure 3.3. Storage (closed symbol) and loss (open symbol) modulus of cathode slurry (NMC 25 vol%, AB 1.5 vol%, PVDF 2.5 wt%) as a function of frequency depending on storage conditions: right after mixing (circular symbol), stored at 50 rpm for 3 hours (square symbol).

Figure 3.3 shows the frequency sweep results of the cathode slurry immediately after preparation (right after mixing) and the cathode slurry stored while agitating at 50 rpm for 3 hours. The cathode slurry right after mixing shows a G' value on the order of thousand with frequency-independent gel-like behavior in a wide range of frequencies. However, when it is stored at a low agitation

speed (50 rpm), the low frequency G' of the cathode slurry decreases dramatically, showing a liquid-like behavior. From the rapid change in rheological properties, a large change in the microstructure of the slurry can be expected.

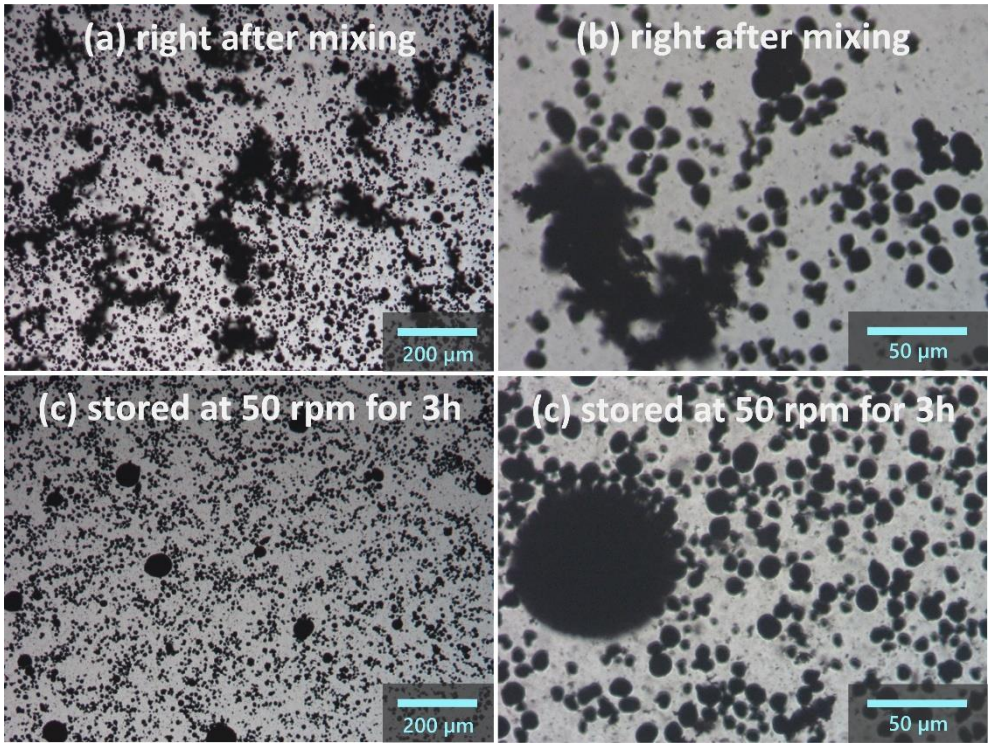

Figure 3.4. Optical microscopic images of cathode slurry(NMC 4.2 vol%, AB 1.25 vol%, PVDF 4.2 wt%): (a) & (b) right after mixing, (c) & (d) sheared at 50 rpm for 3 hours.

The structural change of the cathode slurry during storage can be confirmed by observing the OM images (Figure 3.4). In the slurry right after mixing (Figure 3.4a and b), AB and NMC particles form branched porous agglomerates throughout the samples. On the other hand, when this slurry is stored at 50 rpm for 3 hours (Figure 3.4c and d), the AB particles are restructured to form spherical agglomerates of tens of μm, which is larger than the active material.

The fractal dimensions of these two agglomerates are calculated to be **1.57(±0.03)** (value expected in diffusion-limited aggregation in 2D[79]) for NMC-AB branched agglomerates and **1.75(±0.02)** for AB spherical agglomerates, respectively, after image-processing the optical micrograph (Figure 3.4a and c) using the software Image J, based on the box-counting method. This result clearly shows the structure difference between two slurries.

In addition, even after drying, the microstructural difference between the two cathodes is clearly identified through scanning electron microscope (Figure 3.5). In the cathode made from the slurry of right after mixing (Figure 3.5a,c, and e), some AB particles are distributed on the surface of the active material particles, and the rest form the conductive paths between the active material particles. On the other hand, in the cathode made from the cathode slurry stored at 50 rpm for 3 hours (Figure 3.5b,d, and f), most of the AB particles form large spherical agglomerates of several tens of μm, as observed in the cathode slurry. This implies that the memory in the liquid phase remains even after drying. In particular, by observing the cross-sectional images of the AB agglomerates (Figure 3.5f), it is confirmed that the large spherical agglomerates do not contain NMC particles and consist only of AB particles. As such, if the conductive materials do not form an appropriate conductive network and are severely agglomerated, electrode failure problems may occur in the subsequent electrode process, leading to a drastic deterioration of the battery performance[80-82]. This structural change is a very dangerous storage variable.

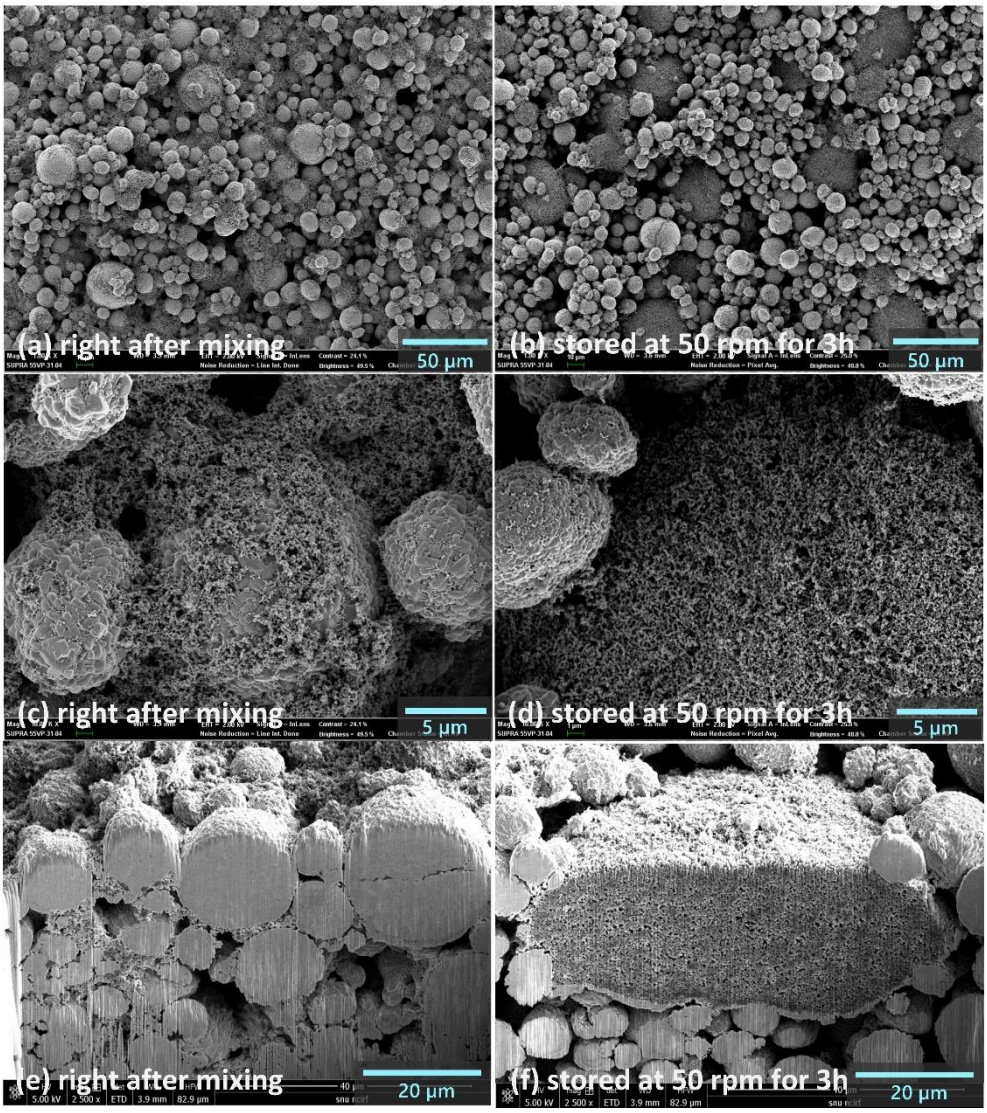

Figure 3.5. FE-SEM surface images of cathode (NMC 95.7 wt%, AB 2.7 wt%, PVDF 1.6 wt%): (a) & (c) right after mixing, (b) & (d) sheared at 50 rpm for 3 hour; FIB-SEM cross sectional images of the same cathode (NMC 95.7 wt%, AB 2.7 wt%, PVDF 1.6 wt%): (e) right after mixing, (f) sheared at 50 rpm for 3 hours.

3.3.2. Effect of agitation speed on the rheological properties of cathode slurry during storage

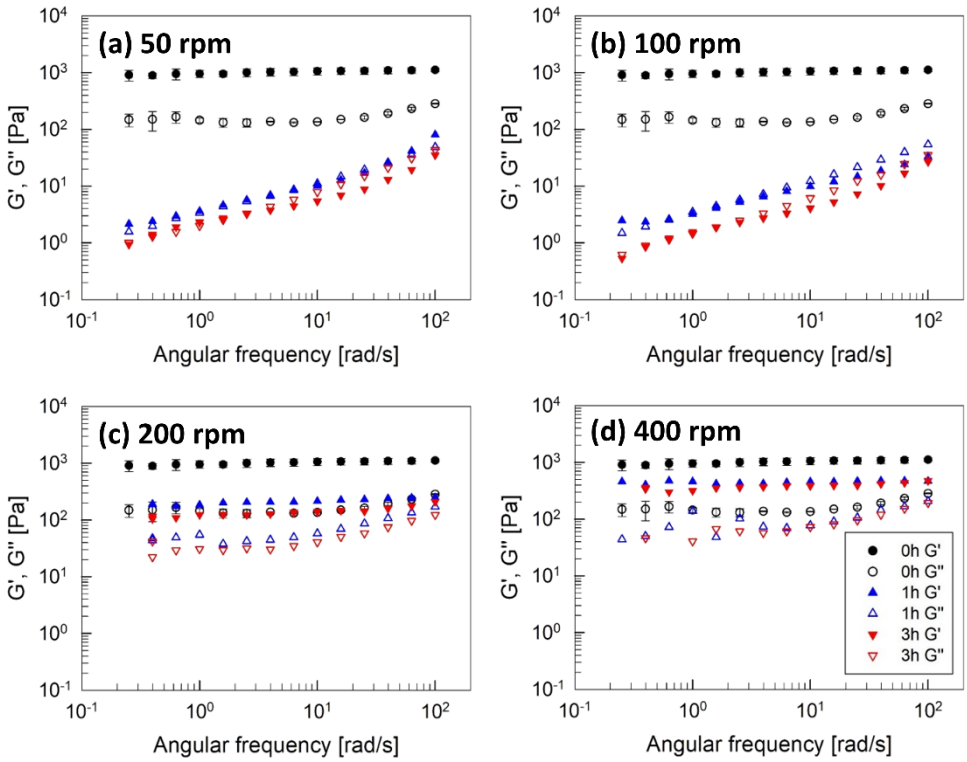

Figure 3.6. Storage (closed symbol) and loss (open symbol) modulus of cathode slurry (NMC 25 vol%, AB 1.5 vol%, PVDF 2.5 wt%) as a function of frequency under storage condition of (a) 50 rpm, (b) 100 rpm, (c) 200 rpm, and (d) 400 rpm.

Therefore, to clarify the main parameter that causes the structural change of the slurry, we investigate the changes in rheological properties of the slurry with varying agitation speed. Figure 3.6 shows the effect of agitation speed on the rheological properties of cathode slurry during storage as a function of storage time. The rheological properties of slurry during storage depend largely on the agitation speed. Under the storage conditions of 50

rpm (Figure 3.6a) and 100 rpm (Figure 3,6b), the low frequency G' value of the cathode slurry, which showed a gel-like behavior initially, decreases by about 3 orders of magnitude after 3 hours of storage. On the other hand, in the storage conditions of 200 rpm (Figure 3.6c) and 400 rpm (Figure 3.6d), although the G' slightly decreases, it is still larger than the G" and the cathode slurry still shows a frequency-independent gel-like behavior after 3 hours of storage. Although not disclosed here, we confirm that AB particles form large spherical agglomerates when the G' of the slurry decreases rapidly and the slurry shows a liquid-like behavior, as in the storage condition of 50 and 100 rpm. The experimental results imply that the cathode slurry reaches a different dispersion state (liquid-like or gel-like) after storage condition of a specific agitation speed.

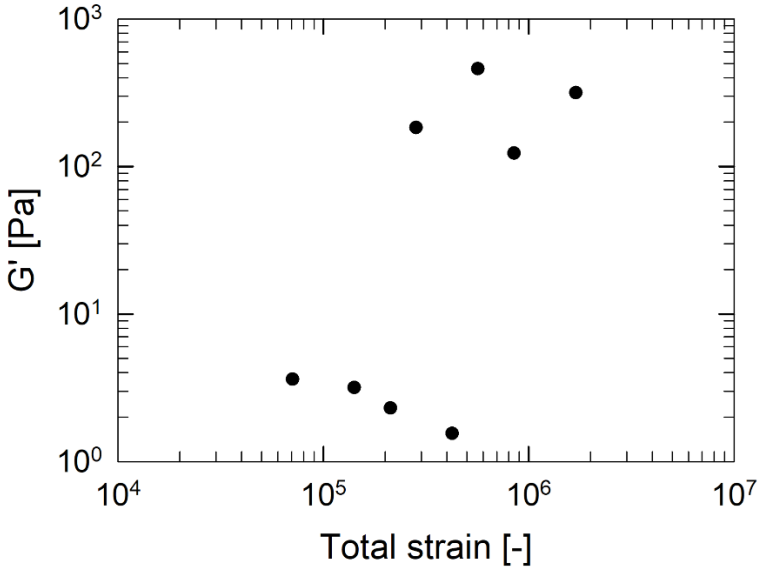

Figure 3.7. Storage modulus (G') of cathode slurry (at angular frequency = 1 rad/s) as a function of total strain during storage at each agitation speed and storage time covered in Figure 3.6.

There are many parameters that cause the structural change of the colloidal gel, such as cathode slurry. However, it is well-known that in the flow field, strain or hydrodynamic stress play a major role in causing changes in microstructure of the colloidal gel[83-85]. At first, we confirm that there is no correlation between G' of the slurry and total strain under each agitation speed (50, 100, 200, and 400 rpm) and storage time (1 and 3 h) covered in Figure 3.6, as shown in Figure. 3.7. Therefore, we simultaneously control the matrix viscosity of the slurry and agitation speed of the agitator and investigate the effect of hydrodynamic stress on the rheological properties of the slurry during storage. The product of these two variables (matrix viscosity and agitation speed) can be integrated into the hydrodynamic stress. We confirm that PVDF solutions show Newtonian behavior in which the viscosity does not show shear-dependence in the investigated ranges of concentration and molecular weight of PVDF binder (Figure 3.8). Furthermore, we also confirm that PVDF hardly affects the interaction between the particles of cathode slurry (NMC, AB) based on the observation that changes in the concentration and molecular weights of the PVDF binder does not significantly affect the elastic part (G') but has a major effect on the viscous part (G") of the cathode slurry (Figure 3.9). Therefore, we control the matrix viscosity of the slurry by varying concentration and molecular weight of PVDF binder (shown in Table 1).

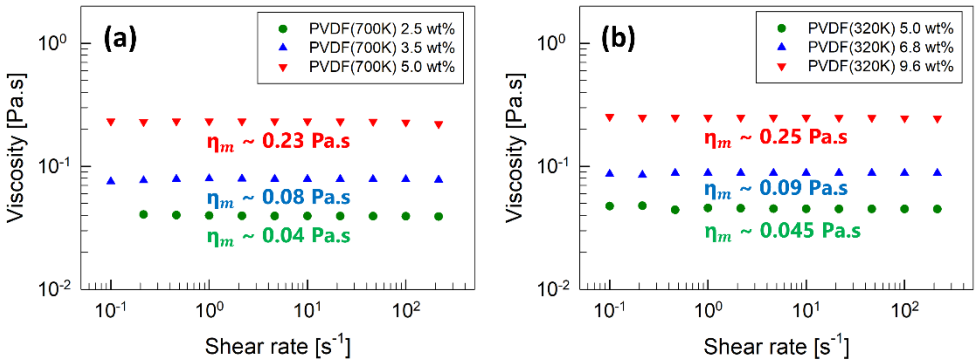

Figure 3.8. Flow curves of (a) PVDF (700K) solution, and (b) PVDF (320K) solution.

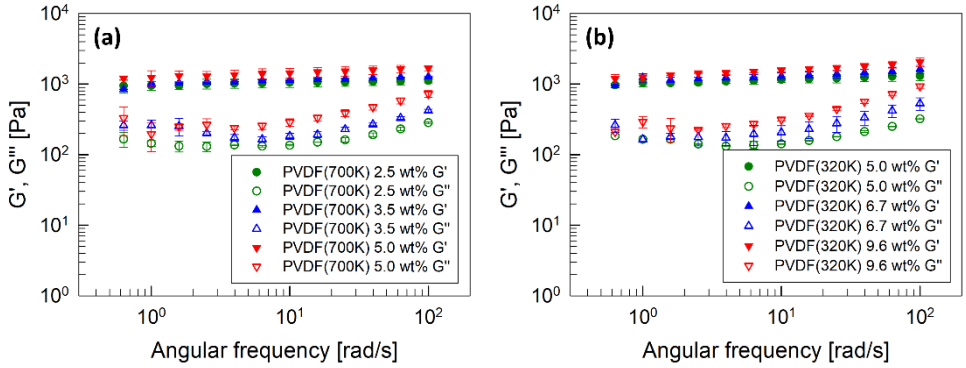

Figure 3.9. Storage (closed symbol) and loss (open symbol) modulus of cathode slurry (NMC 25 vol%, AB 1.5 vol%) as a function of frequency: (a) PVDF(700K) (b) PVDF(320K).

3.3.3. Effect of matrix viscosity on the rheological properties of cathode slurry during storage

Figure 3.10 shows the change in G' (angular frequency = 1 rad/s) of various cathode slurries at different matrix viscosity (Table 1) with respect to the agitation speed and the storage time. As the concentration of PVDF (700K) changes (Figure 3.10a,c and e), the

rheological properties of the slurry change differently with the agitation speed. When the matrix viscosity is 0.04 Pa.s (PVDF(700K) 2.5 wt%, Figure 3.10a), the G' sharply decreases with the storage time under the storage conditions below 100 rpm (50 rpm and 100 rpm), so that the cathode slurry shows a liquid-like behavior. This suggests that the AB particles form large spherical agglomerates. At storage conditions of 200 rpm or higher (200 rpm, 400 rpm), the G' slightly decreases with the storage time, but the cathode slurry still shows a frequency-independent gel-like behavior. However, when the concentration of PVDF (700K) increases and the matrix viscosity is 0.08 Pa.s (PVDF(700K) 3.5 wt%, Figure 3.10c), sharp decrease in the G' value is observed only under the storage condition of 50 rpm. Under the storage conditions of 100 rpm or higher (100, 200, and 400 rpm), the cathode slurry shows a gel-like behavior. As the concentration of PVDF further increases and the matrix viscosity reaches 0.24 Pa.s (PVDF(700K) 5.0 wt%, Figure 3.10e), an abrupt decrease in G' value is not observed at all storage conditions (50, 100, 200, and 400 rpm) and the cathode slurry shows a gel-like behavior.

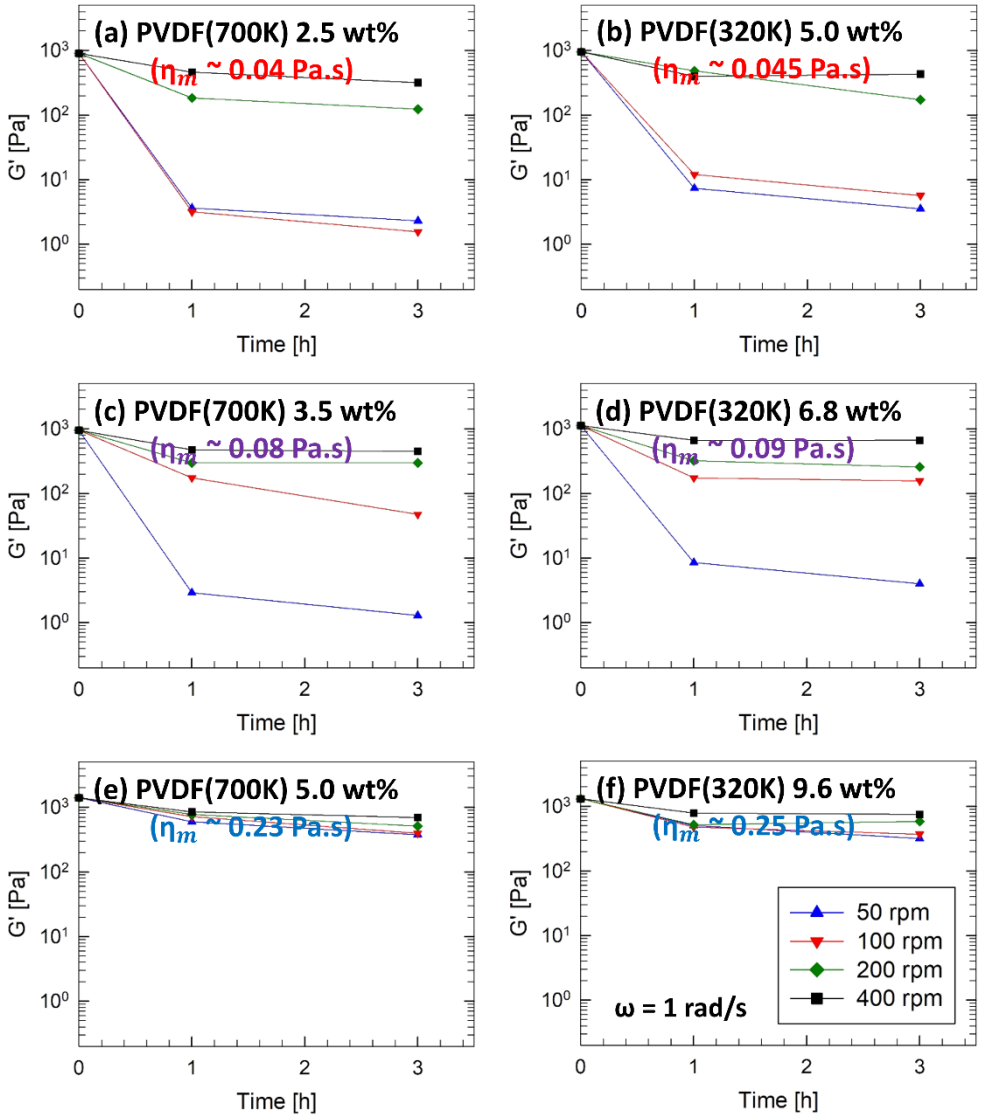

Figure 3.10. Rotational speed dependence of storage modulus (at angular frequency = 1 rad/s) of the cathode slurries (NMC 25 vol%, AB 1.5 vol%) with different binder (matrix viscosity) conditions: (a) PVDF(700K) 2.5 wt%, (b) PVDF(320K) 5.0 wt%, (c) PVDF(700K) 3.5 wt%, (d) PVDF(320K) 6.8 wt%, (e) PVDF(700K) 5.0 wt%, (f) PVDF(320K) 9.6 wt%.

Surprisingly, even when a lower molecular weight PVDF(320K) is used (Figure 3.10b,d and f), the same trend is observed after 3 hours of storage as in the slurry with high molecular weight PVDF(700K). When the matrix viscosity is 0.045 Pa.s (PVDF(320K) 5.0 wt%, Figure 3.10b), the G' rapidly decreases and the agglomeration of AB particles is observed under the storage conditions of 100 rpm or less. The cathode slurry exhibits a gel-like behavior under the storage conditions of 200 rpm or higher, although the G' slightly decreases. When the concentration of PVDF(320K) increases and the matrix viscosity is 0.09 Pa.s (PVDF(320K) 6.8 wt%, Figure 3.10d), the G' sharply decreases only under the storage condition of 50 rpm, and the cathode slurry shows a gel-like behavior under the storage conditions of 100 rpm or higher. As the PVDF(320K) concentration further increases and the matrix viscosity reaches 0.25 Pa.s (PVDF(320K) 9.6 wt%, Figure 3.10f), no abrupt change in G' is observed under all storage conditions and the cathode slurry shows a gel-like behavior.

The experimental results show that the critical shear rate (the critical rpm where the elasticity of the cathode slurry begins to decrease rapidly with storage time) is inversely proportional to matrix viscosity of the slurry. In particular, when the matrix viscosity is doubled for each case of PVDF(320K) and PVDF(700K), the critical shear rate decreases by half. In addition, the critical shear rate is the same when the matrix viscosity is similar, regardless of the concentration and molecular weight of PVDF binder. Therefore, it can be concluded that hydrodynamic stress, which is the product of agitation speed and matrix viscosity, governs the changes in rheological properties and microstructure of the slurry

during storage. This result is in line with the previous study by Rwei et al. that the critical shear rate for breaking up CB agglomerate is inversely proportional to the fluid viscosity [86].

3.3.4. Changes in rheological properties and dispersion state of cathode slurry due to hydrodynamic stress

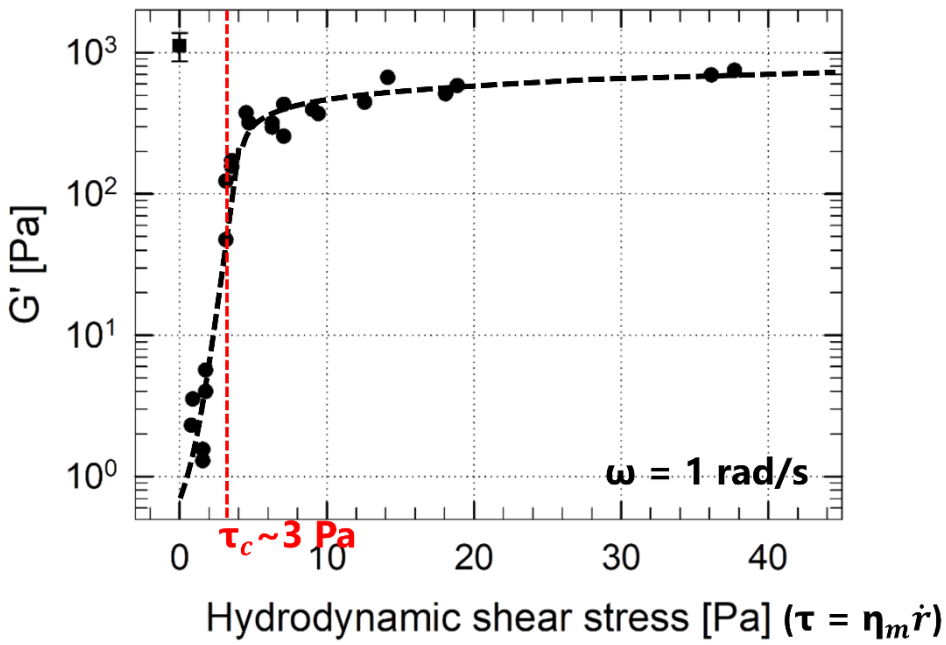

Figure 3.11. Storage modulus (at angular frequency = 1 rad/s) of the cathode slurries (NMC 25 vol%, AB 1.5 vol%, PVDF(700K) 2.5, 3.5, and 5.0 wt%, and PVDF(320K) 5.0, 6.8, and 9.6 wt%) after 3 hours of agitation at 50, 100, 200, and 400 rpm as a function of hydrodynamic shear stress(product of matrix viscosity and shear rate).

Figure 3.11 shows the G' (at angular frequency = 1 rad/s) of the slurry after 3 hours of storage under all storage conditions of agitation speed and matrix viscosity covered in Figure 3.10, as a

function of hydrodynamic stress, which is the product of the agitation speed and matrix viscosity. The G' before storage is indicated by a square symbol while the G' after storage for 3 hours under agitation are indicated by circular symbols. In the cathode slurry immediately after preparation (square symbol), AB nanoparticles form branch type agglomerates together with NMC particles (Figure 3.4a and b) and the cathode slurry exhibits a gel-like behavior. When the cathode slurry is stored with agitation for 3 hours, it reaches a different dispersion state (liquid-like or gel-like) before and after storage condition of a critical hydrodynamic stress $(\tau_c \sim 3\ Pa)$ (Figure 3.11). Under the storage conditions of stress lower than the critical hydrodynamic stress, the elasticity of the cathode slurry rapidly decreases as the AB particles form large spherical agglomerates and the cathode slurry shows a liquid-like behavior. On the other hand, under the storage conditions of the critical hydrodynamic stress or higher, the cathode slurry still shows a gel-like behavior, although the G' slightly decreases. In addition, as the hydrodynamic stress caused by agitation increases, the G' increases and then converges to a limiting value, which is close to the one right after mixing.

In order to understand the change in the rheological properties and microstructure of the slurry due to the flow characteristics (agitation), we must understand the interaction of each component in the cathode slurry and the physical properties of the colloidal gel. In the previous study, we confirmed that the PVDF binder in the NMP-based cathode slurry plays a major role in increasing the matrix viscosity without significantly affecting the interaction between the cathode active materials and the conductive particles [20]. Therefore, the surface properties of the active material and the

conductive particles become crucial in terms of microstructure formation in the slurry. However, the cathode active material and the conductive particle show quite different surface properties. According to the surface energy of LCO cathode material and carbon black obtained from the sessile drop method by Ludwig et al.[63], LCO has dispersive surface energy (VDW interaction) of 12.75 mN/m and polar surface energy (coulomb interaction) of 37.57 mN/m, whereas carbon black shows 56.27 mN/m and 0.54 mN/m, respectively. Using these values, the affinity between the particles can be calculated by using the Fowkes equation[87] (eq 3)

$$W_{ij} = 2(\gamma_i^d \gamma_j^d)^{0.5} + 2(\gamma_i^p \gamma_j^p)^{0.5} \quad (3)$$

where γ_i^d and γ_j^d are the dispersive surface energy of materials i and j, γ_i^p and γ_j^p are the polar surface energy of materials i and j, respectively. As a result of the calculation, the work of cohesion (affinity between the same materials, W_{CB-CB}) is 113.62 mN/m and the work of adhesion (affinity between different materials, W_{LCO-CB}) is 62.58 mN/m. Therefore, from the thermodynamic point of view, CB particles have a strong tendency to aggregate by themselves rather than aggregate with the active materials (although the author does not directly analyze the surface energy of NMC, the NMC electrode shows the same tendency of electrochemical performance as the LCO electrode, suggesting that the NMC electrode shows a similar adhesion/cohesion tendency with LCO electrode). In addition, the colloidal gel (cathode slurry) formed by the attractive particles is not thermodynamically stable, but is a kinetically arrested state[88, 89]. Therefore, in the static state, the structure is relatively stable due to the attractive interaction between the particles. However, in the dynamic state (when flow is applied),

a new structural state can be formed in favor of phase separation [90].

The particle length scale of the bimodal suspension (active material and conductive material) can be estimated as the average diameter [91, 92]. This approach characterizes bimodal suspension containing two monodispersed particles as a pseudo-one component system with an average diameter $< D >$ (eq 4) with the same number density $(\rho_L + \rho_S)$ and total volume fraction.

$$< D >^3 (\rho_L + \rho_S) = \rho_L d_L^3 + \rho_S d_S^3, \qquad < D > = \left(\frac{R}{d_L^3} + \frac{1-R}{d_S^3}\right)^{-\frac{1}{3}} \tag{4}$$

where $< D >, R$, d_L, and d_S are the average diameter, mixing ratio, diameter of large particle, and diameter of small particle, respectively. We can calculate the Peclet number of the bimodal suspension from eq 5 using the average diameter calculated from eq 4 [91].

$$Pe = \frac{3\pi\eta_m \dot{\gamma} < D >^3}{4k_B T} \tag{5}$$

For the cathode slurries used in this study, it is found that Pe = 1.3 under the storage condition of the critical hydrodynamic stress $(\tau_c \sim 3\ Pa)$.

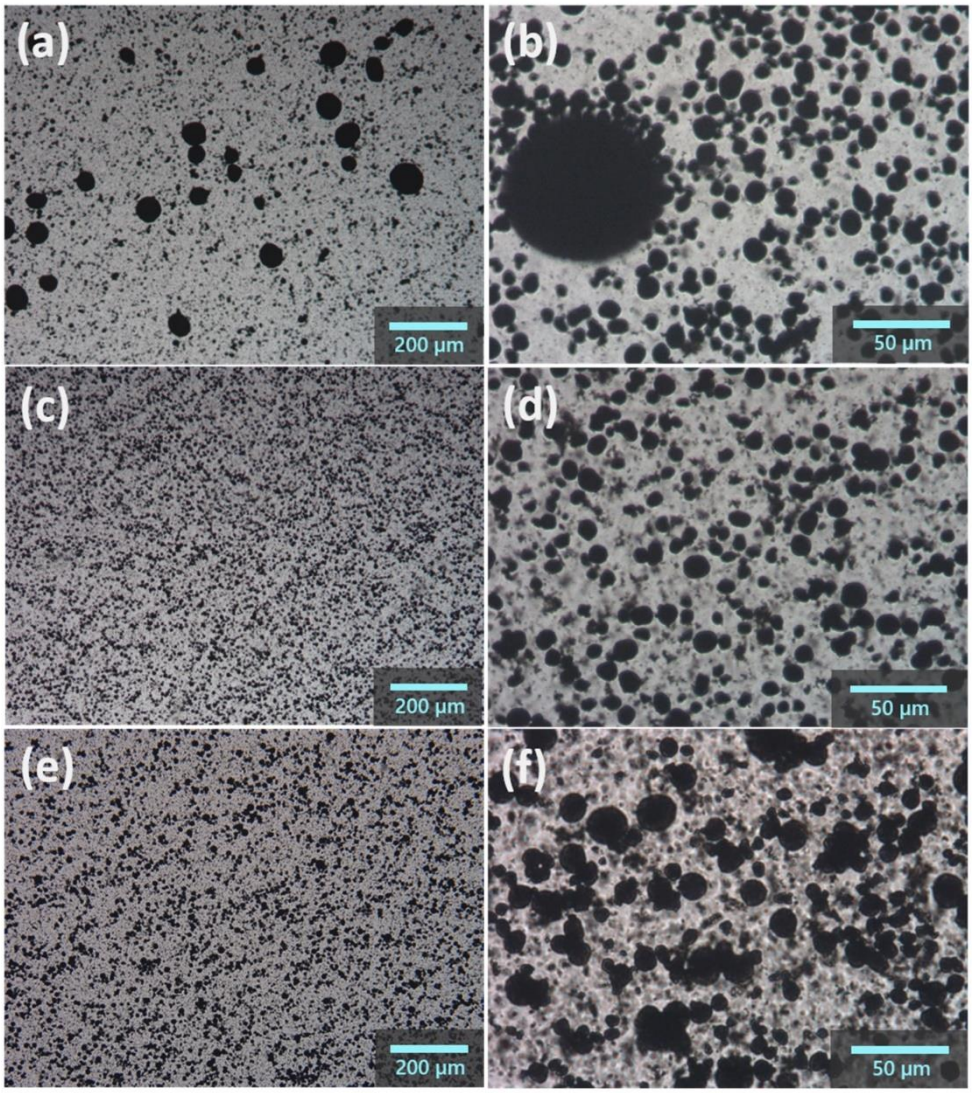

Figure 3.12. Optical micrographs of cathode slurries (NMC 4.2 vol%, AB 0.25 vol%) after 3 hours agitation at each stress conditions: (a) and (b) PVDF(700K) 0.42 wt%, 100 rpm $(\tau < \tau_c)$; (c) and (d) PVDF(700K) 0.58 wt%, 100 rpm $(\tau \sim \tau_c)$; (e) and (f) PVDF(320K) 0.83 wt%, 400 rpm $(\tau > \tau_c)$.

At storage conditions lower than the critical hydrodynamic stress $(\tau < \tau_c,\ Pe < 1)$, the thermal motion dominates over convective transport by flow. In other words, as the diffusion time scale of the particle is very short compared to the advection time scale, AB particles with higher surface affinity tend to agglomerate by themselves rather than agglomerate with the active materials (equilibrium behavior). Therefore, the AB particles are continuously agglomerated by the weak agitation to form large spherical agglomerates reaching several tens of μm (Figure 3.12a and b). As the volume-spanning network of NMC-AB branched agglomerates (Figure 3.4a and b) that exist before storage is destroyed and large AB spherical agglomerates are formed, the effective volume of AB particles rapidly decreases, resulting in a significant decrease in the elasticity of the cathode slurry where the cathode slurry shows a liquid-like behavior (Figure 3.11). However, when graphite particles, which have similar surface properties to AB particles, were used as the active material instead of NMC particles, no dramatic changes in rheological properties (Figure 3.13) and the formation of large spherical AB agglomerates (optical micrograph, Figure 3.14) were observed under same storage condition $(\tau < \tau_c)$ and slurry composition. It further suggests that the surface affinity between particles plays a major role in causing the change in slurry microstructure at $\tau < \tau_c$.

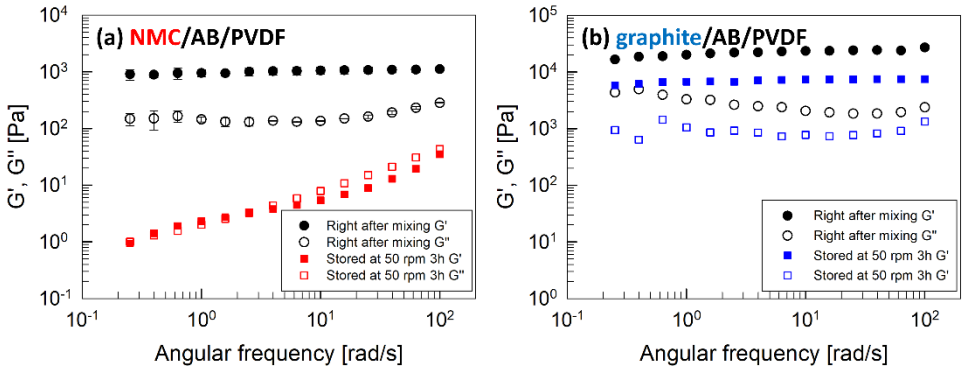

Figure 3.13. Changes in rheological properties of (a) NMC/AB/PVDF cathode slurry, and (b) graphite/AB/PVDF anode slurry after storage at 50 rpm for 3 hours.

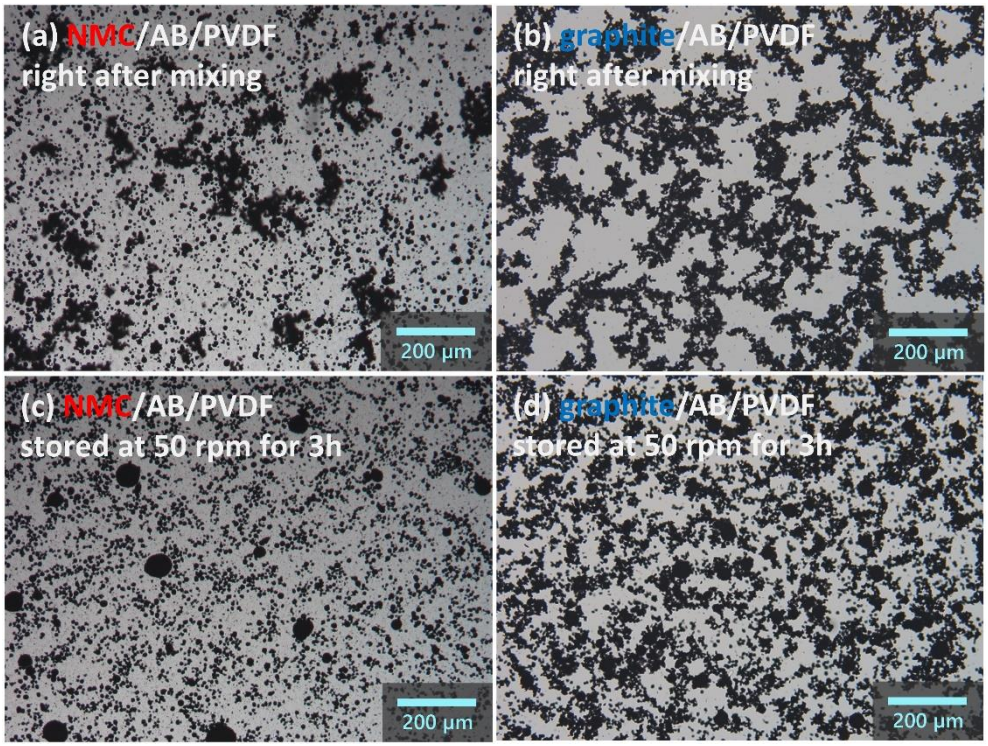

Figure 3.14. Changes in microstructure of (a) NMC/AB/PVDF cathode slurry, and (b) graphite/AB/PVDF anode slurry after storage at 50 rpm for 3 hours.

Under the storage conditions close to the critical hydrodynamic stress ($\tau \sim \tau_c$, $Pe \sim 1$), most of the AB particles are present in the medium in the form of sub-micron aggregates (Figure 3.12c and d). Under this storage conditions, the diffusive motion of the particles and convective transport oppose each other[93], and this state appears to be transient where AB particles cannot form large agglomerates by diffusive motion with other AB particles with high surface affinity (equilibrium behavior), nor can two particles (NMC,AB) with low surface affinity form agglomerates due to strong convective transport by flow (non-equilibrium behavior). Acetylene black (carbon black) exists in the form of aggregates with a size of 100-300 nm composed of primary particles, which can form larger secondary structures (agglomerates) by physical bonds (VDW attraction). And the smallest unit that can be dispersed by mechanical force is an aggregate with a size of hundred nanometers[75]. In this storage condition, the AB particles are dispersed into sub-micron aggregates by mechanical force caused by agitation and mainly exist in the medium. When AB particles exist as aggregates of sub-micron size, the elasticity of the cathode slurry shows an intermediate value (Figure 3.11) since it is disadvantageous for AB particles to form a volume-spanning network through the sample[29, 94]. This result is similar to Kuratani et al. that the elasticity of the slurry decreases when the conductive nanoparticles are over-dispersed by shear force[29].

Under the storage conditions of a stress sufficiently larger than the critical hydrodynamic stress ($\tau > \tau_c$, $Pe > 1$), the diffusive motion of the particles can be neglected since the convective transport in the flow direction is dominant. In this case, the non-equilibrium

phenomena where NMC and AB particles with relatively low surface affinity agglomerate together may occur due to the strong convective force by the flow[93]. In Figure 3.12e and f, NMC−AB agglomerates are distributed throughout the sample under this storage conditions. Since the hydrodynamic radius of the agglomerates in this state increases significantly compared to the aggregates in the transient state, the cathode slurry shows a larger G' value. Furthermore, as the hydrodynamic stress during storage further increases, the G' of the slurry saturates to the value it showed before storage, which is manufactured by strong hydrodynamic stress.

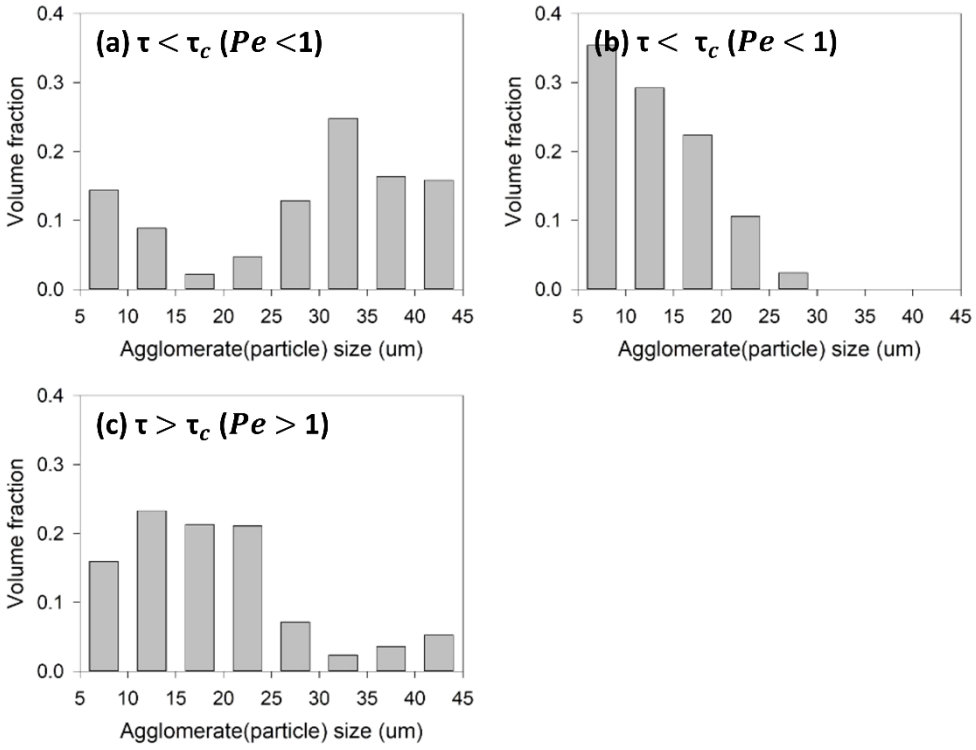

Figure 3.15. Agglomerate (particle) size distribution by image processing of optical microscopic images of cathode slurries: (a) from Figure 3.12a, (b) from Figure 3.12c, (c) from Figure 3.12e.

Figure 3.15 shows the agglomerate (particle) size distribution obtained by image processing of the OM images (Figure 3.12a,c, and e). For reliable analysis, more than 2,000 agglomerates (or particles) are analyzed. For larger than 5 μm, the average agglomerate(particle) sizes in Figure 3.12a,c, and e are calculated to be 9.4, 8.7, and 10 μm, respectively. However, the size distribution shows a large difference, indicating the difference in the microstructure of each slurry. Under the storage conditions of stress lower than the critical hydrodynamic stress (Figure 3.15a), a significant volume fraction of agglomerates larger than 25 μm is distributed as the AB particles form large spherical agglomerates along with the volume fraction of NMC particles with a size of 5 to 15 μm. At storage conditions close to the critical hydrodynamic stress (Figure 3.15b), the agglomerates with a size larger than 25 μm hardly exist anymore since most of the AB nanoparticles are distributed in the medium as sub-micron aggregates and do not form large agglomerates together with active materials. However, in the case of storage conditions of stress larger than the critical hydrodynamic stress (Figure 3.15c), more agglomerates with a size of several tens of μm exist than under the storage conditions of critical hydrodynamic stress, as AB nanoparticles form agglomerates together with NMC particles.

To summarize, under the storage conditions of a stress lower than the critical hydrodynamic stress, AB particles with relatively high surface affinity form large spherical agglomerates of several tens of μm by themselves. As a result, the elasticity of the cathode slurry sharply decreases, showing a liquid-like behavior. At the storage conditions close to the critical hydrodynamic stress, the AB

particles are dispersed in the form of sub-micron aggregates by the mechanical force caused by agitation, but do not form a new structure with active materials. Therefore, the cathode slurry shows a gel-like behavior with an intermediate G' value. As the hydrodynamic stress further increases, the NMC and AB particles with relatively low surface affinity form agglomerates by strong convective motion, and the cathode slurry exhibits a gel-like behavior with high elasticity.

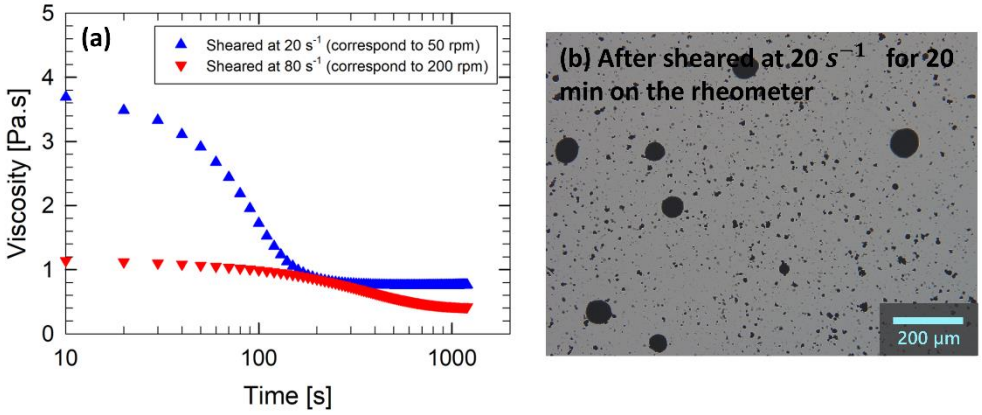

Figure 3.16. (a) Peak hold test results of cathode slurries (NMC 25 vol%, AB 1.5 vol%, PVDF (700K) 2.5 wt%) at $\dot{\gamma} = 20s^{-1}$ $(\tau = 0.8\,Pa)$ and $\dot{\gamma} = 80s^{-1}$ $(\tau = 3.2\,Pa)$ for 20 min (b) optical micrograph of cathode slurries (NMC 25 vol%, AB 1.5 vol%, PVDF 2.5 wt%) after peak hold test on the rheometer.

Figure 3.16 shows the peak hold test results of the cathode slurry (NMC 25 vol%, AB 1.5 vol%, PVDF (700K) 2.5 wt%) (Figure 3.16a) and the optical micrograph of that slurry observed by sampling after the peak hold test on the rheometer (Figure 3.16b). When the prepared cathode slurry is sheared at 20/s (equivalent to 50 rpm in storage tank, $\tau \sim 0.8\,Pa$) in a rheometer, the viscosity decreases

significantly with shearing time (Figure 3.16a). And observing the OM image of the slurry after shearing at 20/s for 20 min shows the formation of large spherical AB agglomerates (Figure 3.16b). However, when the slurry is sheared at 80/s (equivalent to 200 rpm in storage tank, $\tau \sim 3.2\,Pa$), although the viscosity decreases slightly with shearing, no large spherical AB agglomerates are formed. Therefore, we believe that the critical hydrodynamic shear stress (~ 3 Pa) presented in this study is estimated reasonably.

3.4. Conclusion

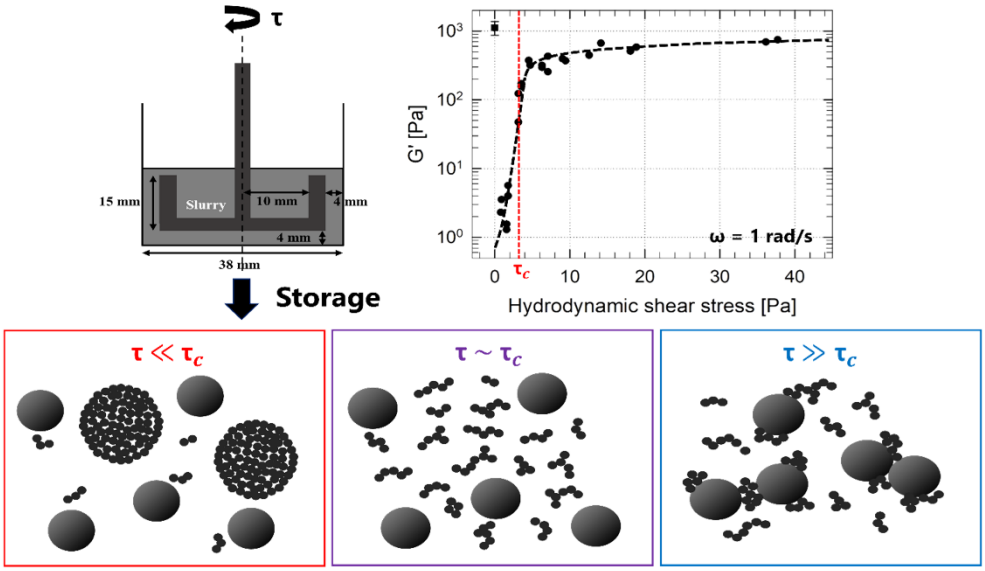

Figure 3.17. Schematic of the changes in rheological properties and microstructure of the cathode slurry during storage according to the hydrodynamic stress.

In this chapter, changes in slurry dispersion during storage were investigated through various storage conditions with varying agitation speed and systematically designed model cathode slurries with varying matrix viscosity. The slurry dispersion was mainly evaluated through rheological analysis and microstructure observation. Figure 3.17 summarizes the changes in rheological properties and microstructure of the slurry during storage according to the hydrodynamic stress induced by the flow.

The cathode slurry immediately after preparation (before storage) showed a gel-like behavior with strong elasticity as the NMC and AB particles form branch type agglomerates throughout the

sample. The changes in slurry dispersion significantly depend on storage conditions. In particular, the hydrodynamic stress, which is the product of matrix viscosity and agitation speed, mainly governed the changes in slurry dispersion. Under the storage conditions lower than the critical hydrodynamic stress, the diffusive motion of the particles dominates, and the AB particles with relatively higher surface affinity formed large spherical agglomerates with a size of several tens of μm. In this process, the effective volume of the AB particles decreased significantly, resulting in a sharp decrease in the elasticity of the cathode slurry, showing a liquid-like behavior. Under the storage conditions of a critical hydrodynamic stress or higher, although the G' slightly decreased, the cathode slurry showed a gel-like behavior as before storage. Under the storage conditions near the critical hydrodynamic stress, NMC and AB particles did not form new structures since the diffusive motion of particles and convective transport by flow are balanced with each other. Most of the AB particles were dispersed into sub-micron sized aggregates by mechanical force applied during agitation and were present in the medium. In this case, although the surface area per unit mass of the AB particles increased, the slurry showed intermediate elasticity as it was disadvantageous to form a volume-spanning network. Under the storage conditions higher than the critical hydrodynamic stress, NMC and AB particles with relatively low surface affinity formed agglomerates by the strong flow, so the cathode slurry exhibited a larger G' than other storage conditions.

The prepared electrode slurry is agitated in a storage tank to maintain dispersion quality prior to entering the subsequent coating process. Even if well-dispersed slurry is prepared, if the slurry

dispersion deteriorates during storage, it can lead to electrode defects like surface defects during the coating process, clogging of pipes and filters, and foil breakage during calendaring, thereby reducing the productivity of the electrode process. As disclosed in this chapter, if conductive particles significantly agglomerate, the productivity of the electrode might be significantly reduced. In particular, we observed that conductive particles form large spherical agglomerates even within a short storage time of several tens of minutes, which is much shorter than the actual storage time in the industrial electrode process, as shown in Figure 3.18. Furthermore, once formed, large spherical AB agglomerates remain in the cathode even after drying. Thus, it would be a very dangerous storage variable that can lead to electrode failure and reduce productivity in actual electrode processing. Therefore, we propose storing the slurry under storage conditions higher than the critical hydrodynamic stress.

The critical hydrodynamic stress presented in this study (3 Pa) will depend on the material-related parameters such as the surface properties of the particles and the composition of each component, and device parameters such as the design of the storage tank and agitator. However, our concept can be applied generally. This study will help improve the productivity of the electrodes by preventing electrode failure due to deterioration of the slurry dispersion during storage.

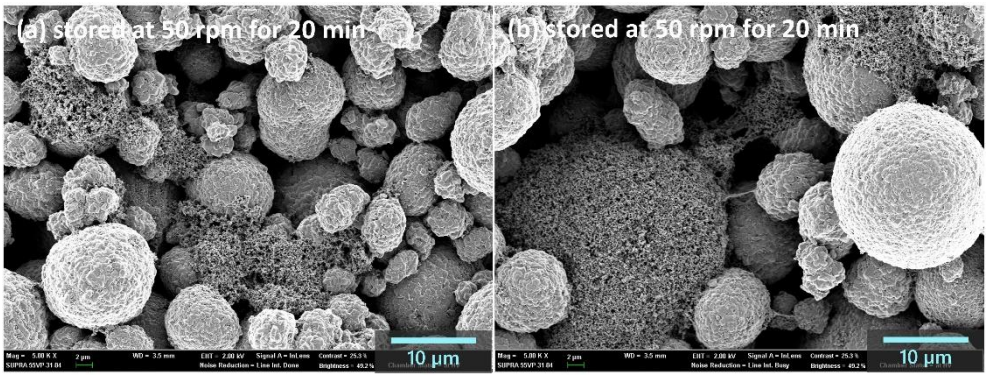

Figure 3.18. FE-SEM surface images of cathode (NMC 95.7 wt%, AB 2.7 wt%, PVDF 1.6 wt%) prepared from the cathode slurry stored at 50 rpm for 20 min. The process of AB particles forming a large spherical agglomerate was observed.

Chapter 4. Rheological behavior and microstructure formation of Si/CB anode slurries

4.1. Introduction

Silicon (Si) is in the limelight as a next-generation anode active materials for lithium-ion batteries (LIBs) owing to its high theoretical capacity (~4200 mAh/g) compared to conventional graphite materials (~370 mAh/g), eco-friendliness, and abundance in nature[95-97]. However, the utilization of silicon anode suffers from many difficulties owing to significant volume changes of Si (~300%, vs ~10% for graphite) during lithiation and delithiation[98-101]. The internal stress caused by the sudden volume change of Si leads to destruction of the network structure of electrode and formation of an unstable SEI (solid electrolyte) layer, resulting in a rapid capacity fading as well as poor cycle life[102-104].

Various approaches have been proposed to overcome these problems: (1) incorporation of functional electrolyte additives to form a stable SEI layer[105], (2) utilization of Si/C composites with a specific shape as an active material[106, 107], (3) Reduction of the size of Si particles to better withstand the internal stress[108], and (4) use of suitable binder capable of accommodating large volume changes[109]. Among them, approach (4) has recently attracting

attention as the most economical and efficient strategy as a solution to overcome the problem of large volume expansion of Si[109, 110].

Polymeric binders play a variety of roles as a component of electrodes: (1) adjustment of slurry dispersion[40, 41], (2) improvement of coating quality[111], (3) adhesive between substrate and electrode[112], and (4) formation of a stable SEI layer[113]. In particular, the binder has a great effect on the slurry dispersion by directly affecting the inter-particle interactions. To fully utilize the silicon anode, understanding the slurry dispersion of selected particle/binder system is as important as suppressing volume expansion of Si, as the electrode microstructure is directly related to the slurry dispersion formed during wet electrode processing[10-14].

Therefore, studies have been conducted to understand the dispersion state of Si anode slurry using various water-soluble binders such as guar gum (GG)[114, 115], sodium alginate (SA)[116, 117], PAA[118, 119], sodium carboxymethyl cellulose (CMC)/styrene butadiene rubber (SBR) blend[110, 118], and CMC[110, 116, 120, 121]. Among them, according to the recent studies, Si slurries show more uniform dispersion when prepared with CMC alone, and resulting anodes also show better electrochemical performance[110, 120, 121]. However, in Si slurry with CMC binder, an understanding of the interaction between each particle as well as the effect of CMC on the inter-particle interaction, and consequent slurry dispersion is still lacking.

In this study, we systemically investigate the rheological behavior and microstructure formation of Si anode slurries containing

Si active materials, CB conductive agent, and CMC binder from the viewpoint of interaction between each component, aiming to provide in-depth insight into the dispersion characteristics of the slurry. The results and discussion consist of three parts. In chapter 4.3.1, we investigate the CB-CB and Si-Si interaction as well as the effect of CMC on the interaction between each particle in the CB and Si suspensions, respectively. We observe that CMC adsorbs to both CB and Si particles but has different effects on the interaction between each particle; CMC acts as a dispersant for CB to stabilize the network structure, whereas acts as a flocculant for Si to form a network structure. Then, in chapter 4.3.2, based on the understanding of CB-CB and Si-Si interaction, we explore the Si-CB interaction by systematically varying the Si and CB content in the Si/CB suspension. It is found that the microstructure of the Si/CB suspension is mainly dominated by the CB particles, although Si particles have some influence on the structure at low CB content. Finally, in chapter 4.3.3, we explore the effect of CMC on the inter-particle interaction in the Si/CB/CMC anode slurry. It turns out that in Si/CB/CMC slurry, CMC acts as a dispersant below a certain CMC content, while it acts as a flocculant at higher content. It is attributed to the selective adsorption of CMC onto CB particles, rather than Si particles. The origin of selective adsorption is understood in terms of the driving forces for adsorption and the surface energy analysis.

4.2. Experimental section

4.2.1. Materials

Micron-sized silicon powder was used as an anode active material (US5008, US Research Nanomaterials, Inc., USA). According to the provider, the average particle size, density, and purity were 1 μm, 2.33 g/cm^3, and 99.9%, respectively. Conductive carbon black (Timcal Super C65, MTI Korea, Korea) was used as a conductive additive. According to the provider, the primary particle size was less than 50 nm, and the density and specific surface area were 2.25 g/cm^3 and 62 m^2/g, respectively. For polymeric binder, sodium carboxymethyl cellulose (CMC, Sigma-Aldrich, USA) was used. The degree of substitution (DS) and molecular weight (M_w) were 0.7 and 250,000 g/mol, respectively. Deionized water was used as a casting solvent for the preparation of each suspension and slurry.

4.2.2. Sample preparation

The CMC solution was prepared by adding a specific amount of CMC into deionized water and dissolving it for 8 hours at 500 rpm using an anchor-type mechanical stirrer. The Si and CB suspensions were prepared by adding each particle into the deionized water or pre-dissolved CMC solution and dispersing at 5,000 rpm for 10 minutes using a rotor-state homogenizer (Ultra-turrax T18, IKA, Germany) equipped with S18N-19G dispersing element. The Si/CB slurry was prepared by simultaneously adding Si and CB particles to the deionized water or CMC solution and dispersing at 5,000 rpm for 10 minutes using the same rotor-state homogenizer

used to prepare the Si and CB suspensions.

4.2.3. Rheological characterization

The rheological behavior of the CB and Si suspensions and CB/Si slurries were analyzed using a stress-controlled type rheometer (AR-G2, TA instruments, USA) equipped with 40 mm parallel plate fixture. For sample showing yielding behavior, a cross-hatched fixture was used with sandpaper to prevent wall slip effect. The gel-type sample was carefully loaded on the rheometer using a spoon to minimize the stress applied to the sample during loading, and the liquid-type sample was also carefully loaded using a pipette. The loading gap between the plate of the rheometer and each fixture was set between 800 and 1200 μm, which is an appropriate condition to characterize the rheological properties of the sample, depending on the loading conditions of the sample. After loading, each sample is rested for 1 min and then time-sweep test was performed in the linear viscoelastic (LVE) region for equilibration. After confirming that the viscoelasticity of the sample did not change significantly over time, a frequency sweep test was performed. Frequency sweep test was performed in an ascending-mode (0.25 to 100 rad/s) in a LVE region. The viscosity of the sample was measured through either descending-mode (1000 to 0.01 s^{-1}) or ascending-mode (0.01 to 1000 s^{-1}) shear rate sweep tests depending on the sample condition. In the case of samples showing gel-like or yielding behavior, when high shear is applied, the sample can jump out within the loading gap, so it was measured in ascending mode. On the other hand, samples exhibiting liquid-like behavior were measured in descending mode to prevent sedimentation.

4.2.4. Microstructure observation

The microstructure of the CB and Si suspensions and CB/Si slurries was observed using a polarizing microscope (BX51, Olympus, Japan) according to the following procedure. At first, each sample was diluted by 5 ~ 20 times with deionized water. If the dilution factor is too high, the number of particles become insufficient, making it difficult to observe the network structure of the particles. When the dilution factor is too low, the images become dark and obscure. Therefore, the dilution factor of each sample was selected as the most suitable for observing the network structure by gradually increasing the dilution factor and observing the images. After dilution, each sample was mixed for 20 seconds using a vortex mixer (VM-10, ALLforLAB, Korea). Then, about 0.1 ml of the sample was carefully loaded onto a slide glass (24 x 50 mm^2) using a dropper and covered with a cover glass (22 x 22 mm^2). Finally, the optical micrographs of the sample were obtained with 10 and 50 times magnification, respectively.

4.3. Results and discussion

4.3.1. CB/CMC and Si/CMC suspensions

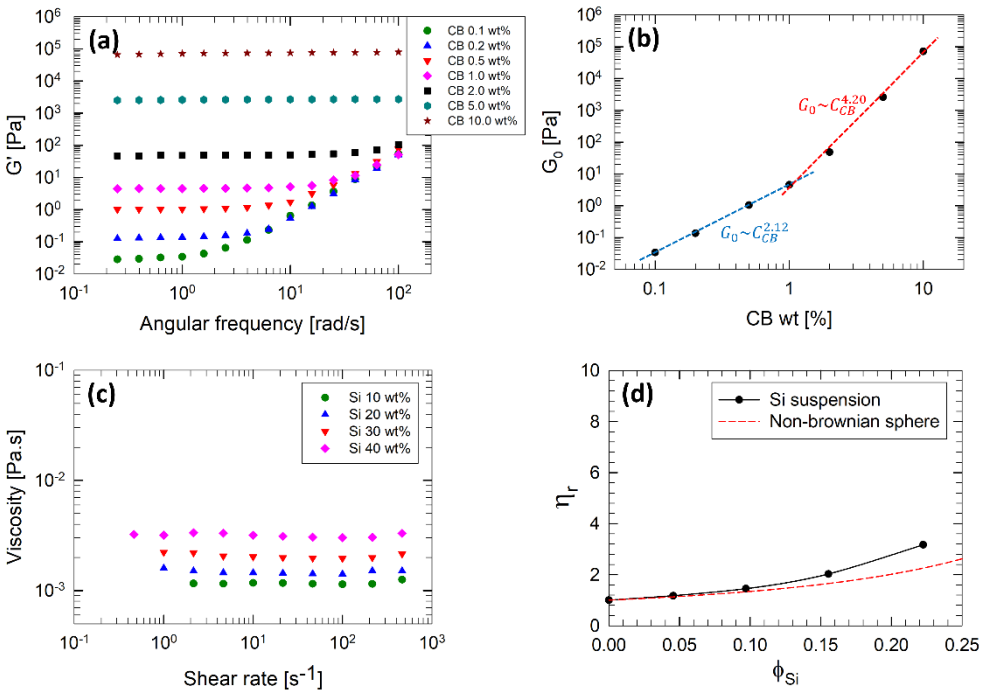

Figure 4.1. (a) frequency sweep results and (b) plateau modulus (at angular frequency = 1 rad/s) of CB suspension (CB/water) with varying CB content, and (c) steady sweep results and (d) relative viscosity of Si suspension (Si/water) with varying Si content.

Figure 4.1 shows the rheological properties of carbon black (CB) (Figure 4.1a and b) and silicon (Si) (Figure 4.1c and d) suspensions with increasing particle content (note that CMC is not present on each suspension). In all investigated CB content ranges (0.1 ~ 10 wt%), the CB suspension shows a solid-like characteristics in which G' is larger than G", and a plateau modulus (G_0) at low frequencies, suggesting a network structure of the CB particles. CB particles

with non-polar surfaces have a strong tendency to agglomerate by hydrophobic interactions, which contributes to the elasticity of the CB suspension[52]. As the CB content increases from 0.1 to 10 wt%, G' increases monotonically. However, the scaling exponent n ($G_0 \sim C_{CB}^n$) changes from 2.12 (below CB 1.0 wt%) to 4.20 (above CB 2.0 wt%). According to the percolation theory[122-125], $n \sim 2.1$ indicates the network structure of particles with bonds resisting stretching but free to rotate, and $n \sim 4.2$ suggests the 3D-percolation network structure of particles with bond-bending force that can bear stress by the unbending of their branches. Therefore, it can be known that the CB particles form a 3D-percolation network as the CB content increases to 2 wt% or more. The disappearance of the frequency dependence of G' at CB 2.0 wt% also suggests the formation of 3D-network structure.

The Si suspension exhibits a Newtonian behavior in which viscosity is independent of shear rate in the investigated high content range (10 ~ 40 wt%), and the viscosity increases monotonically with increasing Si content. In particular, the relative viscosity of the Si suspension with increasing Si content is similar to that of non-Brownian sphere ($\eta_r = e^{-2.34\Phi}\left(1-\frac{\Phi}{\Phi_{max}}\right)^{-3}$) proposed by Zarraga et al.[126], suggesting that Si particles do not form a network structure by particle-particle interactions even at high content. This is because in hydrophilic solvent, hydrophilic silanol groups (Si-OH), which are familiar with water, are formed on most Si surfaces, making the silicon particles familiar to the matrix (water).

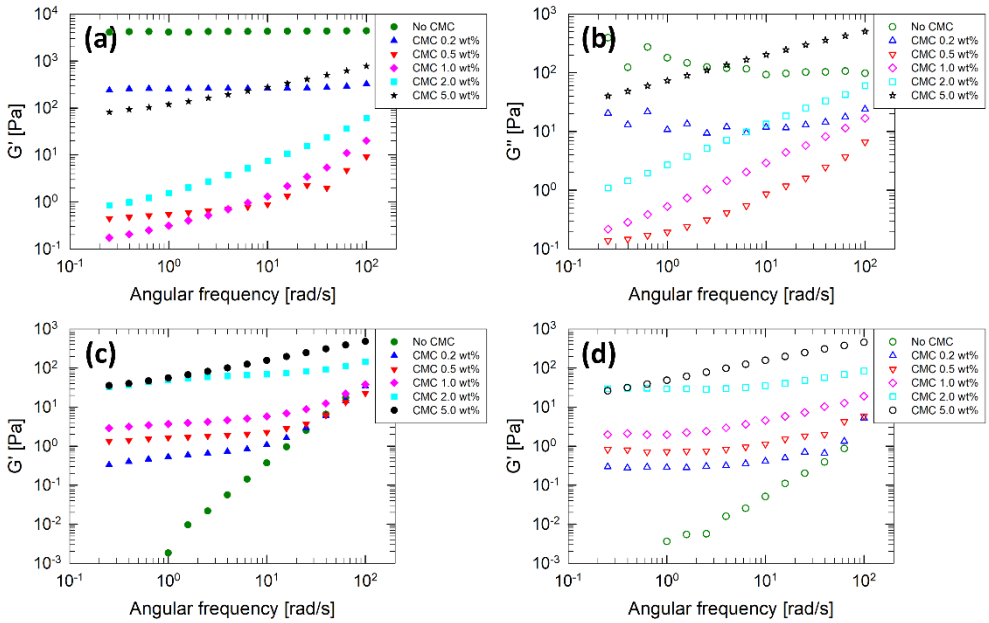

Figure 4.2. (a) storage modulus (G') and (b) loss modulus (G") of 5 wt% CB suspension with varying CMC content as a function of angular frequency, and (c) storage modulus (G') and (d) loss modulus (G") of 30 wt% Si suspension with varying CMC content as a function of angular frequency.

Figure 4.2 shows the frequency sweep results of CB suspension (Figure 4.2a and b) and Si suspension (Figure 4.3c and d) with increasing CMC content. Although CMC adsorbs to both CB and Si particles[27, 56, 110], it has different effect on the rheological properties of each suspension.

The CB suspension without CMC shows a gel-like behavior, suggesting the formation of a 3D-percolation network (hydrophobic interaction) of the CB particles. However, as the CMC content increases to 1.0 wt%, G' decreases significantly and G' and G" are reversed to show a liquid-like behavior, suggesting that the network structure is stabilized. Finally, as the CMC content increases to 5.0

wt%, the CB suspension shows a weak-gel behavior in which G' is larger than G" and has a weak frequency dependence, suggesting the formation of another network structure.

On the other hand, G' and G" of the Si suspension increases monotonically as the CMC content increases from 0 to 5 wt%. The increase in G' is larger when the CMC content increases from 0 to 0.2 wt%, and from 1.0 to 2.0 wt%. Further, unlike the CB suspension, the Si suspension does not show a plateau modulus as the CMC content increases from 0 to 2.0 wt%, suggesting that the rigid network structure is not formed by the particles. At CMC 5.0 wt%, the Si suspensions shows a weak-gel behavior, suggesting the formation of a network structure as in the CB suspension.

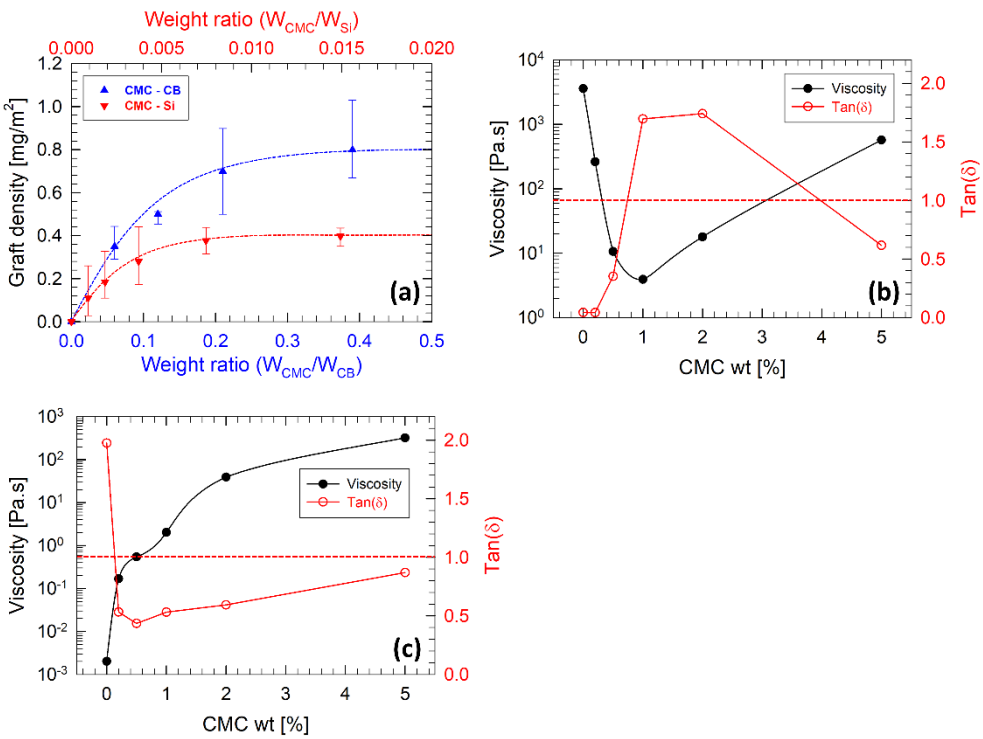

Figure 4.3. (a) adsorption isotherm of CMC-CB and CMC-Si. (b) Viscosity (shear rate = 0.1 s^{-1}, closed symbol, left) and tan(δ) =

G''/G' (frequency = 1 rad/s, open symbol, right) of (a) CB suspension and of (b) Si suspension with varying CMC content. The red dashed line represents the line with $\tan(\delta) = 1$.

Figure 4.3a shows the adsorption isotherms of CMC−CB and CMC−Si. Graft density refers the mass of polymer adsorbed on the unit surface area of the particle. The graft density increases as the mass ratio of CMC to particles increases, and adsorption is saturated at $W_{CMC}/W_{CB} \sim 0.2$ and $W_{CMC}/W_{Si} \sim 0.007$, respectively.

Figure 4.3b shows the change in viscosity and $\tan(\delta)$ of CB suspension. As CMC content increases, CB suspension shows a change in rheological properties from solid−like $(\tan(\delta) < 1,\ \text{gel-like behavior at CMC } 0 \sim 0.5\ \text{wt\%})$ to liquid−like $(\tan(\delta) > 1\ \text{ at CMC } 1.0 \sim 2.0\ \text{wt\%})$, and then back to solid−like behavior $(\tan(\delta) < 1, \text{weak-gel behavior at CMC } 5.0\ \text{wt\%})$. Changes in rheological properties from gel−like to liquid−like behavior appears at CMC 1.0 wt%. CMC 1.0 wt% is the content of the optimum graft density (~0.8 mg/m^2 for CMC−CB) where the viscosity becomes minimized with increasing CMC content. It suggests the optimal dispersion of the particles. Further, it is the content at which CB particles are adsorbed and saturated by CMC $(W_{CMC}/W_{CB} \sim 0.2\ at\ CMC\ 1.0\ wt\%)$. Therefore, as the CMC content increases to the optimum graft density (CMC 1.0 wt%), the CB particles that form the network structure through hydrophobic interaction is stabilized by the electro−steric interaction of the adsorbed CMC, resulting in a liquid−like behavior in the CB suspension. As CMC content increases above the optimum graft density, the CB suspension still shows a liquid−like behavior, but the viscosity increases. As discussed in chapter 2.3.1, free CMC remaining after adsorption increases the matrix viscosity, without

significantly affecting the network structure of the CB particles. At CMC 5.0 wt%, CB suspension shows a weak-gel behavior, which is the characteristics of the CMC-induced network structure (3D-fibrillar network induced by hydrophobic interactions between CMC chain), enhanced by the dispersed CB particles. In CB suspension, CMC acts as a dispersant (below the CMC content of the optimum graft density), thickener (above the CMC content of the optimum graft density), and gelling agent (above the gelling content of CMC solution, 4 wt% in this study) with increasing the content.

Figure 4.3c shows the change in viscosity and tan(δ) of Si suspension. Without CMC, Si suspension shows a liquid-like behavior ($\tan(\delta) > 1$), suggesting a uniform dispersion of particles. As CMC content increases to 0.2 wt%, Si suspension shows a solid-like behavior ($\tan(\delta) < 1$), suggesting an interaction between Si particles and CMC. The viscosity of the Si suspension tends to increase monotonically with increasing CMC content. The increase is larger when the CMC content increases from 0 to 0.2 wt%, and from 1.0 to 2.0 wt%. The rapid increase in G' (Figure 4.2c) and viscosity (Figure 4.3c) at CMC 0.2 and 2.0 wt% suggests the formation of the agglomerates (or aggregates) or network structure of the Si particles by the adsorbed CMC. At CMC 5.0 wt%, Si suspension shows a weak-gel behavior, suggesting the presence of CMC-induced network structure (3D-fibrillar network) enhanced by the Si particles, as in the CB suspension.

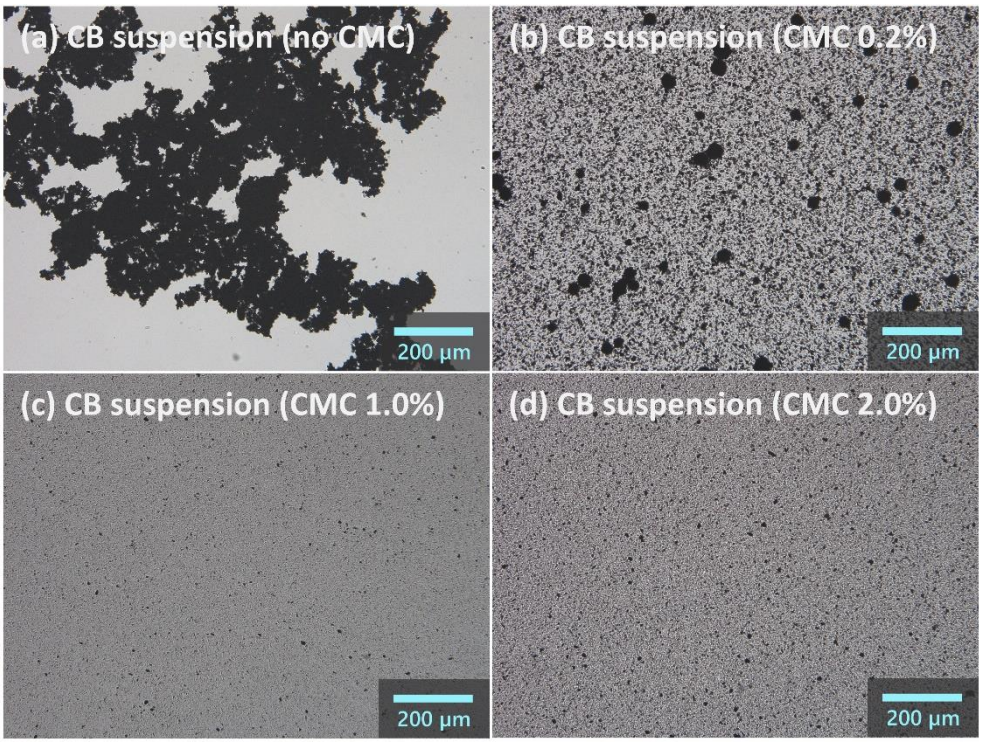

Figure 4.4. Optical micrographs of 5 wt% CB suspensions with (a) no CMC, (b) CMC 0.2 wt% (below optimum graft density), (c) CMC 1.0 wt% (near optimum graft density), and (d) CMC 2.0 wt% (above optimum graft density). The CB suspension was diluted 10 times with DI water.

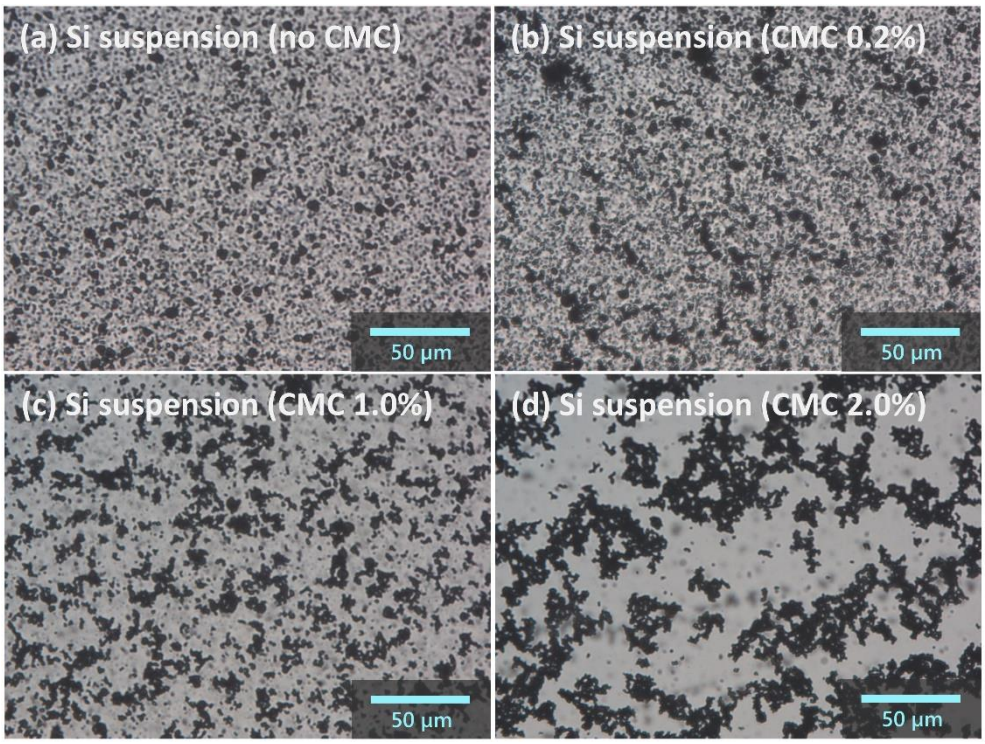

Figure 4.5. Optical micrographs of 30 wt% Si suspension with (a) no CMC, (b) CMC 0.2 wt%, (c) CMC 1.0 wt%, and (f) CMC 2.0 wt%. The Si suspension was diluted 10 times with DI water.

Figure 4.4 shows the optical micrographs of the CB suspension with increasing CMC content. In the absence of CMC (Figure 4.4a), CB particles form a volume-spanning percolation network structure by hydrophobic interactions. At CMC content lower than the optimum graft density (CMC 0.2 wt%, Figure 4.4b), some CB particles are dispersed by the adsorbed CMC, but CB agglomerates with a size of several tens of μm formed by hydrophobic interactions between the CB particles are still observed. However, at CMC content similar to (CMC 1.0 wt%, Figure 4.4c) or higher (CMC 2.0 wt%, Figure 4.4d) than the optimum graft density, most of the CB particles are uniformly dispersed by the electro-steric interaction of the adsorbed CMC.

Figure 4.5 shows the optical micrographs of the Si suspension with increasing CMC content. Without CMC (Figure 4.5a), most of the silicon particles (~ 1 μm) are uniformly dispersed without significant agglomeration, suggesting that the interaction between Si particles is negligible in terms of the formation of the network structure. At CMC 0.2 wt% (Figure 4.5b), Si particles form agglomerates by the adsorbed CMC. This is indicated by the rapid increase in G' and viscosity at CMC 0.2 wt% (Figure 4.2 and 4.3). At CMC 1.0 wt% (Figure 4.5c), more and larger Si agglomerates are formed. At CMC 2.0 wt% (Figure 4.5d), the formation of volume-spanning network structure is observed. This is also indicated by the rapid increase in G' and viscosity at CMC 2.0 wt% (Figure 4.2 and Figure 4.3). From rheological behavior and microstructure observation, it can be known that CMC adsorbs on Si particles and acts as a flocculant through bridging interactions.

However, the network structure of CB (Figure 4.4a) and Si particles (Figure 4.5d) should be distinguished from each other. CB particles form a network structure through strong hydrophobic interactions between particles. When the structure is formed, the CB suspension shows frequency-independent gel-like behavior and scaling exponent $n \sim 4.2$ (Figure 4.1 and Figure 4.2), suggesting a 3D-percolation network structure that can bear stress without being destroyed. However, Si particles form a network structure through weak hydrogen bonding by adsorbed CMC. Even when the network structure is formed, the Si suspension shows a strong frequency-dependence of G' without plateau modulus (Figure 4.2), indicating a weaker (fragile) network structure than that of CB. The change of each suspension with increasing CMC content is clearly observed

with naked eye (Figure 4.6).

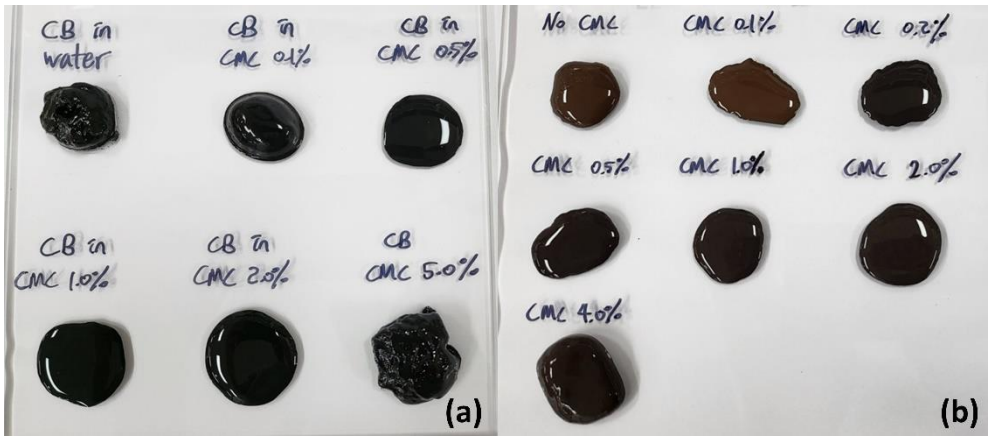

Figure 4.6. Images of the (a) 5 wt% CB suspension, and (b) 30 wt% Si suspension with varying CMC content.

4.3.2. Si/CB suspension

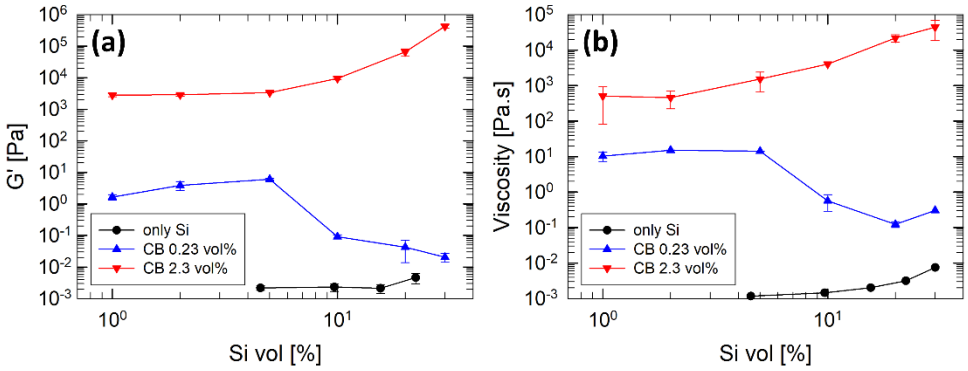

Figure 4.7. (a) Storage modulus (frequency = 1 rad/s), and (b) viscosity (shear rate = 0.1 s^{-1}) of Si and Si/CB suspensions with varying Si content.

Figure 4.7 shows the change in storage modulus (G') (Figure 4.7a) and viscosity (Figure 4.7b) of Si/CB suspension at each CB

content with increasing Si content (note that CMC is not present on each suspension). To better characterize the bimodal suspensions containing two particles (Si/CB), the content of each particle is given as volume % from chapter 4.3.2. As CMC content increases, Si suspension (only Si) shows a negligible change in G' and a monotonic increase in viscosity (showing a Newtonian behavior), suggesting that no network structure is formed by the Si particles. As the CB content increases to 0.23 and 2.3 vol%, G' and viscosity increases significantly. However, changes in the rheological properties of the Si/CB suspension with increasing Si content is different depending on the CB content.

First, at CB 0.23 vol% (corresponds to 0.5 wt% where CB particles do not form a 3D-percolation network structure with scaling exponent $n \sim 2.12$, Figure 4.1b), as Si content increases from 1 to 5 vol%, the Si/CB suspensions show similar G' and viscosity, suggesting that Si particles do not significantly affect the network structure of the CB particles. As Si content increases above 10 vol% (corresponds to 20 wt%), G' and viscosity of the Si/CB suspension decrease rapidly with increasing Si content, suggesting the breakup of the network structure. At CB 2.3 vol% (corresponds to 5.0 wt% where CB particles form a 3D-percolation network with scaling exponent $n \sim 4.3$, Figure 4.1b), the Si/CB suspensions show similar G', suggesting a negligible effect of Si on the CB network structure. However, as Si content increases above 10 vol%, G' and viscosity of the Si/CB suspension increase monotonically, suggesting that Si particles reinforce the network structure of CB particles.

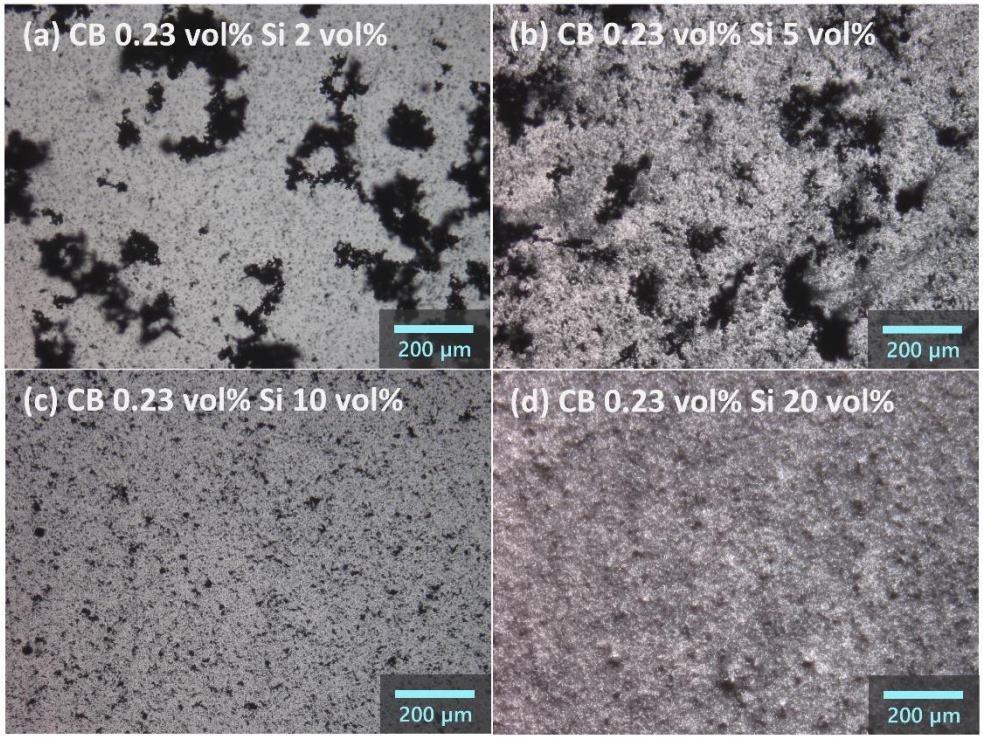

Figure 4.8. Optical micrographs of Si/CB suspension containing (a) CB 0.23 vol%/Si 2 vol%, (b) CB 0.23 vol%/Si 5 vol%, (c) CB 0.23 vol%/Si 10 vol%, and (d) CB 0.23 vol%/Si 20 vol%. The Si/CB suspension was diluted 5 ~ 10 times with DI water.

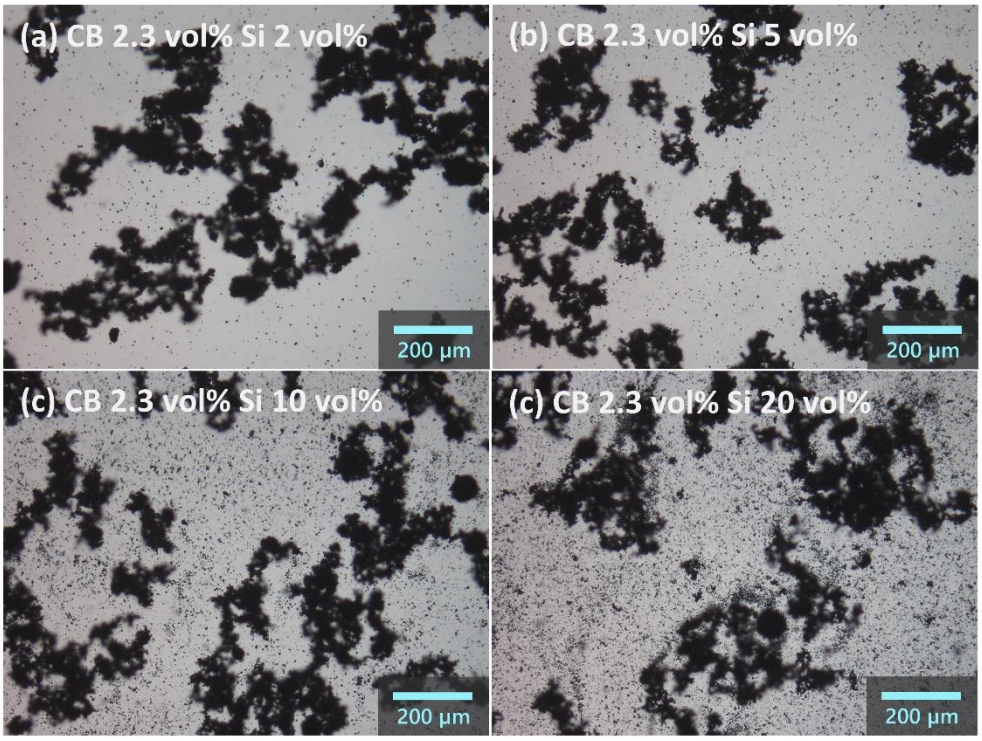

Figure 4.9. Optical micrographs of Si/CB suspension containing (a) CB 2.3 vol%/Si 2 vol%, (b) CB 2.3 vol%/Si 5 vol%, (c) CB 2.3 vol%/Si 10 vol%, and (d) CB 2.3 vol%/Si 20 vol%. The Si/CB suspension was diluted 10 ~ 20 times with DI water.

Figure 4.8 shows the optical micrographs of the Si/CB suspension containing CB 0.23 vol% with increasing Si content. At Si 2 (Figure 4.8a) and 5 (Figure 4.8b) vol%, the network structure of CB particles (by hydrophobic interaction) is observed as in the CB suspension (Figure 4.4a). However, at Si 10 vol% (Figure 4.8c), most of the network structure of the CB particles is destroyed and the CB agglomerates become smaller, and at Si 20 vol% (Figure 4.8d), there is almost no network structure, and the number and size of agglomerates are further reduced. Therefore, it can be inferred that at high Si content (above 10 vol%), large Si particles exert significant stress to disrupt the network structure of the CB particles during the

mixing and dispersing step, resulting in a decrease in G' and viscosity of the Si/CB suspension (Figure 4.7).

Figure 4.9 shows the optical micrographs of the Si/CB suspension containing CB 2.3 vol% with increasing Si content. Unlike at CB 0.23 vol% (Figure 4.8), the network structure of CB is present for all Si content (2 ~ 20 vol%). Therefore, it can be inferred that when CB particles from a 3D-percolation network (indicated by $n \sim 4.2$, compared to $n \sim 2.12$ at CB 0.23 vol%), Si particles do not disrupt the CB network structure at high Si content. Instead, they participate and reinforce it, as indicated by an increase in G' and viscosity of the Si/CB suspension.

From Figure 4.7, Figure 4.8, and Figure 4.9, it can be known that CB mainly governs the rheological behavior and microstructure formation of the Si/CB suspension. The change is determined by the CB content. At CB 0.23 vol% ($n \sim 2.12$ in the CB suspension), Si particles easily disrupt the CB network structure at high content (above 10 vol%). However, at CB 2.3 vol% ($n \sim 4.2$ in the CB suspension), Si particle hardly disturb the CB network structure even at high content (20 vol%), but rather strengthened it. The results are consistent with the percolation theory that at scaling exponent $n \sim 4.3$, the particles form a 3D-percolation network structure capable of withstanding the stress[122-125].

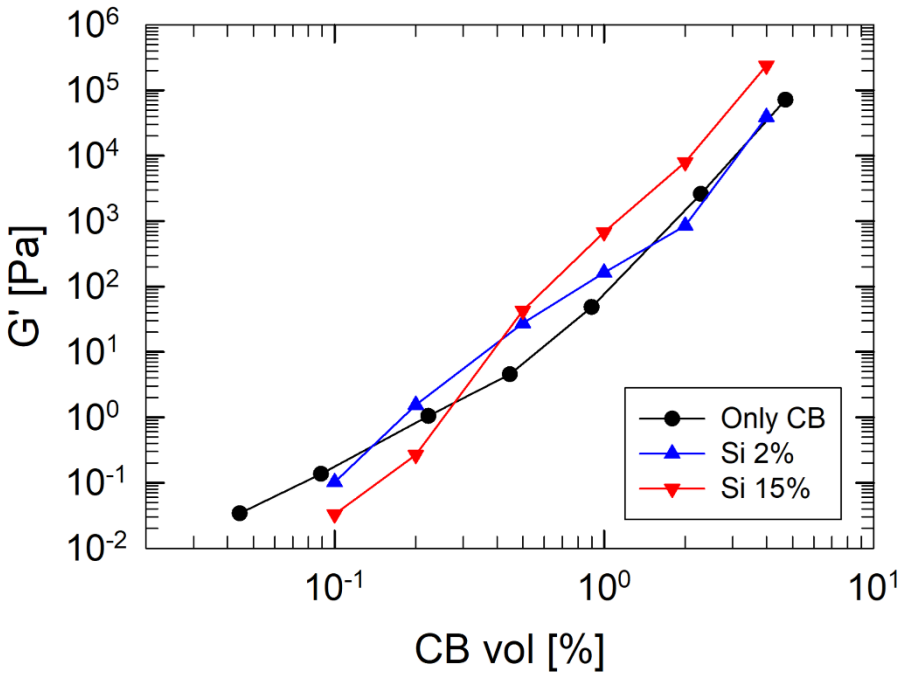

Figure 4.10. (a) Storage modulus (frequency = 1 rad/s), and (b) viscosity (shear rate = 0.1 s^{-1}) of CB and Si/CB suspensions with varying CB content.

Figure 4.10 shows the change in storage modulus (G') of Si/CB suspension at each Si content with increasing CB content (note that CMC is not present on each suspension). As Si particles do not significantly affect the network structure of CB at low Si content, the G' of the Si/CB suspension (Si 2 vol%) with increasing the CB content is similar to that of the CB suspension (only CB). On the other hand, at Si content higher than 10 vol%, Si particles disrupt or reinforce the CB network structure based on the CB content where scaling exponent n changes from 2.12 to 4.3 (at about 0.5 ~ 1.0 vol%). Therefore, the G' of the Si/CB suspension changes more rapidly with increasing the CB content at Si 15 vol% than in the absence of Si (only CB) or at Si 2 vol%. Not only the effect of Si particles on the

CB network structure is determined by the characteristics of the CB network structure, the gelation of Si/CB suspension is determined by the CB content (0.5 vol%) regardless of the Si content. Therefore, it can be known that the rheological behavior and microstructure formation of Si/CB suspensions are mainly dominated by CB particles.

4.3.3. Si/CB/CMC anode slurry

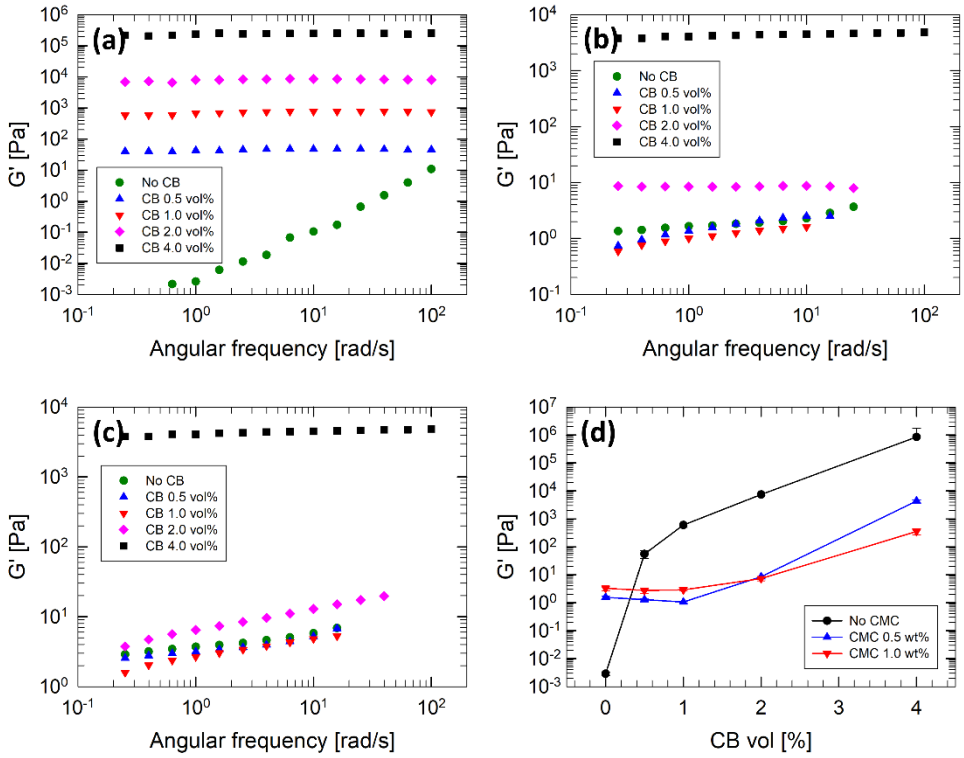

Figure 4.11. Storage modulus of Si/CB/CMC anode slurry containing Si 15 vol% with (a) no CMC, (b) CMC 0.5 wt%, (c) CMC 1.0 wt% with varying CB content. (d) Storage modulus (at frequency = 1 rad/s) of Si/CB/CMC suspension with increasing CB content at each CMC content.

Figure 4.11 shows the change in storage modulus (G') of the Si (15 vol%)/CB/CMC anode slurry at each CMC content with increasing

CB content. Note that Si content is same (15 vol%) for all slurries. In the absence of CMC (Figure 4.11a), the G' of the slurry without CB shows a strong frequency dependence, suggesting the absence of a network structure. As the CB content increases to 0.5 vol% (correspond to about 1.0 wt%), the slurry shows a frequency-independent gel-like behavior, which is the characteristic of the 3D-percolation network structure of CB particles. As the CB content further increases to 4.0 vol%, G' increases monotonically, showing a gel-like behavior. However, in the presence of CMC, the change in G' of the slurry with increasing CB content is different from that in the absence of CMC.

At CMC 0.5 wt% (Figure 4.11b), as the CB content increases from 0 to 1.0 vol%, the G' of the slurry is similar in the investigated frequency ranges and the plateau modulus is not observed, suggesting the absence of a network structure. However, as the CB content increases to 2.0 vol%, G' starts to increase and the slurry shows a gel-like behavior, suggesting a formation of the CB network structure. As the CB content further increases to 4.0 vol%, G' increases significantly, showing a gel-like behavior. On the other and, at CMC 1.0 wt% (Figure 4.11c), the slurry shows a similar G' without a plateau modulus at CB content from 0 to 2.0 vol, and a sharp increase in G' at CB 4.0 vol%, showing a gel-like behavior.

In Figure 4.11d summarizes the results of Figure 4.11a, b, and c. Without CMC, the G' of the slurry increases monotonically with increasing CB content. In the presence of CMC, as the CB content increases, the G' of the slurry shows a similar value at low CB content but increases significantly above a certain content. In particular, the CB content at which G' starts to increase and shows a gel-like

behavior decreases as the CMC content increases.

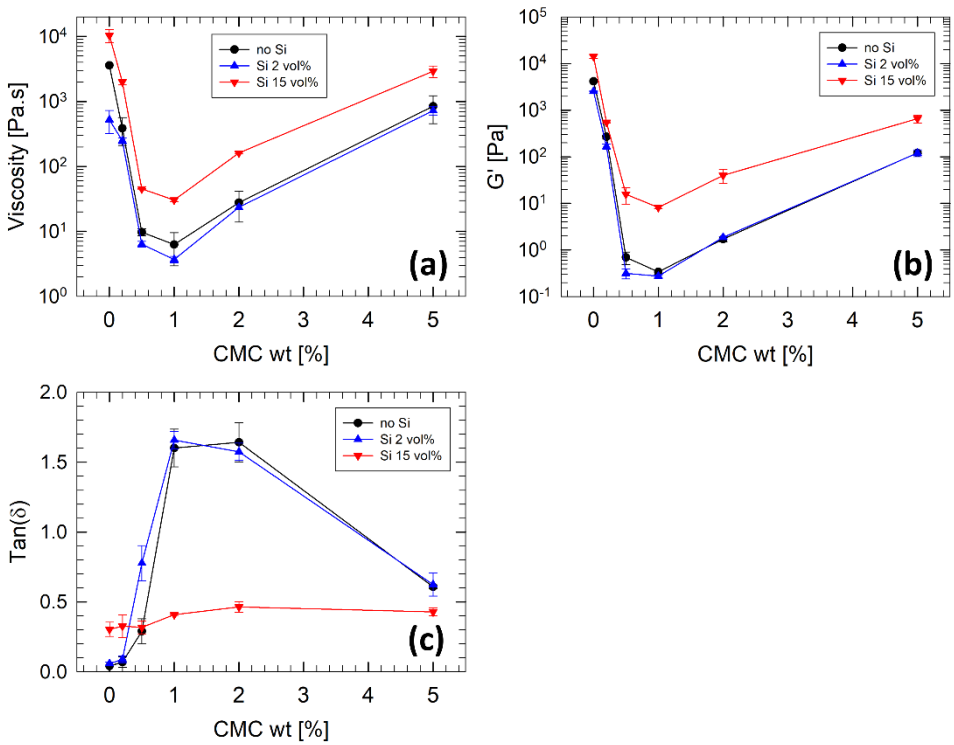

Figure 4.12. Rheological properties of Si/CB/CMC anode slurries containing Si 0/2/15 vol% and CB 2.3 vol% with varying CMC content: (a) viscosity (shear rate = 0.1 s^{-1}), (b) storage modulus (frequency = 1 rad/s), and (c) tan(δ).

Figure 4.12 shows the change in viscosity (Figure 4.12a), storage modulus (Figure 4.12b), and tan(δ) (Figure 4.12c) of the Si/CB(2.3 vol%)/CMC anode slurry at each Si content with increasing CMC content. Note that CB content is same (2.3 vol%) for all slurries. At Si 2 vol%, as the CMC content increases, the viscosity and G' of the slurries decrease below CMC 1.0 wt% and then increase above CMC 1.0 wt%, showing values similar to those of the CB suspension (no Si) at each CMC content. Tan(δ) also shows similar trend to that of CB suspension. At Si 15 vol%, the viscosity and G'

of the slurry are larger than those of CB suspension or Si(2 vol%)/CB slurry at each CMC content, but still decrease and then increase with increasing CMC content.

In particular, it should be noted that as CMC content increases, the viscosity of the slurries becomes minimized at CMC 1.0 wt% regardless of Si content, suggesting an optimum dispersion of the particles. Surprisingly, as discussed in chapter 4.3.1, it is the content close the content of the optimum graft density for CB particles ($W_{CMC}/W_{CB} \sim 0.2$) where CB particles are adsorbed and saturated by CMC. Therefore, it can be confirmed that CMC selectively adsorbs and disperses CB particles and acts as a dispersant in the slurries at a content lower than the optimum graft density for the CB particles (the detailed rationale for selective adsorption will be discussed later). Also, in Figure 4.11, it is confirmed that the CB content where the G' rapidly increases and the slurry starts to show a gel-like behavior in each slurry is the content where CMC content becomes lower than the optimum graft density for CB particles. Therefore, in Figure 4.12, as the CMC content increases to 1.0 wt%, viscosity and G' of the slurries decrease significantly to a minimum value, as the network structure of the particles is stabilized by the adsorbed CMC.

The selective adsorption of CMC to CB can be explained by the two theoretical rationales. One thing is the difference in the adsorption mechanism of CMC for each particle. The driving force for the adsorption of CMC to CB is the hydrophobic interaction between the hydrophobic chain of CMC and the non-polar surface of CB particles[27, 109], and that for the adsorption of CMC to Si is the hydrogen-bonding between hydrophilic functional groups (hydroxyl

and carboxylate groups) of CMC and silanol groups formed on the Si surface[56, 116]. In general, hydrophobic interaction is relatively stronger than other intermolecular forces (van der Waals interactions or hydrogen bonds), although the strength depends on the specific polymers and particles involved[127-129]. Further, in hydrophilic environment (water), hydrogen bonding between the two species can be weakened due to the presence of water molecules, which also can form hydrogen bonds with the hydrogen-bonding species. Therefore, the driving force for the adsorption of CMC to Si can be weakened.

The other thing is the difference in surface affinity between CB-CMC and Si-CMC. By using the Fowkes equation[87] (same as eq 3 in chapter 3.3.4), we can calculate the work of adhesion (W_{ij}) which characterizes the affinity between two species:

$$W_{ij} = 2(\gamma_i^d \gamma_j^d)^{0.5} + 2(\gamma_i^p \gamma_j^p)^{0.5} \quad (3)$$

where γ_i^d and γ_j^d are the dispersive surface energy of materials i and j, γ_i^p and γ_j^p are the polar surface energy of materials i and j, respectively. Calculating from the polar and dispersive surface energy of each component in the literature, W_{CMC-CB} is about 82.6 mN/m and the W_{CMC-Si} is about 64.4 mN/m. Therefore, from the thermodynamic point of view, it can be known that CMC-CB adsorption is more advantageous than CMC-Si adsorption.

At CMC content above the optimum graft density of the CB particles (1 wt%), the viscosity and G' of the slurries (no Si/Si 2 vol%/Si 15 vol%) increase as the CMC content increases to 2 wt%. This is because the excess CMC remaining after adsorption on CB particles adsorbs on the Si particles and acts as a flocculant in the

slurries to form a network structure of the particles (as will be discussed later). However, at Si 2 vol%, slurry shows similar viscosity and G' to CB suspension and shows a liquid-like behavior ($\tan(\delta)>1$), unlike at Si 15 vol%, which shows a solid-like behavior ($\tan(\delta)<1$). It has been found that CMC cannot act as a flocculant for the particles if the Si content is insufficient, as discussed later. As the CMC content further increases to 5 wt%, the slurries (no Si/Si 2 vol%/Si 15 vol%) show a weak-gel behavior, which is a characteristic of the fibrillar network structure of the CMC enhanced by the particles. As in the CB and Si suspensions, CMC acts as a gelling agent above the CMC content where it forms a 3D-fibrillar network in the matrix.

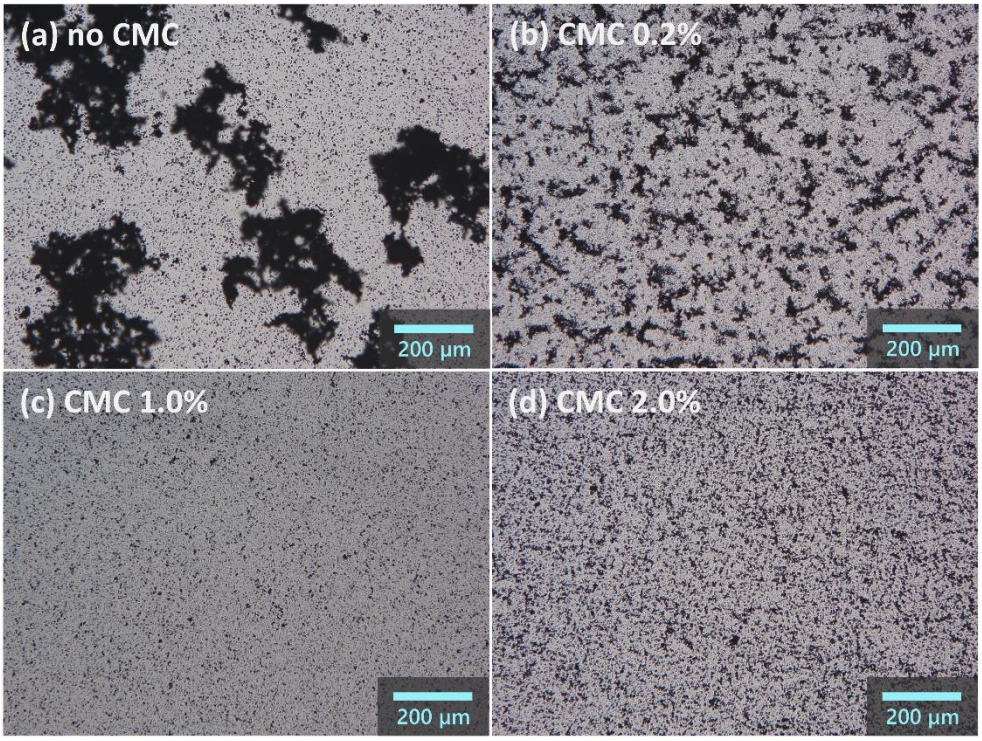

Figure 4.13. Optical micrographs of Si/CB/CMC anode slurry containing Si 15 vol% and CB 2.3 vol% with increasing CMC content: (a) no CMC, (b) CMC 0.2 wt%, (c) CMC 1.0 wt%, and (d) CMC 2.0

wt%. The Si/CB suspension was diluted 20 times with DI water.

Figure 4.13 shows the optical micrographs of the Si(15 vol%)/CB(2.3 vol%)/CMC anode slurries with increasing CMC content. In the absence of CMC (Figure 4.13a), CB particles agglomerate to form a volume-spanning network structure together with Si particles. At CMC 0.2 wt% (Figure 4.13b, below the CMC content of optimum graft density for CB particles), the network structure of the particles is more stabilized and agglomerates become smaller than without CMC, as CMC adsorbs to CB particles and acts as a dispersant. At CMC 1.0 wt% (Figure 4.13c, close the CMC content of optimum graft density for CB particles), the network structure is the most stable as most of the CB particles are dispersed by the adsorbed CMC. At CMC 2.0 wt% (Figure 4.13d, above the CMC content of optimum graft density for CB particles), agglomerates of the particles are observed again as CMC adsorbs to Si particles and acts as a flocculant.

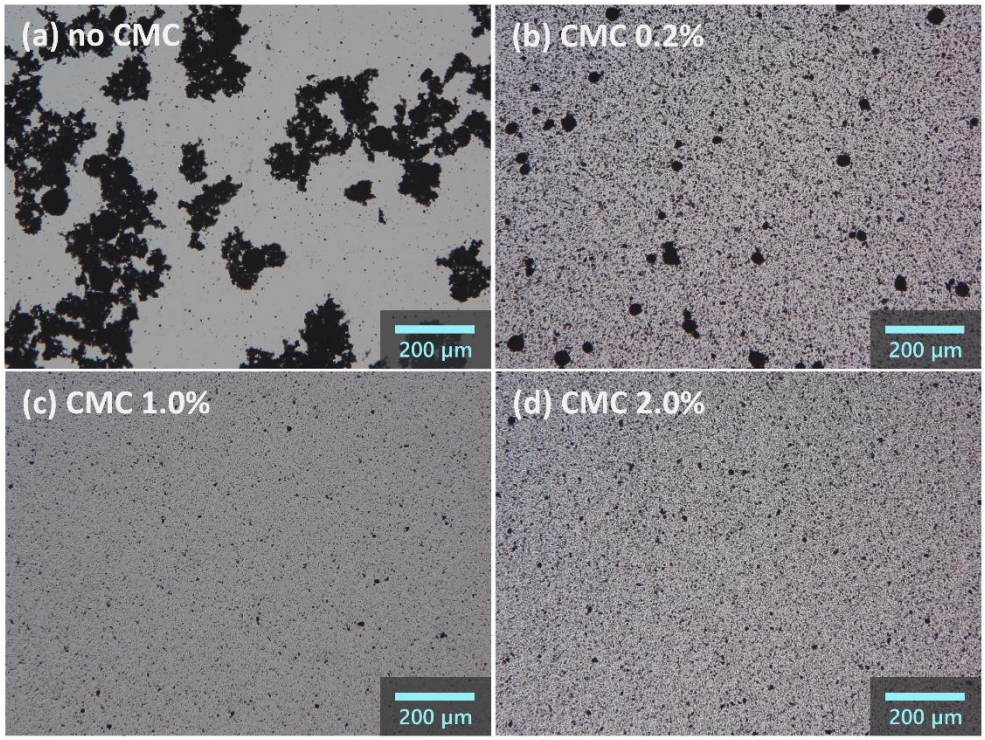

Figure 4.14. Optical micrographs of Si/CB/CMC anode slurry containing Si 2 vol% and CB 2.3 vol% with increasing CMC content: (a) no CMC, (b) CMC 0.2 wt%, (c) CMC 1.0 wt%, and (d) CMC 2.0 wt%. The Si/CB suspension was diluted 10 times with DI water.

Figure 4.14 shows the optical micrographs of the Si(2 vol%)/CB(2.3 vol%)/CMC anode slurries with increasing CMC content. As in the slurry of Si 15 vol% (Figure 4.13), the network structure of CB particles is observed in the absence of CMC (Figure 4.14a), and it is weakened at CMC 0.2 wt% (Figure 4.14b). At CMC 1.0 wt% (close the CMC content of optimum graft density for CB particles), most of the CB particles are dispersed by the adsorbed CMC. At CMC 2.0 wt% (Figure 4.14d), agglomerates of the particles are not frequently observed, unlike at Si 15 vol% (Figure 4.13d), as the Si content is insufficient for CMC to act as a flocculant through bridging interactions.

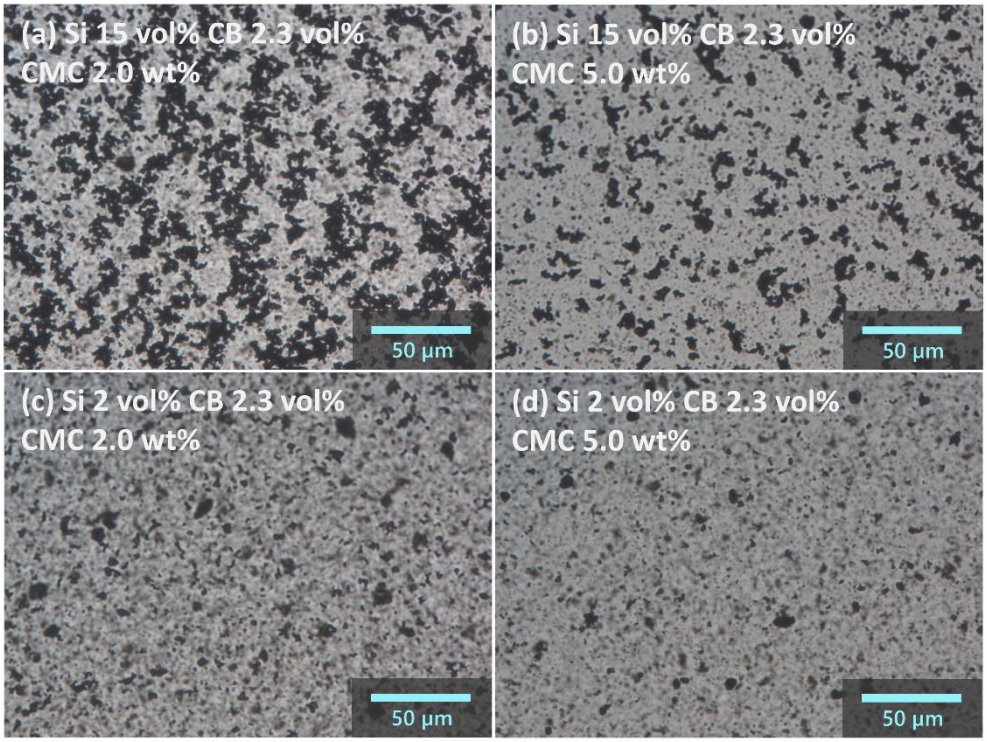

Figure 4.15. Optical micrographs of Si/CB/CMC anode slurry containing Si 15 vol% and CB 2.3 vol% with (a) CMC 2.0 wt%, (b) CMC 5.0 wt%, (c) CMC 2.0 wt%, and (d) CMC 5.0 wt%. The Si/CB suspension was diluted 10 ~ 20 times with DI water.

Figure 4.15 shows the optical micrographs of the Si(15/2vol%)/CB(2.3 vol%)/CMC anode slurries containing CMC 2.0 wt% and 5.0 wt%, respectively. At Si 15 vol% (Figure 4.15a and b), Si−CMC−CB agglomerates are observed, as CMC acts as a flocculant above CMC content of the optimum graft density for CB particles. On the other hand, at Si 2 vol% (Figure 4.15c and d), Si−CMC−CB agglomerates are not present, even though the CMC content is higher than the optimum graft density for CB particles. Therefore, it can be inferred that the Si content should be sufficient for CMC to act as a flocculant, as discussed in Figure 4.12. The reason why the number and size of Si−CMC−CB agglomerates are reduced at CMC

5.0 wt% compared to CMC 2.0 wt% in Si(15 vol%)/CB(2.3 vol%)/CMC slurry is that most of the CMC acts as a gelling agent by forming a fibrillar network through hydrophobic interactions, which is more advantageous than adsorption.

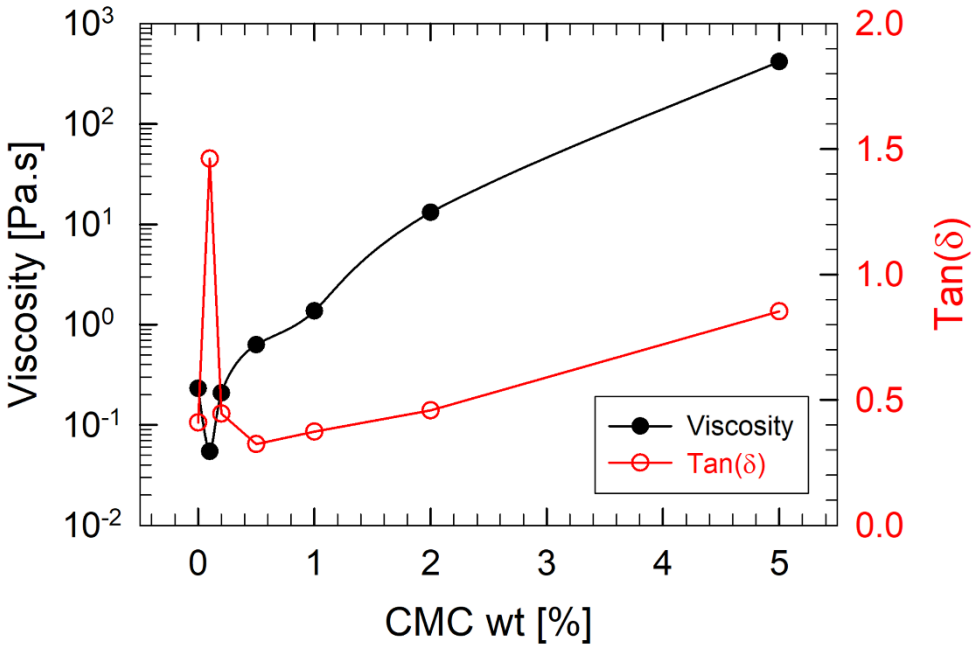

Figure 4.16. Viscosity (shear rate = 0.1 s^{-1}, closed symbol, left) and tan(δ) = G''/G' (frequency = 1 rad/s, red symbol, right) of Si/CB suspension containing Si 15 vol% and CB 0.23 vol% with increasing CMC content.

Figure 4.16 shows the change in viscosity and tan(δ) of the Si(15 vol%)/CB(0.23 vol%)/CMC anode slurries with increasing CMC content. Note that the CB content (0.23 vol%) is different from Figure 4.12 (2.3 vol%). As in Figure 4.12, the viscosity of the slurry decreases and then increases with increasing CMC content. In particular, the viscosity is minimized at CMC 0.1 wt%, which is the content close to the optimum graft density for CB particles,

suggesting the optimum dispersion of the particles. Furthermore, the slurry shows a liquid-like behavior ($\tan(\delta)>1$) only at CMC 0.1 wt%. These imply that CMC selectively adsorbs to CB and acts as a dispersant in the slurry. As the CMC content further increases, the viscosity increases and slurry shows a solid-like behavior ($\tan(\delta)<1$). Since the Si content is sufficient for CMC to act as a flocculant, it agglomerates the particles in the slurry. To summarize, CMC selectively adsorbs to CB particles and acts as a dispersant at a content lower than the optimum graft density for CB particles. When the CMC content increases above the optimum graft density for CB particles, it acts as a flocculant for the particles, as the CMC remaining after adsorption onto the CB particles adsorbs onto the Si particles. As CMC content further increases and the free CMC forms a fibrillar network in the matrix, it acts as a gelling agent for the particles.

4.4. Conclusion

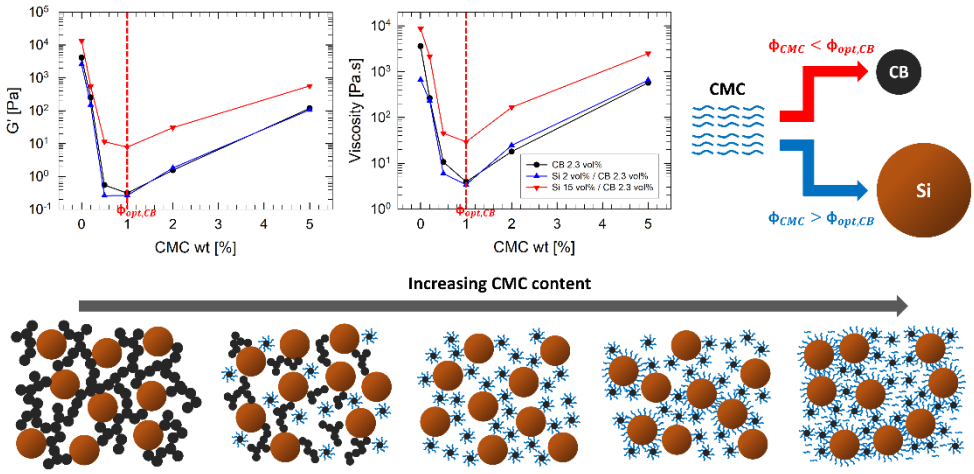

Figure 4.17. Schematic of the rheological behavior and microstructure formation of the Si/CB/CMC anode slurries.

In this chapter, we systematically investigated the rheological behavior and microstructure formation of the Si/CB/CMC anode slurries in terms of inter-particle and polymer-particle interactions, aiming to provide an in-depth understanding of the slurry dispersion. Figure 4.17 summarizes the rheological behavior and microstructure formation of the slurry with respect to interactions between the individual components.

CB particles form a strong network structure through hydrophobic interactions to show a gel-like behavior in the CB suspension. On the other hand, Si particles do not interact to form a network structure, resulting in a Newtonian behavior in the Si suspension. CMC adsorbs onto both particles but has different effect on the interaction between individual particles. The CMC adsorbs on CB particles and acts as a dispersant through electro-

steric interactions. Therefore, the rheological properties of the CB suspension change from gel-like to liquid-like behavior as the CB network structure is stabilized with increasing CMC content. On the other hand, CMC adsorbs on Si particles and acts as a flocculant through bridging interactions. Although the adsorbed CMC forms a network structure of Si particles, the Si suspension does not show plateau modulus, suggesting that the network structure is not as strong as that of the CB particle. As CMC further increases to form a fibrillar network in the matrix, CMC acts as a gelling agent and both suspensions show a weak-gel behavior.

The rheological properties and microstructure formation of Si/CB suspensions are mainly dominated by the CB particles. At CB content insufficient to form a 3D-percolation network ($n \sim 2.1$), Si particles disrupt the CB network structure, leading to a significant decrease in G' and viscosity of the suspension. However, when the CB content is sufficient to form a 3D-percolation network structure ($n \sim 4.2$), Si particles participate and reinforce the CB network structure, increasing the G' and viscosity of the suspension. Further, the gelation of Si/CB suspension is determined by the CB content regardless of the Si content.

In the Si/CB/CMC anode slurry, CMC selectively adsorbs to CB particles. Therefore, at a CMC content lower than the optimum graft density for the CB particles, CMC adsorbs onto the CB particles and acts as a dispersant, decreasing the G' and viscosity of the slurry. However, at higher CMC content, the CMC remaining after adsorption onto the CB particles adsorbs onto the Si particles and acts as a flocculant, increasing the G' and viscosity of the slurry. As the CMC content further increases and free CMC forms a fibrillar network, it

acts as a gelling agent, leading to further increases in the G' and viscosity of the slurry.

Despite the great advantages of silicon, such as high theoretical capacity, eco-friendliness, and abundance in nature, there are many difficulties in fully utilizing Si anode slurries. To fully utilize Si anodes, it is crucial to understand and control the slurry dispersion which directly affects the various electrode properties. We anticipate our findings provide a comprehensive understanding of controlling Si anode slurry dispersion and contribute to the development of Si anode technology.

Chapter 5. Concluding remarks

Dispersibility of the Li-ion battery electrode slurry is emerging as an important issue in both academia and industry as it critically affects the electrochemical performance of the battery as well as the productivity of the electrode process. Numerous studies have been performed to understand the general dispersion behavior of the slurry. However, for electrode process optimization, we must understand the processing effects on the slurry dispersion, as the slurry dispersion can change in various ways depending on the process conditions. In this thesis, changes in dispersion state of the electrode slurry during electrode processes, particularly focusing on the slurry preparation and storage stages, are extensively studied through rheological analysis and microstructure observation in terms of the interactions between individual components.

In chapter 2, focusing on the slurry preparation step, we show how mixing sequence of CMC and particles affects the graphite/CB slurry dispersion based on the understanding of various roles of CMC binder. We find that CMC acts as a dispersant at lower content than the optimum graft density where adsorption of CMC on the particles (graphite/CB) is saturated. When the CMC content further increases, CMC acts as a thickener and gelling agent depending on the content. In the meanwhile, adsorption and dispersion mechanisms of CMC are similar for both particles. Therefore, below the CMC content of optimum graft density, CMC mixing sequence significantly affects the adsorption selectivity of CMC on the particles,

resulting in a large difference in slurry dispersion. However, at higher content, CMC mixing sequence rarely affects the slurry dispersion as both particles are eventually adsorbed and saturated by CMC in the final mixing stage. The findings in chapter 2 show a simple method to control slurry dispersion by changing the mixing sequence of the components, without altering the physiochemical properties of each component and the composition of the slurry. The findings in chapter 2 suggest that the design of the slurry preparation process and consequent evaluation of the slurry dispersion should be accompanied by an in-depth understanding of the interaction between each component at each preparation step.

In chapter 3, focusing on the storage step after slurry preparation, we demonstrate how the dispersion state of NMC/AB cathode slurry changes during storage, which parameter governs the change in slurry microstructure, along with the underlying mechanism. We find that hydrodynamic stress induced by the flow governs the changes in slurry dispersion by simultaneously controlling the agitation speed and matrix viscosity of the slurry. The cathode slurry exhibits different dispersion state before and after the storage condition of the critical hydrodynamic stress. In particular, under the storage conditions lower than the critical hydrodynamic stress, AB particles are significantly aggregated to form a large spherical agglomerate, which is a very dangerous factor in electrode processing. The mechanism of the structural change is understood by considering the Peclet number, which is the relative magnitude of the force between convective transport by flow and thermal motion of particles, and the surface affinity between individual particles. The findings in chapter 3 suggest that storage conditions of the slurry

should be designed in consideration of the flow characteristics and surface affinity between each particle.

In chapter 4, we provide for the first time an in-depth understanding of the rheological behavior and microstructure formation of the anode slurry containing silicon particle, which is attracting as a next-generation anode material. CMC adsorbs to both Si and CB particles but has different effect on the interaction between individual particles. We find that CMC acts as a dispersant for CB particles that tend to form a strong network structure through hydrophobic interaction, while it acts as a flocculant for Si particles that do not form a network structure. In the meanwhile, CMC selectively adsorbs to CB particles. Therefore, at a CMC content lower than the optimum graft density for the CB particles, CMC adsorbs on CB particles and acts as a dispersant through the electro-steric interactions. At higher content, CMC remaining after adsorption on CB particles adsorbs on Si particles and acts as a flocculant through the bridging interactions. As CMC content further increases to form a fibrillar network, CMC acts as a gelling agent in the slurry. The rationale for selective adsorption is explained by different adsorption mechanisms and surface energy analysis of the particles.

Although an extensive study on the processing effect on slurry dispersion is conducted in this thesis, there remain several challenges for further development. First, establishing correlations between slurry dispersion and various electrode properties, such as adhesion (cohesion) strength, microstructure, and electrochemical performance, will broaden our understanding of the electrode process. Second, integrating rheological behavior of the slurry with a variety

of physicochemical or electrochemical analyzes, such as electrochemical impedance spectroscopy (EIS), will deepen our understanding of slurry dispersion. Lastly, cooperative studies combining control of material properties, such as chemical synthesis, with an understanding of slurry processing, will help optimize the electrode process. Nevertheless, we anticipate that our findings and methodology for understanding the processing effect on slurry dispersion will contribute to the optimization of electrode process and the development of LIBs technology.

Bibliography

[1] A. El Kharbachi, O. Zavorotynska, M. Latroche, F. Cuevas, V. Yartys, M. Fichtner, Exploits, advances and challenges benefiting beyond Li-ion battery technologies, Journal of Alloys and Compounds 817 (2020) 153261.

[2] Y. Zhao, O. Pohl, A.I. Bhatt, G.E. Collis, P.J. Mahon, T. Rüther, A.F. Hollenkamp, A review on battery market trends, second-life reuse, and recycling, Sustainable Chemistry 2(1) (2021) 167-205.

[3] N. Wassiliadis, J. Schneider, A. Frank, L. Wildfeuer, X. Lin, A. Jossen, M. Lienkamp, Review of fast charging strategies for lithium-ion battery systems and their applicability for battery electric vehicles, Journal of Energy Storage 44 (2021) 103306.

[4] F. Wang, C. Intrator, N. Salopek, C. Yuan, An Environmental Sustainability Analysis Tool for Next Generation Lithium Ion Batteries of Electric Vehicles, Procedia CIRP 105 (2022) 489-494.

[5] J. Dunn, M. Slattery, A. Kendall, H. Ambrose, S. Shen, Circularity of lithium-ion battery materials in electric vehicles, Environmental Science & Technology 55(8) (2021) 5189-5198.

[6] K. Ariyoshi, H. Yamamoto, Y. Yamada, High dimensional stability of LiCoMnO4 as positive electrodes operating at high voltage for lithium-ion batteries with a long cycle life, Electrochimica Acta 260 (2018) 498-503.

[7] Z. Guan, Z. Zhang, B. Du, Z. Peng, A Non-Flammable Zwitterionic Ionic Liquid/Ethylene Carbonate Mixed Electrolyte for Lithium-Ion Battery with Enhanced Safety, Materials 14(15) (2021) 4225.

[8] A. Nulu, V. Nulu, K.Y. Sohn, Silicon and porous MWCNT composite as high capacity anode for lithium-ion batteries, Korean Journal of Chemical Engineering 37 (2020) 1795-1802.

[9] J.H. Sung, T.W. Kim, H.-K. Kang, S.Y. Choi, F. Hasan, S.K. Mohanty, J. Kim, M.K. Srinivasa, H.-C. Shin, H.D. Yoo, Superior high voltage LiNi0. 6Co0. 2Mn0. 2O2 cathode using Li3PO4 coating for lithium-ion batteries, Korean Journal of Chemical Engineering 38(5) (2021) 1059-1065.

[10] V. Wenzel, H. Nirschl, D. Nötzel, Challenges in lithium-ion-battery slurry preparation and potential of modifying electrode structures by different mixing processes, Energy Technology 3(7) (2015) 692-698.

[11] A. van Bommel, R. Divigalpitiya, Effect of calendering LiFePO4 electrodes, Journal of The Electrochemical Society 159(11) (2012) A1791.

[12] Y. Liu, R. Zhang, J. Wang, Y. Wang, Current and future lithium-ion battery manufacturing, IScience 24(4) (2021) 102332.

[13] J.-S. Seo, B.-K. Na, Effects of Pluronic P123 addition and Cr3+ doping on electrochemical properties of Li4Ti5O12 anode for lithium ion batteries, Korean Journal of Chemical Engineering 38(9) (2021) 1826-1833.

[14] A. Kukay, R. Sahore, A. Parejiya, W.B. Hawley, J. Li, D.L. Wood III, Aqueous Ni-rich-cathode dispersions processed with phosphoric acid for lithium-ion batteries with ultra-thick electrodes, Journal of colloid and interface science 581 (2021) 635-643.

[15] H. Dreger, H. Bockholt, W. Haselrieder, A. Kwade, Discontinuous and continuous processing of low-solvent battery slurries for lithium nickel cobalt manganese oxide electrodes, Journal of Electronic Materials 44 (2015) 4434-4443.

[16] W. YongJian, T. RenHeng, L. WenChao, W. Ying, H. Ling, O. LiuZhang, A high-quality aqueous graphene conductive slurry applied in anode of lithium-ion batteries, Journal of Alloys and Compounds 830 (2020) 154575.

[17] W. Porcher, B. Lestriez, S. Jouanneau, D. Guyomard, Optimizing the surfactant for the aqueous processing of LiFePO4 composite electrodes, Journal of Power Sources 195(9) (2010) 2835-2843.

[18] J.K. Mayer, L. Almar, E. Asylbekov, W. Haselrieder, A. Kwade, A. Weber, H. Nirschl, Influence of the carbon black dispersing process on the microstructure and performance of Li-ion battery cathodes, Energy Technology 8(2) (2020) 1900161.

[19] Y. Kim, S. Kim, B.S. Kim, J.H. Park, K.H. Ahn, J.D. Park, Yielding behavior of concentrated lithium-ion battery anode slurry, Physics of Fluids 34(12) (2022) 123112.

[20] S.H. Sung, S. Kim, J.H. Park, J.D. Park, K.H. Ahn, Role of PVDF in rheology and microstructure of NCM cathode slurries for lithium-ion battery, Materials 13(20) (2020) 4544.

[21] S.L. Morelly, M.H. Tang, N.J. Alvarez, The Impotence of Non-Brownian Particles on the Gel Transition of Colloidal Suspensions, Polymers 9(9) (2017) 461.

[22] G.-W. Lee, J.H. Ryu, W. Han, K.H. Ahn, S.M. Oh, Effect of slurry preparation process on electrochemical performances of LiCoO2 composite electrode, Journal of Power Sources 195(18) (2010) 6049-6054.

[23] S. Lim, S. Kim, K.H. Ahn, S.J. Lee, The effect of binders on the rheological properties and the microstructure formation of lithium-ion battery

anode slurries, Journal of Power Sources 299 (2015) 221-230.

[24] S.H. Sung, D.H. Kim, S. Kim, M.H. Jeong, J. Nam, K.H. Ahn, Effect of neutralization of poly (acrylic acid) binder on the dispersion heterogeneity of Li-ion battery electrodes, Journal of Materials Science 54(20) (2019) 13208-13220.

[25] R. Gordon, R. Orias, N. Willenbacher, Effect of carboxymethyl cellulose on the flow behavior of lithium-ion battery anode slurries and the electrical as well as mechanical properties of corresponding dry layers, Journal of Materials Science 55 (2020) 15867-15881.

[26] T. Mori, K. Kitamura, Effect of adsorption behaviour of polyelectrolytes on fluidity and packing ability of aqueous graphite slurries, Advanced Powder Technology 28(1) (2017) 280-287.

[27] J.H. Park, S.H. Kim, K.H. Ahn, Role of carboxymethyl cellulose binder and its effect on the preparation process of anode slurries for Li-ion batteries, Colloids and Surfaces A: Physicochemical and Engineering Aspects 664 (2023) 131130.

[28] R. Gordon, M. Kassar, N. Willenbacher, Effect of polymeric binders on dispersion of active particles in aqueous LiFePO4-based cathode slurries as well as on mechanical and electrical properties of corresponding dry layers, ACS omega 5(20) (2020) 11455-11465.

[29] K. Kuratani, K. Ishibashi, Y. Komoda, R. Hidema, H. Suzuki, H. Kobayashi, Controlling of dispersion state of particles in slurry and electrochemical properties of electrodes, Journal of The Electrochemical Society 166(4) (2019) A501.

[30] M.K. Dufficy, R.D. Corder, K.A. Dennis, P.S. Fedkiw, S.A. Khan, Guar gel binders for silicon nanoparticle anodes: Relating binder rheology to electrode performance, ACS Applied Materials & Interfaces 13(43) (2021) 51403-51413.

[31] M.H. Kim, S.H. Kwon, H.J. Choi, Effects of dispersion state on rheological and electrical characteristics of concentrated multiwalled carbon nanotube suspensions, Korea-Australia Rheology Journal 31 (2019) 179-186.

[32] K. Kitamura, M. Tanaka, T. Mori, Effects of the mixing sequence on the graphite dispersion and resistance of lithium-ion battery anodes, Journal of Colloid and Interface Science 625 (2022) 136-144.

[33] J. Lee, S. Sung, Y. Kim, J.D. Park, K.H. Ahn, A new paradigm of materials processing—heterogeneity control, Current opinion in chemical engineering 16 (2017) 16-22.

[34] J. Park, K.H. Ahn, Controlling drying stress and mechanical properties of battery electrodes using a capillary force-induced suspension system, Industrial & Engineering Chemistry Research 60(13) (2021) 4873-4882.

[35] F. Duffner, M. Wentker, M. Greenwood, J. Leker, Battery cost modeling: A review and directions for future research, Renewable and Sustainable Energy Reviews 127 (2020) 109872.

[36] M. Wentker, M. Greenwood, J. Leker, A bottom-up approach to lithium-ion battery cost modeling with a focus on cathode active materials, Energies 12(3) (2019) 504.

[37] J.-H. Lee, U. Paik, V.A. Hackley, Y.-M. Choi, Effect of carboxymethyl cellulose on aqueous processing of natural graphite negative electrodes and their electrochemical performance for lithium batteries, Journal of The Electrochemical Society 152(9) (2005) A1763.

[38] M. Ishii, H. Nakamura, Influence of molecular weight and concentration of carboxymethyl cellulose on rheological properties of concentrated anode slurries for lithium-ion batteries, JCIS Open 6 (2022) 100048.

[39] N.-S. Choi, S.-Y. Ha, Y. Lee, J.Y. Jang, M.-H. Jeong, W.C. Shin, M. Ue, Recent progress on polymeric binders for silicon anodes in lithium-ion batteries, Journal of Electrochemical Science and Technology 6(2) (2015) 35-49.

[40] C.-C. Li, Y.-W. Wang, Importance of binder compositions to the dispersion and electrochemical properties of water-based LiCoO2 cathodes, Journal of power sources 227 (2013) 204-210.

[41] C. Li, T. Shi, H. Yoshitake, H. Wang, Improved performance in micron-sized silicon anodes by in situ polymerization of acrylic acid-based slurry, Journal of Materials Chemistry A 4(43) (2016) 16982-16991.

[42] C.-C. Li, Y.-S. Lin, Interactions between organic additives and active powders in water-based lithium iron phosphate electrode slurries, Journal of power sources 220 (2012) 413-421.

[43] D. Grießl, A. Adam, K. Huber, A. Kwade, Effect of the slurry mixing process on the structural properties of the anode and the resulting fast-charging performance of the lithium-ion battery cell, Journal of The Electrochemical Society 169(2) (2022) 020531.

[44] M. Wang, D. Dang, A. Meyer, R. Arsenault, Y.-T. Cheng, Effects of the mixing sequence on making lithium ion battery electrodes, Journal of The Electrochemical Society 167(10) (2020) 100518.

[45] S.L. Morelly, N.J. Alvarez, M.H. Tang, Short-range contacts govern the

performance of industry-relevant battery cathodes, Journal of Power Sources 387 (2018) 49-56.

[46] W. Bauer, D. Nötzel, V. Wenzel, H. Nirschl, Influence of dry mixing and distribution of conductive additives in cathodes for lithium ion batteries, Journal of Power Sources 288 (2015) 359-367.

[47] H. Bockholt, M. Indrikova, A. Netz, F. Golks, A. Kwade, The interaction of consecutive process steps in the manufacturing of lithium-ion battery electrodes with regard to structural and electrochemical properties, Journal of Power Sources 325 (2016) 140-151.

[48] M.J. Snowden, S.M. Clegg, P.A. Williams, I.D. Robb, Flocculation of silica particles by adsorbing and non-adsorbing polymers, Journal of the Chemical Society, Faraday Transactions 87(14) (1991) 2201-2207.

[49] A.A. Zaman, N. Delorme, Effect of polymer bridging on rheological properties of dispersions of charged silica particles in the presence of low-molecular-weight physically adsorbed poly (ethylene oxide), Rheologica acta 41 (2002) 408-417.

[50] J.B. Hooper, K.S. Schweizer, Contact aggregation, bridging, and steric stabilization in dense polymer– particle mixtures, Macromolecules 38(21) (2005) 8858-8869.

[51] S. Kim, K. Hyun, B. Struth, K.H. Ahn, C. Clasen, Structural development of nanoparticle dispersion during drying in polymer nanocomposite films, Macromolecules 49(23) (2016) 9068-9079.

[52] S. Yasin, P. Luckham, Investigating the effectiveness of PEO/PPO based copolymers as dispersing agents for graphitic carbon black aqueous dispersions, Colloids and Surfaces A: Physicochemical and Engineering Aspects 404 (2012) 25-35.

[53] V. Moraru, N. Lebovka, D. Shevchenko, Structural transitions in aqueous suspensions of natural graphite, Colloids and Surfaces A: Physicochemical and Engineering Aspects 242(1-3) (2004) 181-187.

[54] S. Kim, K. Hyun, J.Y. Moon, C. Clasen, K.H. Ahn, Depletion stabilization in nanoparticle-polymer suspensions: multi-length-scale analysis of microstructure, Langmuir 31(6) (2015) 1892-1900.

[55] R. Hasegawa, Y. Aoki, M. Doi, Optimum graft density for dispersing particles in polymer melts, Macromolecules 29(20) (1996) 6656-6662.

[56] T.-w. Kwon, J.W. Choi, A. Coskun, The emerging era of supramolecular polymeric binders in silicon anodes, Chemical Society Reviews 47(6) (2018) 2145-2164.

[57] S. Kim, S.H. Sung, S. Lim, K.H. Ahn, Particle dispersion in silica-poly (vinyl alcohol) coatings: Role of particle-polymer interaction, BioResources 13(2) (2018) 3195-3207.

[58] K. White, S. Hawkins, M. Miyamoto, A. Takahara, H.-J. Sue, Effects of aspect ratio and concentration on rheology of epoxy suspensions containing model plate-like nanoparticles, Physics of Fluids 27(12) (2015) 123306.

[59] C.G. Lopez, R.H. Colby, J.o.T. Cabral, Electrostatic and hydrophobic interactions in NaCMC aqueous solutions: Effect of degree of substitution, Macromolecules 51(8) (2018) 3165-3175.

[60] A. Benchabane, K. Bekkour, Rheological properties of carboxymethyl cellulose (CMC) solutions, Colloid and Polymer Science 286(10) (2008) 1173-1180.

[61] T. Müller, H. Hakert, T. Eckert, Rheological and electron microscopic characterization of aqueous carboxymethyl cellulose gels Part II: Visualization of the gel structure by freeze-fracturing, Colloid and Polymer Science 267 (1989) 230-236.

[62] Y. Liu, C. Dai, K. Wang, C. Zou, M. Gao, Y. Fang, M. Zhao, Y. Wu, Q. You, Study on a novel cross-linked polymer gel strengthened with silica nanoparticles, Energy & Fuels 31(9) (2017) 9152-9161.

[63] B. Ludwig, Z. Zheng, W. Shou, Y. Wang, H. Pan, Solvent-free manufacturing of electrodes for lithium-ion batteries, Scientific reports 6(1) (2016) 1-10.

[64] J. Lee, B. Lee, A simple method to determine the surface energy of graphite, Carbon letters 21 (2017) 107-110.

[65] M.K. Burdette-Trofimov, B.L. Armstrong, L. Heroux, M. Doucet, A.E.M. Rossy, D.T. Hoelzer, N. Kanbargi, A.K. Naskar, G.M. Veith, Competitive adsorption within electrode slurries and impact on cell fabrication and performance, Journal of Power Sources 520 (2022) 230914.

[66] P.C. Hidber, T.J. Graule, L.J. Gauckler, Competitive adsorption of citric acid and poly (vinyl alcohol) onto alumina and its influence on the binder migration during drying, Journal of the American Ceramic Society 78(7) (1995) 1775-1780.

[67] R.M. Fernandes, M. Buzaglo, O. Regev, E.F. Marques, I. Furo, Surface coverage and competitive adsorption on carbon nanotubes, The Journal of Physical Chemistry C 119(38) (2015) 22190-22197.

[68] Y. Yang, S. Wu, Y. Zhang, C. Liu, X. Wei, D. Luo, Z. Lin, Towards efficient binders for silicon based lithium-ion battery anodes, Chemical Engineering

Journal 406 (2021) 126807.

[69] Y. Kang, C. Deng, Y. Chen, X. Liu, Z. Liang, T. Li, Q. Hu, Y. Zhao, Binder-free electrodes and their application for Li-ion batteries, Nanoscale Research Letters 15(1) (2020) 1-19.

[70] S. Huang, J. Ren, R. Liu, M. Yue, Y. Huang, G. Yuan, Enhanced electrochemical properties of a natural graphite anode using a promising crosslinked ionomer binder in Li-ion batteries, New Journal of Chemistry 41(20) (2017) 11759-11765.

[71] W. Wang, T. Yang, S. Li, W. Fan, X. Zhao, C. Fan, L. Yu, S. Zhou, X. Zuo, R. Zeng, 1-ethyl-3-methylimidazolium tetrafluoroborate (EMI-BF4) as an ionic liquid-type electrolyte additive to enhance the low-temperature performance of LiNi0. 5Co0. 2Mn0. 3O2/graphite batteries, Electrochimica Acta 317 (2019) 146-154.

[72] C. Yuan, H. Cao, K. Shen, Y. Deng, D. Zeng, Y. Dong, M. Hauschild, Water-based manufacturing of lithium ion battery for life cycle impact mitigation, CIRP Annals 70(1) (2021) 25-28.

[73] G.A. Collins, K. McNamara, S. Kilian, H. Geaney, K.M. Ryan, Alloying germanium nanowire anodes dramatically outperform graphite anodes in full-cell chemistries over a wide temperature range, ACS Applied Energy Materials 4(2) (2021) 1793-1804.

[74] Y. Ren, J. Li, J. Guo, Perforated Active Carbon and Pre-Lithiated Graphite Electrodes for High Performance Hybrid Lithium-ion Capacitors, Int. J. Electrochem. Sci 15 (2020) 2659-2666.

[75] D. Guy, B. Lestriez, R. Bouchet, D. Guyomard, Critical role of polymeric binders on the electronic transport properties of composites electrode, Journal of The Electrochemical Society 153(4) (2006) A679.

[76] Y.I. Kwon, J.D. Kim, Y.S. Song, Agitation effect on the rheological behavior of lithium-ion battery slurries, Journal of Electronic Materials 44 (2015) 475-481.

[77] Z. Wang, T. Zhao, M. Takei, Morphological structure characterizations in lithium-ion battery (LIB) slurry under shear rotational conditions by on-line dynamic electrochemical impedance spectroscopy (EIS) method, Journal of The Electrochemical Society 164(9) (2017) A2268.

[78] Z. Wang, T. Zhao, M. Takei, Clarification of particle dispersion behaviors based on the dielectric characteristics of cathode slurry in lithium-ion battery (LIB), Journal of The Electrochemical Society 166(2) (2019) A35.

[79] K. Meienberg, T. Malinina, Z. Nguyen, C. Park, M. Glaser, N. Clark, J.

Maclennan, Nanoparticle aggregation and fractal growth in fluid smectic membranes, Molecular Crystals and Liquid Crystals 611(1) (2015) 14-20.

[80] R. Dominko, M. Gaberšček, J. Drofenik, M. Bele, J. Jamnik, Influence of carbon black distribution on performance of oxide cathodes for Li ion batteries, Electrochimica Acta 48(24) (2003) 3709-3716.

[81] R. Dominko, M. Gaberscek, J. Drofenik, M. Bele, S. Pejovnik, J. Jamnik, The role of carbon black distribution in cathodes for Li ion batteries, Journal of Power Sources 119 (2003) 770-773.

[82] J.K. Hong, J.H. Lee, S.M. Oh, Effect of carbon additive on electrochemical performance of LiCoO2 composite cathodes, Journal of power sources 111(1) (2002) 90-96.

[83] A.S. Negi, C.O. Osuji, New insights on fumed colloidal rheology—shear thickening and vorticity-aligned structures in flocculating dispersions, Rheologica acta 48(8) (2009) 871-881.

[84] P.T. Spicer, Shear-induced aggregation-fragmentation: mixing and aggregate morphology effects, University of Cincinnati1997.

[85] C.O. Osuji, D.A. Weitz, Highly anisotropic vorticity aligned structures in a shear thickening attractive colloidal system, Soft Matter 4(7) (2008) 1388-1392.

[86] S.-P. Rwei, I. Manas-Zloczower, D. Feke, Observation of carbon black agglomerate dispersion in simple shear flows, Polymer Engineering & Science 30(12) (1990) 701-706.

[87] F.M. Fowkes, Calculation of work of adhesion by pair potential suummation, Journal of colloid and interface science 28(3-4) (1968) 493-505.

[88] P. Segre, V. Prasad, A.B. Schofield, D. Weitz, Glasslike kinetic arrest at the colloidal-gelation transition, Physical Review Letters 86(26) (2001) 6042.

[89] F. Sciortino, S.V. Buldyrev, C. De Michele, G. Foffi, N. Ghofraniha, E. La Nave, A. Moreno, S. Mossa, I. Saika-Voivod, P. Tartaglia, Routes to colloidal gel formation, Computer physics communications 169(1-3) (2005) 166-171.

[90] L.C. Johnson, B.J. Landrum, R.N. Zia, Yield of reversible colloidal gels during flow start-up: Release from kinetic arrest, Soft Matter 14(24) (2018) 5048-5068.

[91] Z. Daneshfar, F. Goharpey, H. Nazockdast, R. Foudazi, Rheology of concentrated bimodal suspensions of nanosilica in PEG, Journal of Rheology 61(5) (2017) 955-966.

[92] T. Jiang, C.F. Zukoski, Rheology of high density glass of binary colloidal

mixtures in unentangled polymer melts, Soft Matter 9(11) (2013) 3117-3130.

[93] A. Moncho-Jordá, A. Louis, J. Padding, How Péclet number affects microstructure and transient cluster aggregation in sedimenting colloidal suspensions, The Journal of chemical physics 136(6) (2012) 064517.

[94] Y. Komoda, S. Kobayashi, H. Suzuki, R. Hidema, Effect of shear strain in coating on the particle packing of gelled-clay particle dispersions during drying, Journal of Coatings Technology and Research 12 (2015) 939-948.

[95] M. Gu, Y. He, J. Zheng, C. Wang, Nanoscale silicon as anode for Li-ion batteries: The fundamentals, promises, and challenges, Nano Energy 17 (2015) 366-383.

[96] L.-F. Cui, R. Ruffo, C.K. Chan, H. Peng, Y. Cui, Crystalline-amorphous core– shell silicon nanowires for high capacity and high current battery electrodes, Nano letters 9(1) (2009) 491-495.

[97] B. Wang, X. Li, X. Zhang, B. Luo, Y. Zhang, L. Zhi, Contact-engineered and void-involved silicon/carbon nanohybrids as lithium-ion-battery anodes, Advanced materials 25(26) (2013) 3560-3565.

[98] H. Gao, L. Xiao, I. Plu¨mel, G.-L. Xu, Y. Ren, X. Zuo, Y. Liu, C. Schulz, H. Wiggers, K. Amine, Parasitic reactions in nanosized silicon anodes for lithium-ion batteries, Nano Letters 17(3) (2017) 1512-1519.

[99] J.H. Ryu, J.W. Kim, Y.-E. Sung, S.M. Oh, Failure modes of silicon powder negative electrode in lithium secondary batteries, Electrochemical and solid-state letters 7(10) (2004) A306.

[100] M.T. McDowell, S. Xia, T. Zhu, The mechanics of large-volume-change transformations in high-capacity battery materials, Extreme Mechanics Letters 9 (2016) 480-494.

[101] Y. Yao, M.T. McDowell, I. Ryu, H. Wu, N. Liu, L. Hu, W.D. Nix, Y. Cui, Interconnected silicon hollow nanospheres for lithium-ion battery anodes with long cycle life, Nano letters 11(7) (2011) 2949-2954.

[102] H. Wu, Y. Cui, Designing nanostructured Si anodes for high energy lithium ion batteries, Nano today 7(5) (2012) 414-429.

[103] R. Kumar, A. Tokranov, B.W. Sheldon, X. Xiao, Z. Huang, C. Li, T. Mueller, In situ and operando investigations of failure mechanisms of the solid electrolyte interphase on silicon electrodes, ACS Energy Letters 1(4) (2016) 689-697.

[104] M. Ling, Y. Xu, H. Zhao, X. Gu, J. Qiu, S. Li, M. Wu, X. Song, C. Yan, G. Liu, Dual-functional gum arabic binder for silicon anodes in lithium ion

batteries, Nano Energy 12 (2015) 178-185.

[105] K. Kim, I. Park, S.-Y. Ha, Y. Kim, M.-H. Woo, M.-H. Jeong, W.C. Shin, M. Ue, S.Y. Hong, N.-S. Choi, Understanding the thermal instability of fluoroethylene carbonate in LiPF6-based electrolytes for lithium ion batteries, Electrochimica Acta 225 (2017) 358-368.

[106] D. Wang, C. Zhou, B. Cao, Y. Xu, D. Zhang, A. Li, J. Zhou, Z. Ma, X. Chen, H. Song, One-step synthesis of spherical Si/C composites with onion-like buffer structure as high-performance anodes for lithium-ion batteries, Energy Storage Materials 24 (2020) 312-318.

[107] L. Hozer, J.-R. Lee, Y.-M. Chiang, Reaction-infiltrated, net-shape SiC composites, Materials Science and Engineering: A 195 (1995) 131-143.

[108] N. Ding, J. Xu, Y. Yao, G. Wegner, I. Lieberwirth, C. Chen, Improvement of cyclability of Si as anode for Li-ion batteries, Journal of Power Sources 192(2) (2009) 644-651.

[109] G.G. Eshetu, E. Figgemeier, Confronting the challenges of next-generation silicon anode-based lithium-ion batteries: role of designer electrolyte additives and polymeric binders, ChemSusChem 12(12) (2019) 2515-2539.

[110] C.-C. Wu, C.-C. Li, Distribution uniformity of water-based binders in si anodes and the distribution effects on cell performance, ACS Sustainable Chemistry & Engineering 8(17) (2020) 6868-6876.

[111] G. Sandu, B. Ernould, J. Rolland, N. Cheminet, J. Brassinne, P.R. Das, Y. Filinchuk, L. Cheng, L. Komsiyska, P. Dubois, Mechanochemical synthesis of PEDOT: PSS hydrogels for aqueous formulation of Li-ion battery electrodes, ACS applied materials & interfaces 9(40) (2017) 34865-34874.

[112] J. Park, N. Willenbacher, K.H. Ahn, How the interaction between styrene-butadiene-rubber (SBR) binder and a secondary fluid affects the rheology, microstructure and adhesive properties of capillary-suspension-type graphite slurries used for Li-ion battery anodes, Colloids and Surfaces A: Physicochemical and Engineering Aspects 579 (2019) 123692.

[113] L. Chai, Q. Qu, L. Zhang, M. Shen, L. Zhang, H. Zheng, Chitosan, a new and environmental benign electrode binder for use with graphite anode in lithium-ion batteries, Electrochimica Acta 105 (2013) 378-383.

[114] L.-H. Huang, C.-C. Li, Effects of interactions between binders and different-sized silicons on dispersion homogeneity of anodes and electrochemistry of lithium-silicon batteries, Journal of Power Sources 409 (2019) 38-47.

[115] Y. Lai, H. Li, Y. Zhang, Q. Yang, H. Li, Y. Sun, Y. Liu, B. Zhong, Z. Wu, X. Guo, Investigation of effective bonding between varied binders and Si anode with different particle sizes, Applied Physics Letters 121(18) (2022) 183901.

[116] L.-H. Huang, D. Chen, C.-C. Li, Y.-L. Chang, J.-T. Lee, Dispersion homogeneity and electrochemical performance of Si anodes with the addition of various water-based binders, Journal of The Electrochemical Society 165(10) (2018) A2239.

[117] F. Bigoni, F. De Giorgio, F. Soavi, C. Arbizzani, Sodium alginate: a water-processable binder in high-voltage cathode formulations, Journal of The Electrochemical Society 164(1) (2016) A6171.

[118] B. Kim, Y. Song, B. Youn, D. Lee, Dispersion Homogeneity of Silicon Anode Slurries with Various Binders for Li-Ion Battery Anode Coating, Polymers 15(5) (2023) 1152.

[119] M.K. Burdette-Trofimov, B.L. Armstrong, A.M. Rogers, L. Heroux, M. Doucet, G. Yang, N.D. Phillip, M.K. Kidder, G.M. Veith, Understanding Binder-Silicon Interactions during Slurry Processing, The Journal of Physical Chemistry C 124(24) (2020) 13479-13494.

[120] J. Li, R. Lewis, J. Dahn, Sodium carboxymethyl cellulose: a potential binder for Si negative electrodes for Li-ion batteries, Electrochemical and Solid-State Letters 10(2) (2006) A17.

[121] Y.M. Zhao, F.S. Yue, S.C. Li, Y. Zhang, Z.R. Tian, Q. Xu, S. Xin, Y.G. Guo, Advances of polymer binders for silicon-based anodes in high energy density lithium-ion batteries, InfoMat 3(5) (2021) 460-501.

[122] M. Sahimi, S. Arbabi, Mechanics of disordered solids. II. Percolation on elastic networks with bond-bending forces, Physical Review B 47(2) (1993) 703.

[123] M. Youssry, F.Z. Kamand, M.I. Magzoub, M.S. Nasser, Aqueous dispersions of carbon black and its hybrid with carbon nanofibers, RSC advances 8(56) (2018) 32119-32131.

[124] R. Niu, J. Gong, D. Xu, T. Tang, Z.-Y. Sun, Rheological properties of ginger-like amorphous carbon filled silicon oil suspensions, Colloids and Surfaces A: Physicochemical and Engineering Aspects 444 (2014) 120-128.

[125] M. Youssry, D. Guyomard, B. Lestriez, Suspensions of carbon nanofibers in organic medium: Rheo-electrical properties, Physical Chemistry Chemical Physics 17(48) (2015) 32316-32327.

[126] J. Mewis, N.J. Wagner, Colloidal suspension rheology, Cambridge

university press2012.

[127] P. Atkins, J. De Paula, Physical chemistry for the life sciences, Oxford University Press, USA2011.

[128] R. Chang, Physical chemistry for the biosciences, University Science Books2005.

[129] H.A. Scheraga, Theory of hydrophobic interactions, Journal of Biomolecular Structure and Dynamics 16(2) (1998) 447-460.

Abstract (Korean)

리튬이온 배터리 전극 슬러리의 분산 특성은 배터리 성능 및 전극 공정의 생산성과 직결되기에 학계 및 산업계에서 중요한 이슈로 떠오르고 있다. 전극 공정에서 슬러리의 분산 특성을 효과적으로 제어하기 위해서는 재료 및 공정 특성에 대한 포괄적인 이해가 필요하다. 그러나 전극 슬러리 구성 성분들 간의 상호작용에 대한 가공 효과와, 그에 따른 슬러리의 분산 특성 변화에 대한 심도 있는 이해는 여전히 부족하다.

본 논문에서는 전극 공정 중 슬러리 제조 및 보관 단계에서 리튬이온 배터리 전극 슬러리의 유변학적 거동 및 분산 상태의 변화를 공정 조건과 각 성분들 간의 상호작용 관점에서 체계적으로 연구하였다. 첫 번째 장에서는 슬러리 제조 단계에 초점을 맞추어, graphite/CB 음극 슬러리에서 CMC바인더의 다양한 역할과 그로 인해 CMC바인더가 음극 슬러리 제조 공정에 어떠한 영향을 미치는지를 연구하였다. CMC는 함량이 증가함에 따라 분산제, 증점제, 그리고 겔화제 역할을 했다. 특히, 두 입자에 대한 CMC의 유사한 흡착 및 분산 메커니즘으로 인해, 최적 그래프트 밀도(optimum graft density)보다 낮은 CMC함량에서 CMC와 두 입자의 혼합 순서는 슬러리 분산성에 큰 영향을 미치는 것을 확인했다. 다음 장에서는 슬러리 보관 단계에 초점을 두고, 보관 중 NMC/AB 양극 슬러리의 분산 상태 변화와 그 메커니즘을 연구하였다. 보관 중 양극 슬러리의 분산 상태 변화는 유동에 의한 유체역학적 응력(hydrodynamic stress)이 지배했다. 따라서, 임계 유체역학적 응력(critical hydrodynamic stress)의 보관 조건을 전후로 양극 슬러리는 서로 다른 분산 상태를 보이는 것을 확인했다. 마지막 장에서는 차세대 음극 활물질이 포함된 Si/CB/CMC 음극 슬러리의 유변학적 거동 및 미세구조 형성 메커니즘을 연구하였다. CMC는 음극 슬러리의 두 입자 중 CB입자에 선택적으로 흡착했다. 따라서, CMC는 슬러리에서 낮은 함량에서는 CB입자의 분산제 역할을 하는 반면, 높은 함량에서는 입자

들의 응집제 역할을 하는 것을 확인했다.

본 학위논문은 전극 슬러리의 각 구성 성분들 간의 상호작용에 대한 이해를 바탕으로 액상 전극 공정, 특히 슬러리 제조 및 저장 단계에서 슬러리 분산성 변화에 대한 심도있는 이해를 제공하는 것을 목적으로 수행되었다. 연구 결과는 슬러리 가공 가이드라인을 제시하여 전극 공정 최적화 및 생산성 향상에 기여할 것으로 기대된다.

주요어: 리튬이온 배터리, 전극 공정, 슬러리 분산, 바인더, 유변학, 미세구조

학 번: 2018-26542